Arts & Sciences Electronic Theses and Dissertations

Arts & Sciences

Summer 8-15-2015

Neural Basis of Functional Connectivity MRI

Jingfeng Li
Washington University in St. Louis

Follow this and additional works at: https://openscholarship.wustl.edu/art_sci_etds

Part of the Biology Commons

WASHINGTON UNIVERSITY IN ST. LOUIS

Division of Biology and Biomedical Sciences
Neurosciences

Dissertation Examination Committee:
Lawrence Snyder, Chair
Erik Herzog
Camillo Padoa-Schioppa
Steve Petersen
John Pruett

Neural Basis of Functional Connectivity MRI

by

Jingfeng Li

A dissertation presented to the
Graduate School of Arts & Sciences
of Washington University in
partial fulfillment of the
requirements for the degree
of Doctor of Philosophy

August 2015
St. Louis, Missouri

Table of Contents

List of Figures

List of Tables

<u>Acknowledgments</u>

First, I would like to thank Larry. Larry is a great mentor, and he explains things in great detail, which is especially helpful for me, because I had very limited exposure to neuroscience before coming to graduate school. The last five years have been a very enjoyable journey, and Larry is the most significant contributor to it.

Second, I would like to thank my thesis committee. John served as the chair for both my qualifying exam committee and my thesis committee. He is extremely helpful. When I expressed my interest in transitioning to industry, he was supportive and helped me build connections, and I am very grateful for his help. Camillo, Erik, and Steve have provided lots of valuable feedback.

Third, I would like to thank Paul Taghert. He took me as a summer student during my junior year. That experience inspired me to pursue a PhD in neuroscience.

Fourth, I would like to thank the lab. I would like to thank Will Bently for setting up and initiating the project. We have lots of stimulating conversations. I would like to thank Jonathan and Mary Kay for taking care of the monkeys. I would also like to thank my classmates and friends. You guys make good times better, and make bad times not so bad.

Fifth, I would like to thank my mom, my dad, and my brother. They supported me to pursue my dreams. My mom taught me to be kind, my dad taught me to be confident, and my brother built my interest in biology by sharing lots of fascinating stories about zoology.

Last but not the least, I would like to thank my husband, Brian Daniels. He made my PhD journey fun and fabulous. He spent so many hours proofreading my documents and listening to my practice talks. I am so thankful to have Brian in my life.

ABSTRACT OF THE DISSERTATION

Neural Basis of Functional Connectivity MRI

by

Jingfeng Li

Doctor of Philosophy in Biology and Biomedical Sciences

Neurosciences

Washington University in St. Louis, 2015

Professor Lawrence Snyder, Chair

The brain is hierarchically organized across a range of scales. While studies based on electrophysiology and anatomy have been fruitful on the micron to millimeter scale, findings based on functional connectivity MRI (fcMRI) suggest that a higher level of brain organization has been largely overlooked. These findings show that the brain is organized into networks, and each network extends across multiple brain areas. This large-scale, across-area brain organization is functionally relevant and stable across subjects, primate species, and levels of consciousness.

This dissertation addresses the neural origin of MRI functional connectivity. fcMRI relies on temporal correlation in at-rest blood oxygen level dependent (BOLD) fluctuations. Thus, understanding the neural origin of at-rest BOLD correlation is of critical significance. By shedding light on the origin of the large-scale brain organization captured by fcMRI, it will guide the design and interpretation of fcMRI studies. Prior investigations of the neural basis of BOLD have not addressed the at-rest BOLD correlation, and they have been focusing on task-related

BOLD. At-rest BOLD correlation captured by fcMRI likely reflects a distinct physiological

process that is different from that of task-related BOLD, since these two kinds of BOLD

dynamics are different in their temporal scale, spatial spread, energy consumption, and their

dependence on consciousness.

To address this issue, we develop a system to simultaneously record oxygen and

electrophysiology in at-rest, awake monkeys. We demonstrate that our oxygen measurement,

oxygen polarography, captures the same physiological phenomenon as BOLD by showing that

task-related polarographic oxygen responses and at-rest polarographic oxygen correlation are

similar to those of BOLD. These results validate the use of oxygen polarography as a surrogate

for BOLD to address the neural origin of MRI functional connectivity.

Next, we show that at-rest oxygen correlation reflects at-rest correlation in

electrophysiological signals, especially spiking activity of neurons. Using causality analysis, we

show that oxygen is driven by slow changes in raw local field potential levels (slow LFP), and

slow LFP itself is driven by spiking activity. These results provide critical support to the idea

that oxygen correlation reflects neural activity, and pose significant challenges to the traditional

view of neurohemodynamic coupling.

In addition, we find that at-rest correlation does not originate from criticality, which has

been the dominant hypothesis in the field. Instead, we show that at-rest correlation likely reflects

a specific and potentially localized oscillatory process. We suggest that this oscillatory process

could be a result of the delayed negative feedback loop between slow LFP and spiking activity.

Thus, we conclude that at-rest BOLD correlation captured by fcMRI is driven by at-rest

slow LFP correlation, which is itself driven by spiking activity correlation. The at-rest spiking

activity correlation, itself, is likely driven by an oscillatory process. Future studies combining recording with interventional approaches, like pharmacological manipulation and microstimulation, will help to elucidate the circuitry underlying the oscillatory process and its potential functional role.

Chapter 1: Introduction

The brain is hierarchically organized across a range of scales - from cellular neuronal circuits at the scale of columns, layers, and areas, to large-scale, across-area networks. While intracranial electrophysiology recording has been fruitful on the cellular scale, findings from methods looking at across-area relationships, such as functional connectivity MRI (fcMRI), suggest that an entire level of organization in the brain has been largely overlooked. fcMRI findings have revealed that brain is organized into functional networks, which are stable across subjects, levels of consciousness and species (1). An important concern, however, is that fcMRI relies on the temporal correlation in at-rest blood oxygen level dependent signals (spontaneous BOLD), which are at the most an indirect measure of neural activity. This thesis aims to elucidate the neural basis of at-rest BOLD correlation, and our work will further our understanding of the large-scale brain functional organization captured by at-rest BOLD correlation.

In the following sections, we briefly cover topics including BOLD and BOLD correlation, electrophysiology and neural activity, the neural basis of BOLD correlation, and heuristic models of the origin of BOLD correlation.

1.1 BOLD and BOLD correlation

The fundamental signal for blood oxygen-level dependent (BOLD) functional magnetic resonance imaging (fMRI) signal comes from hydrogen atoms (2). In a magnetic field, hydrogen

atoms are at a low-energy, equilibrium state. Hydrogen atoms can leave this state by absorbing energy that is applied by a radio frequency pulse. After the radio frequency pulse, the energized hydrogen atoms emit energy until they return to their equilibrium state, and the emitted energy is measured by a T2* weighted MR imaging. The measured signal decays over time, and the speed of the decay is influenced by various factors, including the presence of inhomogeneities in the magnetic field. Greater inhomogeneity leads to a faster delay and a smaller signal (2).

Oxygenation state of the blood affects its magnetic property, with deoxyhemoglobin (paramagnetic) introducing a small local field inhomogeneity, and oxyhemoglobin (diamagnetic) producing a more uniform microscopic field homogeneity. Changes in the amount of deoxyhemoglobin in the sampled volume is reflected in MRI signal intensity (2). An increase in deoxyhemoglobin leads to a loss of fMRI signal. The amount of deoxyhemoglobin depends in turn on blood oxygen level (3). Thus, fMRI signal is often referred to as blood oxygen level dependent signal, or BOLD.

BOLD variances have two varieties: the fast, transient BOLD response that is related by external stimuli, a task or a cognitive challenge (task-related BOLD), and slow (<0.1Hz) BOLD fluctuation that occurs all the time, even when subjects are at rest with no explicit sensory input or motor output (at-rest BOLD, or spontaneous BOLD) (4). While task-related BOLD is of great significance by providing a non-invasive approach to study whole-brain activity, spontaneous BOLD has become the primary signal used to study brain functional organization.

In 1995, Biswal and colleagues first noted that slow, spontaneous BOLD signals in the left and right motor cortices were well correlated in time, even when the subjects were at rest, that is, they had no task to perform and were not presented with any salient stimuli (5). Over the

next 20 years, the number of studies exploring BOLD correlations has exploded. A whole research field now is dedicated to investigate at-rest BOLD correlations, referred to as resting-state functional connectivity MRI (rs-fcMRI).

Substantial evidence suggests that at-rest BOLD correlation reflects a fundamental aspect of brain organization. BOLD correlations exist among groups of spatially segregated areas. These groups of areas form networks, such as those associated with sensorimotor, language, attention, and executive functions, as well as the "default mode" network. The spatial structure of these networks closely resembles the functional architecture of co-activations related by experimentally administered tasks (6-10). The resemblance between BOLD correlation networks and task-related co-activation patterns indicates that BOLD correlation does not randomly exist across brain areas, but instead exists between functionally related areas, reflecting large-scale functional organization (11). Second, the spatial pattern of correlation networks is largely conserved across tasks, subjects, primate species, and levels of consciousness (4, 12, 13), suggesting that BOLD correlation reflects a brain organizational principle that is critical to normal brain function. Finally, BOLD correlation is linked to behavior, cognition, brain function and brain dysfunction. Differences in spontaneous BOLD fluctuations are correlated with within-subject differences in perception and behavior(14-16), and variations in the strength of BOLD correlations have been correlated with inter-individual differences in task performance, fluid intelligence, perception, and mood (17-21). Characteristic anomalies in BOLD correlation structure and correlation strength have been observed in many neurological disorders, such as autism and schizophrenia (22, 23). Changes in correlation structure are associated with behavioral impairment after brain injury (24, 25). Together, these observations suggest that BOLD correlations reflect a fundamental, functionally relevant aspect of brain organization (26).

1.2. Electrophysiology and neural activity

Electrophysiological recordings in the extracellular space measure electrical activity generated by various neural processes by the local neural population. Action potentials in cell bodies and axons produce characteristic deflections of the extracellular potential, which is referred to as "spikes". Most of the energy in spikes locates between 600 and 4000 Hz (27). Spikes from one single neuron can be isolated and identified as "single unit activity", and spikes originating from a two or more nearby neurons are referred to as "multi-unit spiking activity" (MUA). Though it is difficult to determine which neuron type is being recorded or in which layer the recorded neuron is situated, pyramidal neurons are likely to be the most significant contributor due to their large discharge waveforms (27). There are also lower frequency fluctuations (<200Hz) in the extracellular potential. These low frequency fluctuations are referred to as the local field potentials, or LFPs.

Local field potential:

LFP differs from electroencephalogram (EEG) and electrocorticogram (EcoG), because LFP is recorded in depth, from within the cortical tissue, using microelectrodes. LFP has been linked to a variety of cognitive processes, such as attention, perception, and memory (27). However, the exact origin of LFP is unclear. The working hypothesis is that LFP comes from local synaptic activity. Synaptic activity leads to current flow within dendrites. The current flow in a single dendrite creates a dipole: a current sink at the dendrite and a source at the soma (assuming excitatory inputs) (28). LFP is a weighted average of these dipoles from the local population. The dendritic arbors of most neurons are relatively uniform, and to the extent that they are not, the arbors of nearby neurons are randomly directed, such that the dipoles created by

these arbors cancel each other out. A prominent exception is found in pyramidal neurons. Pyramidal neurons have large dendritic arbors, and the dendrite-to-soma dipoles are neatly aligned across pyramidal neurons (29). Thus, pyramidal neurons are thought to be the most significant contributor to LFP (27).

In addition to excitatory postsynaptic potentials, other sources are also likely to contribute to LFP, such as inhibitory synaptic input, integrative soma-dendritic processes including subthreshold membrane oscillations, and afterpotentials of somatodendritic action potentials (30-32). Further, low frequency components of spike waveforms might also contribute to LFP (33), though these contributions are likely to be negligible, because the signature spike waveform in the extracellular electrical field is believed to be above 300 Hz.

Two aspects of LFP are often looked at in their relationship to BOLD**:** the power of high frequency (1~150 Hz) LFP bands (LFP power), and slow fluctuation (< 1Hz) of raw LFP levels (slow LFP).

1.2.1. LFP band and LFP power:

A LFP band is a signal extracted by filtering the LFP signal into different frequency ranges, and the power of a LFP band (LFP power) is typically computed as a signal of interest. This approach of looking at LFP signals is inspired from the EEG literature, where EEG signals can be separated into well-defined rhythms with distinct dynamics, and different rhythms correspond to distinct behavioral states (27). However, well-separated rhythms are typically not observed in LFP signals. Nevertheless, LFP signals are often separated into 5 LFP bands, corresponding to standard EEG bands: delta band (1-4 Hz), theta band (4-8 Hz), alpha band (8-16 Hz), beta band (16-32 Hz), and gamma band (32-128 Hz). (We report specific boundaries for each band, but in fact the exact boundaries vary across studies.)

A related concept to LFP band is LFP oscillation. A LFP oscillation refers to the repeating LFP patterns following a particular temporal beat or period. A simple example for an oscillation is a pure sine wave. In reality, for a given LFP oscillation, the repeating pattern does not have to be the shape as a sine function. To test the existence of LFP oscillations, appropriate statistics should be applied to demonstrate periodicity (34-36). In general, a LFP oscillation can be identified in the frequency domain, where the oscillation stands out as a peak in the power spectrum. In contrast, a LFP band is a signal being extracted from the raw LFP signal by band-pass filtering. Not all LFP signals contain LFP oscillations. However, any LFP signal, whether or not containing LFP oscillations, can be filtered to extract LFP bands. The two concepts are easily confused, since they share nomenclature, and in fact, the names are often used interchangeably (27).

On the one hand, little is known about which aspect of neural activity a LFP band reflects. One possibility is that a LFP band reflect the same processes underlying the LFP oscillation that exists in the same frequency range as the LFP band (37). The idea is that when the oscillation is weak, it blends in with other neural dynamics, and the repeating pattern cannot be identified. In this case, the LFP band captures the low level activity of the LFP oscillation. When the oscillatory process is highly active, the repeating pattern stands out, drives a peak in the power spectrum and manifests as a LFP oscillation. Another possibility is that a LFP band reflects a part of the arrhythmic neural activity (38). A typically arrhythmic activity is the scale-free activity, whose dynamics span over many temporal scales (more discussion about scale-free dynamics in "Criticality" section). A LFP band captures a part of the scale-free activity, the part that is survived after the bandpass filtering.

On the other hand, studies have shown that different LFP oscillations likely reflect distinct processes of different scale and strength (27). Low frequency LFP oscillations (<30Hz) may be produced by thalamocortical feedback loops, which are thought to have a long time constant (tens to hundreds of milliseconds), and are thought to be modulated by global neuromodulatory inputs. High frequency oscillations, on the other hand, likely originate from local microcircuits consisting of pyramidal neurons and interneurons.

We will briefly cover our understanding of the origin of gamma oscillation. This is relevant, because studies have suggested that gamma band is the best neural correlate of task-related BOLD, and in these studies gamma band is dominated by the activity from gamma oscillation (39). While pyramidal neurons may be the strongest contributors to LFP due to their size and aligned geometry (as discussed earlier), interneurons are known to play a critical role in gamma oscillation (40, 41). Interneurons, specifically the fast spiking basket neurons, act as gamma rhythm generators by rhythmically inhibiting pyramidal neurons and synchronizing inhibitory synaptic potentials.

The mechanism of gamma rhythmicity in interneurons is unclear. Two conceptual models have been proposed: the inhibition-inhibition (I-I) model and the inhibition-excitation (I-E) model (42). In the I-I model, two sets of interneurons mutually inhibit each other. One set of interneurons begins to fire together and generates synchronous IPSPs in the other set of interneurons. Once the IPSPs have decayed the inhibited neurons will start to fire, switching from being inhibited to inhibiting the first set, and the cycle repeats. In the I-E model, a fast excitation and a delayed feedback inhibition alternate. In reality, I-E and I-I hybrid gamma networks may work together to generate gamma rhythmicity in interneurons.

1.2.2. Slow LFP:

Slow LFP is the slow fluctuation (<1 Hz, sometimes up to 4Hz) of the raw LFP potential. Similar to a LFP band, slow LFP is also a signal extracted by filtering raw LFP signals. Slow LFP is often arrhythmic (not dominated by a particular frequency component) at rest or during rapid eye movement sleep. During slow wave sleep (SWS), slow LFP is often dominated by "slow oscillation", which has a dominant frequency of 0.8 Hz (43). Arrhythmic slow LFP and slow oscillation are covered separately below.

On the one hand, the origin of arrhythmic slow LFP is mysterious. Several studies have suggested that arrhythmic slow LFP is likely related to slow potential changes measured by EEG, which is referred to as slow cortical potential (SCP) (43). A range of neural and non-neural processes might contribute to SCP. The major contributor is thought to be prolonged (on the order of seconds) depolarizations of pyramidal apical dendrites in upper cortical layers (28, 44). Negative SCPs are linked to EPSPs, and positive SCPs are linked to a reduction of EPSPs and sometimes a predominance of IPSPs. Theoretically, neuroglial depolarizations might also contribute to SCP (45). However, glial depolarizations are not spatially aligned (29), and thus they are likely to cancel out each other. Changes in pCO2 also contribute to SCP (46). An increase of pCO2 during hypoventilation evokes a positive shift in SCP.

On the other hand, we have a coarse understanding about slow oscillation. It has been related to up-down states (43). During slow wave sleep (SWS), neuronal membrane potential oscillates between two subthreshold states: a hyperpolarized state ("down") and a hypopolarized state ("up"). During the up state, the neuron is more likely to fire an action potential compared to the down state. The oscillation in membrane potential between these two states produces a slow oscillatory extracellular field potential (slow oscillation). It is worth noting that up-down states

8

can be used to describe a more general phenomenon in which neuronal membrane potentials shift between two states without displaying rhythmicity. The mechanism giving rise to slow oscillation is still under investigation. The current model is that neurons spontaneous enter the up state. This could be due to the spontaneous release of transmitter vesicles at the presynaptic membrane (47). Another possibility being proposed is that extracellular potassium concentration is elevated during SWS and this elevation induces layer V neurons to fire first, rendering the local circuit in the up state (48). During the up state, neurons synchronously burst, leading to afterhyperpolarizations and a return to the down state (43).

1.3. Neural basis of BOLD correlation

Little is known about the neural basis of BOLD correlation. Many of the current assumptions surrounding the neural basis of BOLD correlation arise from our understanding of the neural basis of task-related BOLD. However, there could conceivably be different neural mechanisms underlying task-related BOLD and at-rest BOLD correlation.

1.3.1. Neural basis of the task-related BOLD response

We currently have a rudimentary understanding of task-related BOLD (49). The task-related neural response is linked to an increase in oxygen delivery to nervous tissue via an increase in blood flow and vessel dilation. This increase in oxygen delivery exceeds any change in oxygen consumption due to metabolism, leading to an increase of local blood oxygen level and a decrease in local deoxyhemoglobin concentration due to its conversion into oxyhemoglobin. Deoxyhemoglobin is paramagnetic and creates a small local magnetic field inhomogeneity, thereby reducing the MR signal. Oxyhemoglobin, which like the surrounding

fluid and tissue is diamagnetic, does not have this effect. As a result, a conversion of

deoxyhemoglobin to oxyhemoglobin causes the BOLD signal to increase.

Beyond this rudimentary understanding, investigations are now focusing on

differentiating whether LFP or multiunit spiking activity is reflected by task-related BOLD. LFP

is often viewed as reflecting the synchronized dendritic currents of the inputs to an area, while

multiunit activity is believed to reflect the output of a neural population, because pyramidal

neurons, the most significant contributor to multiunit activity, project outside the local area (50).

Thus, determining whether the task-related BOLD response reflects local field potential (LFP) or

multiunit activity (MUA) can shed light on whether the task-related BOLD response reflects

neuronal input (synaptic activity) or neuronal output (spike activity).

In one such study, Logethetis et al. simultaneously recorded BOLD and

electrophysiological signals in V1 of anesthetized monkeys. They demonstrated that the visually

related BOLD response was correlated with both MUA and LFP power, with the LFP correlation

(r^2=0.52) slightly higher than the MUA correlation (r^2=0.44) (39). Via a specific visual stimulus

and a pharmacological manipulation, respectively, Viswanathan et al. and Rauch et al.

demonstrated that a significant LFP response and a significant BOLD response could be obtained

without evoking a significant MUA response in V1(51, 52), demonstrating that a MUA response

is not necessary to elicit a significant BOLD response. The authors of these studies argued that

the task-related BOLD response is coupled with the LFP response and, thus, reflects synaptic

activity (input) instead of spiking activity (output).

It is worth noting, however, that the MUA responses may in fact contribute to the task-

related BOLD response; no studies address this point. Both MUA and LFP responses are elicited

in most task paradigms. Indeed, Thomsen et al. demonstrated that after pharmacologically

blocking excitatory synaptic input, the rate of local oxygen consumption was largely dependent on the ongoing spiking activity (53). In addition, the reliability of the mapping from electrical signals to neural input or/and output remains a source of debate. Most synaptic inputs (both excitatory and inhibitory) originate from the local neural populations, and only a small minority of inputs come from distant cortical and subcortical structures. This feature of neuronal wiring suggests that the spiking output of a local population of cells contributes the majority of the input to that same population. Thus, local spiking activity, synaptic activity, and dendritic currents likely all co-vary (50). To complicate the matter further, non-neural factors can also influence LFP activity, such as the position of the electrode relative to the neuronal geometry (54). Ultimately, then, the exact relationship between the task-related BOLD response and neural activity is still unclear.

1.3.2. Task-related BOLD versus at-rest (spontaneous) BOLD correlation

Several observations support the idea that the neural basis of the task-related BOLD response may be different from the neural basis of at-rest BOLD correlation, from which BOLD correlation is derived. At-rest BOLD correlation and the task-related BOLD response have different temporal dynamics, suggesting that they may reflect neural activity with different temporal dynamics. It is important to differentiate the dynamics of neural activity underlying these BOLD phenomena and the dynamics of neuro-hemodynamic coupling. The neuro-hemodynamic coupling is sluggish and acts as a lowpass filter. However, it is the dynamics of the neural activity underlying BOLD that is relevant to the discussion.

At-rest BOLD correlation happens at a very slow time scale (10~100s per cycle). BOLD is shown to be able to capture events at a much faster time scale (< 2s), despite the sluggish neuro-hemodynamic coupling (55). The fact at-rest BOLD correlation does not exist in the fast

time scale suggests that neural activity underlying BOLD correlation itself is slow. However, the neural activity underlying task-related BOLD is much faster and can change as fast as tens of milliseconds, though task-related BOLD cannot capture the tens-of-millisecond-scale changes in neural activity because of the non-linearity of neuro-hemodynamic coupling for rapid changing neural events(56).

The energy expended on at-rest activity is believed to be much larger than that expended on task-related activity. Studies using position emission tomography have demonstrated that absolute blood flow increases associated with task-related responses are rarely more than 5%-10% of the resting blood flow of the brain, even for the most arousing perceptual and vigorous motor activity, and the corresponding increase of energy consumption is no more than 1.0%(4). These results suggest that only a fraction of energy consumed by brain is dedicated to task-related BOLD, while the majority reflects at-rest BOLD. In sum, the differences in the temporal dynamics and relative energy budgets between task-related BOLD responses and BOLD correlation suggest that neural activity reflected by BOLD correlations may be different from the neuronal activity reflected by the task-related BOLD response.

1.3.3. Potential neural basis of BOLD correlation

The patterns of connectivity obtained with BOLD correlation have been compared to anatomical data in monkeys, and to anatomical data from diffusion tensor imaging in humans. The comparison of anatomical connectivity to BOLD correlation shows that BOLD correlation is largely predicted by anatomical connectivity but can exist between areas where there is little or no anatomically connectivity((57-61), see review(62)). This suggests that BOLD correlation is not a merely reflection of the anatomical connectivity.

EEG features have been compared to BOLD correlations to provide clues about the neural basis of functional connectivity. Hlinka et al. demonstrate that individual differences in BOLD correlation strength within the default mode network are correlated with individual differences in delta and beta power (63). Lu et al. demonstrate that varying anesthetic doses induce similar changes in both BOLD correlation and delta power coherence (64). Chang et al. demonstrate that temporal fluctuations of different EEG band powers are correlated with temporal fluctuations in the strength of BOLD correlation within specific fcMRI networks, though the polarity of the correlation differs across fcMRI networks (65). Together, these and similar studies link various EEG-derived features to specific fcMRI networks, though the specifics of these findings do not lead to a coherent picture about the relationship between EEG signals and fcMRI. Moreover, interpretation of these results is complicated by the fact that EEG has poor spatial resolution (tens of cubic cm) and imprecise localization of the signal source. Detailed examination of the neural basis of BOLD correlation will require a direct comparison between BOLD correlation and intracranial electrophysiological signals, which have greater temporal and spatial resolution compared to EEG.

A few studies have attempted to address the neural basis of spontaneous BOLD signals from which BOLD correlations are derived. Pan et al. record from rat S1FL and demonstrate that the spontaneous BOLD signal is significantly correlated with both the local infraslow (<0.5Hz) LFP signal (r = ~0.5) and the slow modulations of broadband (1-100Hz) LFP power (r = ~0.4). However, interpretation of their results is complicated by the substantial distortion of their electrical signals due to simultaneous fMRI scanning (66, 67). Aside from rodent studies, only one study in the primate literature has examined the relationship between spontaneous BOLD and neural activity. Magri et al. record from V1 in anesthetized monkeys. Consistent with the

13

results of Pan el al., Magri and colleagues report a significant relationship between the broadband LFP power and spontaneous BOLD fluctuations, using mutual information analysis. In addition, after controlling for the fluctuation of broadband power, they demonstrate that the amplitude of spontaneous BOLD fluctuations reflects changes in gamma power, while the timing of spontaneous BOLD fluctuations reflects beta band power (37). These results provide clues concerning the neural basis underlying spontaneous BOLD signals, at least in monkey V1 and rat primary forelimb somatosensory cortices. However, it is unclear to what extent these results can be generalized to other brain areas when animals are awake, as both BOLD and neural activity differ greatly across behavioral states and brain areas. In addition, these studies focus on the relationship between spontaneous BOLD fluctuations and local neural activity. Investigation of the relationship between local BOLD and local neural activity may not reveal the neural basis for BOLD correlation, as BOLD correlation might reflect an interaction between correlated brain areas, such as the amount of time that neuronal activity is synchronized (68).

Electrophysiological findings by other groups have provided additional clues concerning the neural basis of BOLD correlation. Nir et al. demonstrate that, similar to spontaneous BOLD, slow fluctuations of gamma band power are correlated between left and right auditory cortices in humans, opening up the possibility that BOLD correlation reflects the slow co-fluctuation of gamma band power (69). He et al. demonstrate that the spatial pattern of correlations based on slow (<0.5Hz) fluctuation of LFP is similar to the spatial pattern of BOLD correlations, suggesting that BOLD correlation reflects the co-fluctuation of slow LFP (70). These indirect comparisons between BOLD correlation and electrical signals suggest potential neuronal mechanisms that underlie BOLD correlations. However, direct comparisons between spontaneous BOLD correlations are required before any conclusions can be drawn.

1.4. Two heuristic models of the origin of BOLD correlation

BOLD correlation operates at very slow time scales, in the range of tens of seconds (6). This is several orders of magnitude slower than most neural dynamics (but see (71)). We will briefly introduce two heuristic models, via which the brain generates such slow dynamics underlying BOLD correlation: criticality and oscillation.

1.4.1. Criticality

Criticality is a particular state in which complex systems are balanced between ordered and disordered phases. A hallmark of the criticality point is scale-free dynamics, where the power (or variance) of the dynamics is inversely proportional to the scale: $P \propto 1/f^{\beta}$, where P is the power and f is the temporal scale (or frequency) at which the power is calculated.

A classic example of criticality is the Ising model (38). Consider a set of lattice sites, and there is an electron in each site. The electron spins create a micro magnetic field. Electrons can be treated as small magnetic bars. The orientation of a magnetic bar is influenced by its neighbors, and by thermal fluctuations (random disturbances due to the kinetic energy). At low temperature, the neighbor interaction dominates. As a result, almost all of the magnetic bars align in the same orientation, producing an ordered phase. At high temperature, thermal fluctuation dominates. Magnetic bars all point in different directions, producing a disordered phase.

At some critical temperature, neighbor interaction and thermal fluctuation are balanced. Instead of all spins lining up or all bars pointing in different directions, an intermediate state arises: a constantly evolving landscape of different local domains, and the spins with these domains align. The size and the longevity of individual domain vary widely. Small domains are common while

large domains are infrequent; transient domains are common while long-lasting domains are rare. There is an inverse relationship between the frequency and size of domains: Size $\propto 1/f^{\beta}$. There is a similar inverse relationship between the frequency and duration of domains: Duration $\propto 1/f^{\beta}$. These relationships are referred to as a power-law or scale-free relationship. For systems operating close to criticality, their information communication, information storage, computational power, and dynamic range to inputs are optimized (38). It is important to note that the scale-free feature is a hallmark of the criticality, but it alone is not sufficient to prove criticality.

Several scale-free features have been reported in neural systems, providing evidence that the brain operates at a critical point (72-77). For example, at times a local neural population spontaneously bursts, and the number of neurons activated in each distinct burst follows a power law. Bursting of a small number of neuron is often, but bursting of a large population is rare. These so-called "neural avalanches" have been reported in awake monkeys, anesthetized rats, isolated leech ganglion, and dissociated neural cultures, suggesting a general and robust phenomenon. As a second example, the power of various neural signals, such as local field potentials and BOLD, show 1/f characteristics ($P \propto 1/f^{\beta}$). Third, the topology of connectivity, as assessed by correlations, itself shows a 1/f character. Only a few nodes are strongly correlated with many other nodes outside of their own network ("hub nodes"), while many nodes show a few inter-network correlations (78, 79). Taken together, these findings have inspired a heuristic model in which the slow dynamics underlying BOLD correlation reflect the low frequency end of the scale-free dynamics associated with criticality (72-76).

1.4.2. Oscillators

An alternative model is that the slow dynamics underlying BOLD correlation could be driven by oscillatory modules, perhaps in sub-cortical nuclei. These modules could consist of small sets of cells which generate slow oscillatory patterns of firing that are then transmitted to widespread cortical and sub-cortical regions. Simple oscillator-based models of functional connectivity exist (e.g.(80)). However, most neural oscillators reported operate on a scale of tens to hundreds of milliseconds, which is several orders of magnitude faster than BOLD correlation. Oscillators of tens of seconds (referred to as infraslow oscillators) have been reported in the various thalamus nuclei and deep brain nuclei, such as LGN, nucleus lateralis posterior, and olivary pretectal nucleus (71), though their role in BOLD correlation is unclear.

1.5. Overview

In this thesis, we examine the neural mechanisms underlying large-scale functional organization in the brain captured by at-rest, long-range BOLD correlation. In chapter 2, we develop oxygen polarography as an MR-independent measure of oxygen level and demonstrate that oxygen polarography captures the same physiological phenomenon as BOLD. We also demonstrate that the classic view of neuro-hemodynamic coupling, where task-related oxygen relates to gamma band activity via a linear transformation, likely does not capture the true physiological process. In chapter 3, we differentiate the two heuristic models (criticality versus oscillation) that address the origin of BOLD correlation. We show that functional connectivity is not related to criticality but, instead, to specific and potentially localizable oscillatory processes. In chapter 4, we show that at-rest oxygen correlation reflects correlated spiking activity of

neurons. We show that spiking activity drives slow LFP change, which itself drives oxygen change. Our results provide conclusive support for the idea that at-rest BOLD correlation reflects patterns of neural activity and present significant challenges to the traditional view of neurohemodynamic coupling. In chapter 5, we summarize the work presented in this thesis and describe future directions to further understand the mechanisms and functional significance of BOLD correlation.

Chapter 2: Oxygen level and LFP in task positive and task negative areas: Bridging BOLD fMRI and electrophysiology

Abstract

The human default mode network (DMN) shows decreased blood oxygen level dependent (BOLD) signals in response to a wide range of attention-demanding tasks. Our understanding of the specifics regarding the neural activity underlying these "task negative" BOLD responses remains incomplete. We paired oxygen polarography, an electrode-based oxygen measurement technique, with standard electrophysiological recording to assess the relationship of oxygen and neural activity in task-negative posterior cingulate (PCC), a hub of the DMN, and visually responsive task-positive area V3 in the awake macaque. In response to engaging visual stimulation, oxygen, LFP and multi-unit activity in PCC showed transient activation followed by sustained suppression. In V3, oxygen, LFP and multi-unit activity showed an initial phasic response to the stimulus followed by sustained activation. Oxygen responses were correlated with LFP in both areas, although the apparent hemodynamic coupling between oxygen level and electrophysiology differed across areas. Our results suggest that oxygen responses reflect changes in LFP power and multi-unit activity, and that either the coupling of neural activity to blood flow and metabolism differs between PCC and V3, or computing a linear transformation from a single LFP band to oxygen level does not capture the true physiological process.

Introduction:

The default mode network (DMN) was first identified through human brain imaging as a set of regions in which blood flow decreases, relative to baseline, in response to a wide range of novel, attention-demanding tasks and stimuli (81-84). These "task negative" regions, which include the anterior and posterior cingulate cortices, medial and lateral parietal cortices, and medial prefrontal cortex, are collectively considered to be a network because they show correlated intrinsic BOLD fluctuations even when subjects are at rest (85). The human DMN is believed to instantiate high order cognitive functions, such as self-referential thinking, social cognition and episodic recall (86). Altered BOLD fMRI activity in the DMN has been linked to neurological and psychiatric disorders, such as schizophrenia and depression (87). Yet, substantial gaps exist in the understanding of how BOLD is related to the underlying neural activity in the DMN. We address this issue in the current study.

The macaque brain includes a network that is homologous to the human DMN. As in humans, the macaque DMN exhibits spontaneously correlated intrinsic activity in the absence of task performance (10, 61, 88, 89). These regions also exhibit task negative responses in a variety of behavioral paradigms (90, 91). However, these task negative responses have appeared to be less reliable than those in humans. In humans, task negative responses in the DMN are a robust finding in many PET and fMRI studies. In monkeys, task negative responses in PET differ substantially across animals and tasks (90), and task negative responses in fMRI have been reported only in a meta-analysis that combines data from 8 individual studies and 15 experiments (89); none of the individual studies reported task negative effects. The difficulty of observing task negative responses in macaques compared to humans could reflect a species difference,

perhaps related to differences in how the DMN is used in the two species (92). Alternatively, however, the difference may reflect the fact that animals are extensively trained and reinforced to hold still and fixate during fMRI data collection. As a result, animals may never fully disengage with the environment and may never fully engage their DMN.

Although it is generally accepted that BOLD signals reflect neural activity ((37, 39, 93-103) reviewed by (104)), gaps remain in our understanding of the specific neural activity that underlies task-induced fMRI responses. Simultaneous BOLD fMRI in combination with electrophysiology requires highly specialized equipment unavailable to most (39). Studies in monkeys and rodents that have compared BOLD fMRI and high resolution invasive electrophysiology have focused on primary visual and somatosensory cortex, i.e., "task positive" brain areas that show increased activity in response to particular stimuli or tasks; moreover, most of these studies have been done in anesthetized animals (39, 95, 96, 105, 106). As far as we are aware, simultaneous fMRI-electrophysiology has not been performed in any node of the DMN. Two studies in macaques and a handful in humans have recorded electrophysiology in the DMN, but the findings were not directly linked back to BOLD fMRI (93, 107-112). Direct comparison of BOLD fMRI and invasive electrophysiological task-negative responses obtained from identical locations under identical task conditions has not been done.

To directly compare task negative BOLD responses in macaques to the underlying neural activity, we used oxygen polarography as a surrogate for BOLD fMRI. Oxygen polarography is an electrode-based technique for measuring tissue oxygen that can be readily combined with standard macaque electrophysiology. The spatial specificity and temporal resolution of our oxygen polarographic system far exceed those of fMRI and are comparable with the scale of the electrophysiology. We used this system to record oxygen level and local field potentials (LFP)

in posterior cingulate cortex (PCC), a hub of the DMN (113), and in task-positive area V3. Monkeys sat in a quiet, dark room with minimal restrictions and naturally entered a "resting" state during the long (30s) intertrial intervals. Every 45 s they were engaged by 15 s of whole-field visual stimulation. This stimulus drove increases in both oxygen level and LFP power within V3. In PCC, stimulation produced a transient increase followed by a sustained decrease in both measures. Oxygen and LFP responses were clearly related across a wide range of LFP frequencies in both regions. However, the specifics of LFP oxygen relationship differed between the two regions.

Materials and Methods:

Oxygen Recording: Oxygen polarography was introduced to neuroscience in the mid 20th century but went out of favor long ago (114). It has recently been reintroduced and has been used to study oxygen changes in sensory areas and the cerebellum (115-118). Polarography is an electrochemical technique. When the voltage of a noble metal cathode is held at around -0.8 V relative to a reference electrode, the primary half-cell reaction is reduction of oxygen. The reaction rate is limited by oxygen concentration, and thus the current required to maintain the polarization is proportional to oxygen concentration (119, 120).

We utilized specialized platinum microelectrodes suitable for both oxygen polarographic redox control and electrophysiologic recording (FHC instruments) as a cathode. An Ag/AgCl reference electrode (Grass Technologies) was placed on the back of the head at a location with minimal underlying musculature and no response to body or limb movements. The skin was lightly abraded to minimize sweat and movement potentials, and a layer of Ten20 EEG paste was

23

applied. A commercial voltage clamp (Unisense PA2000) provided a measure of the clamping current. Our system allowed simultaneous oxygen recording at four sites with a temporal resolution from 0 to 20 Hz and a spatial specificity of 30-100 microns (120). We could then record LFP and multi-unit activity from these same electrodes by disconnecting them from the voltage clamp and connecting them to standard electrophysiologic amplifiers.

Animals, Behavior, Stimulus: Two macaques served as subjects in this study. Animals were cared for and handled in accordance with the *Guide for the Care and Use of Laboratory Animals*, and all procedures were approved by the Washington University Animal Studies Committee. During recording, macaques were fully hydrated and sat head-fixed in a dark room facing a wide field textured screen. Behavior was unconstrained, and the animals had no expectation of a task or reward. Every 45 seconds, 15 seconds of dim 1 Hz stroboscopic illumination with a 0.5 s duty cycle was presented. Illumination filled ~45 degrees of visual angle directly in front of the animal, and contained low frequency spatial contours (blurred shadows) due to the projector. This blurring is visually equivalent to applying a 2-pixel radius Gaussian filter to a 256-pixel by 256-pixel image (e.g. Supplementary Figure S1). Each 15 s stimulus period and subsequent 30 s rest period was considered one trial. On one-eighth of trials, an auditory tone was sounded at the onset of the visual stimulus. Responses on trials with and without tones were similar and so were pooled in the analysis (below).

Animals naturally relaxed in between stimulus presentations. During the interstimulus period the velocity of spontaneous eye movements typically slowed and the eyelids often partially or fully closed (37% of the time, monitored using an ISCAN camera and software (ETL-400)). With each onset of the visual stimulus, even though there was no explicit task, animals opened their eyes and made high velocity saccades toward the stimulus. Thus each trial

contained two distinct states: aroused and engagement with an external stimulus, and unstimulated "resting" interstimulus periods in which animals appeared disengaged from the external world and drowsy.

Recording: The brain was accessed via bilateral 15 mm (internal diameter) chronic custom recording chambers custom manufactured from Delrin and stabilized using a poly methyl methacrylate headcap affixed to the skull with ceramic screws (Thomas Recording GmbH). T1 weighted MRI images (MPRAGE; .5 mm isotropic voxels) were obtained using a custom phantom in the chamber that provides visualization of the chamber and allows for the virtual projection of a chamber-based coordinate system down into the brain. Two small manganese injections were placed in each monkey to determine the alignment of our chamber coordinates with the brain anatomy (Supplementary figure S2A). Prior to data collection, we used MRI images from each animal and standard atlas definitions (121) to target PCC and V3 in the left and right hemispheres (Supplementary figure S2B). We then recorded local field potentials and multi-unit activity in and around the targeted areas, refining the boundaries based on the extent of negative and positive electrophysiological responses to visual stimuli in PCC and V3, respectively. During data collection, for each recording session, four specialized platinum microelectrodes were inserted into left and right PCC and V3 with a multi-electrode micro-drive (NAN Instruments, Inc.). Placement in gray matter was confirmed by multi-unit activity. Electrodes were referenced to a metal guide tube that traversed the soft tissue outside the brain and just penetrated the dura.

We recorded from 23 and 21 sites in PCC and V3, respectively. Oxygen and LFP were recorded serially. At each site, 15 to 40 trials (45 s cycles of alternating stimulation and quiet rest in the dark) of LFP were collected. Next, we polarized the electrodes (see above), waited 30

minutes to ensure electrochemical stability and then collected 45 trials of oxygen data at each site. In total, data were obtained from 1025 and 942 trials for oxygen, and 605 trials and 607 trials for LFP, in PCC and V3, respectively. Oxygen was lowpass filtered at 20 Hz, LFP was lowpass filtered at 300 Hz, and both were sampled and stored at 1 kHz using the Plexon MAP system (Plexon Inc).

Analysis: Oxygen polarographic signals, like BOLD signals, reflect relative rather than absolute oxygen levels. The polarographic current values were therefore, like fMRI BOLD data, expressed as percentage deviation from baseline. Baseline was defined as mean of the last 5 s of all trials. LFP data were converted to the frequency domain using the continuous wavelet transform. The mother wavelet used was a complex Morlet wavelet:

$$Complex\ Morlet(x) = \left(\frac{1}{\sqrt{2\pi}}\right) * e^{(i2\pi x)} * e^{-\frac{x^2}{2}}$$

Supplementary figure S3 shows that the temporal smoothing of this method is proportional to the period of the estimated frequency, with more temporal smoothing for lower frequencies. Similar to oxygen, the power in each frequency band was expressed as percent deviation from the power in that band during baseline. Oxygen and LFP signals were then averaged across trials, recording sites, and monkeys. Prior to averaging, each trial's response was offset by the mean of the last 5 s of the previous and current trial. This removes low frequency effects such as linear trends that effect response variance but has no effect on the mean response.

In order to compare the relationship between oxygen and neural activity, we assessed the lagged cross correlation between oxygen and LFP. For statistical analysis, the bounded distribution of Pearson's r values was shifted to a normal distribution using Fisher's z transform.

For the analysis illustrated in Figure 5, rows 1 through 4, standard hemodynamic response functions (the sum of two gamma functions) were generated using the SPM5 fMRI Matlab toolbox (http://www.fil.ion.ucl.ac.uk/spm/software/spm5/) and to fit the data: a canonical hemodynamic response function (HRF) based on empirical data from visual stimulation in humans, with a single free scale parameter (122), and a generic HRF with all eight parameters of the two gamma functions free. These functions have previously been used to relate LFP and hemodynamic signals (123, 124). Free parameters were fit by minimizing the squared deviation of the predicted and observed oxygen responses.

To provide a model-free approach to assessing the relationship between oxygen and LFP power, transfer functions were computed using linear systems theory. The fast Fourier transform (FFT) of the oxygen signal was divided by the FFT of the LFP signal, and the result was inverse Fourier transformed. This process derives a mathematically exact convolution kernel that converts the LFP signal to the estimated oxygen signal. (Figure 5, rows 5 and 6). However, assumptions inherent to the FFT lead to over-fitting in frequency domain of real world signals, which can lead to artificial zeroes in the FFT. When zeroes occur in the FFT of the denominator (FFT(LFP)) they result in artificially inflated frequencies in the transfer function that obscure visualization of its primary behavior. To reduce the impact of over-fitting, we multiplied each signal by 25% Gaussian white noise prior to computing the FFT, which regularizes the frequency domain representation of the modeled signal by reducing artificial zeroes. To remove effects of the white noise on the estimated kernel we repeated this process 500 times and took the mean result. To further focus on the primary features of the kernel we then low pass filtered the transform at 0.27 Hz (125).

Results

To investigate the relationship between BOLD responses and neural activity, we recorded local oxygen level and LFP serially from V3 and PCC of two macaque monkeys at rest and engaged by a visual stimulus. V3 is a visually responsive "task-positive" brain region. PCC is a "task-negative" brain region expected to decrease activity during task engagement (91). Visual stimulation consisted of 15 to 45 repetitions of 15 s of 1 Hz stroboscopic low spatial frequency patterned illumination. Each stimulus was followed by 30 s of darkness to allow the macaque to return to a baseline (unstimulated) resting state. Animals were head-fixed and seated in a primate chair but were otherwise unrestrained. No rewards were delivered. Visual monitoring and eye tracking under infrared illumination confirmed that they were engaged with the stimulus when it was presented, and otherwise were relaxed and drowsy, partially or fully closing their eyes 37% of the time. The basic results described in the paper were similar for the two monkeys, and they were combined.

Visual stimulation resulted in an increase in mean oxygen level averaged over the stimulus response compared to baseline of $0.77 \pm 0.08\%$ in V3 and $-1.82 \pm 0.21\%$ in PCC ($P<0.0001$). The results in the two monkeys were similar to each other (in V3, $F_{(1,20)} = 0.62$, p $= 0.4$; in PCC, $F_{(1,22)} = 1.13$, p $= 0.3$). In V3, the oxygen level increased after a short delay, peaking at 2.0% above baseline 6.2 s after stimulus onset. Oxygen then decreased to a sustained level of 0.3% above baseline during stimulation. A second peak of 0.7% occurred 3.2 s after the final flash, followed by 9.4 s of values below baseline. In PCC, there was an initial positive response that was indistinguishable for the first 3.1 s from the initial positive response in V3. The initial PCC response peaked at 1.1%, 3.7 s after stimulus onset. PCC oxygen then decreased

sharply, falling to -2.5% below baseline at 11.7s and remained negative for 15.4s after the end of stimulation (Figure 1). Oxygen responses were similar in the two monkeys (Supplementary Figure S4). These results, obtained from oxygen polarographic measurements in monkeys, are similar to the results obtained from BOLD measurements in humans under similar circumstances (126-128).

Changes in oxygen level lagged but otherwise qualitatively tracked the stimulus-evoked changes in LFP power recorded from the same electrodes used for polarography. Figure 2A shows that, like oxygen, LFP power increased in V3 and decreased in PCC during stimulation overall. Increases in power greater than two standard errors above baseline are shown in yellow and red, and decreases are shown in blue. Figure 2B shows the mean (± SEM) change in LFP power as a function of frequency during the period 5-15 s after the onset of visual stimulation relative to the subsequent 30 s of darkness. Supplementary figure S6A shows the LFP power during the visual stimulation and the subsequent 30s of darkness. The LFP power change was similar in the two monkeys at most frequencies, except 8-32 Hz in V3, where there was a trend towards weaker modulation in Monkey 1 compared with Monkey 2 (Supplementary Figure S7 and p values in Supplementary Figure S5). In V3, LFP power is significantly increased at frequencies above 16 Hz and significantly decreased from 4-16 Hz. A similar pattern has been reported in other monkey electrophysiology studies, e.g. (129). In contrast, LFP power in PCC was suppressed across the entire frequency range (1-150Hz), with the magnitude of the suppression varying by frequency.

LFP power modulation showed many temporal and spectral features that were not visible in the oxygen response. To examine these responses in detail, we collapsed the LFP response

29

into near-logarithmic bands that approximate the common EEG frequency ranges (Figure 3): Delta: 1-4Hz, Theta: 4-8Hz, Alpha: 8-16Hz, Beta: 16-32Hz, low Gamma: 32-64, and high Gamma: 64-150Hz. We did not find well separated rhythms with distinct dynamics corresponding to common EEG frequency ranges (Supplementary figure S6 and Figure 2B). Instead, the LFP response patterns changed slowly with frequency, so that the precise boundaries of these bands had only minor effects on the results.

Across all bands in both V3 and PCC, there was an increase in LFP power at stimulus onset. Onset response magnitude was roughly similar in the two regions. Following the onset response, the LFP responses markedly differed. We separated the LFP responses into tonic modulation and phasic responses to each flash. Tonic LFP power modulation was evaluated as the mean power during the inter-flash intervals (100 ms prior to each flash, averaged over the stimulation period) relative to the power in the inter-trial interval. In V3, the tonic power was elevated in Gamma and Delta (both $P<0.0001$, suppressed in Theta and Alpha (both $P<0.0001$), and weakly though significantly suppressed in Beta ($P<0.0001$). As noted in the Methods section, the method used to estimate the power also smooths (low-pass filters) the data. This effect is largely negligible in the time scale we are interested in, except for Delta band, where the smoothing has a full width half height of 900 ms (Supplementary Figure S3). Thus, the fact that power in the Delta band shows a tonic increase could be an artifact of the combination of a phasic increase with each flash, plus temporal smoothing, rather than a true activation of Delta band frequencies that is sustained across the inter-flash intervals. Differentiating these two possibilities is beyond the scope of this study. In PCC, all bands showed tonic suppression (all $P<0.0001$).

How long it took to reach the tonic level of LFP power, and how long the tonic level was sustained after the end of the stimulus, varied across frequency bands (Figure 3). In V3, tonic increases in power in the Gamma and Delta bands occurred immediately following stimulus onset. Gamma power was maintained at a constant level for 0.7 s after the end of stimulation before falling to baseline, while Delta power dropped almost immediately to a pronounced post-stimulation undershoot. Tonic decreases in V3 power (Alpha and Theta bands) showed much slower dynamics, evolving over the first several flashes and remaining depressed for 1.8 s before returning to baseline. In PCC, tonic suppression developed and decayed slowly in all bands, reaching its peak after several seconds and returning to baseline ~8 s after the last flash. As in V3, tonic LFP dynamics in PCC varied with frequency. The time to peak tonic suppression depended on the frequency band (analysis of variance, $F(5,3624)= 4.31$, $P <0.001$). The slowest development of tonic suppression was in the Beta and low-Gamma range.

Phasic responses to each cycle of the flashing stimulus were superimposed on the tonic LFP power modulations. We were particularly interested in the phasic responses at steady state, and so averaged the LFP responses to the fourth through fifteenth flashes in each area (Figure 4). The late flash-triggered average was aligned so that the mean power in the interval 100 ms prior to each flash was set to zero. There was an abrupt increase in power at the onset of each flash, with additional ripples just before and after flash offset. Phasic responses were present at all frequencies in both regions; however, they were approximately 10 times larger in V3 than in PCC. The strongest phasic responses occurred at higher frequencies in V3 compared to PCC (high Gamma versus Beta, respectively). In addition to phasic responses in LFP power, LFP also showed consistent visually evoked potentials in both V3 and PCC. Each cycle of the stimulus evoked a response, and these responses were similar across time, that is, the potential evoked by

the first flash was similar to the potential evoked by each of the later flashes (Supplementary Figure S8A). Removing the mean evoked potential has minimum effect on LFP power responses, suggesting that neither tonic nor phasic responses result from the evoked potentials (Supplementary Figure S8B).

Oxygen responses did not match the phasic responses in LFP power or evoked potentials, but they did roughly match tonic LFP responses. Oxygen level increased in V3 and decreased in PCC (Figure 1). Phasic LFP responses were positive in both regions, and showed complex patterns that were not directly reflected in the oxygen signal. In contrast, the tonic LFP responses behaved similar to oxygen level, generally rising in V3 and falling in PCC. Note that both oxygen and LFP power showed an initial positive response in PCC that was sustained for longer than the phasic flash responses.

Next, we quantitatively evaluated the relationship between oxygen level and LFP power in each area. Prior studies suggested that hemodynamic responses are most consistently correlated with Gamma band LFP (104). To test this relationship, we computed the linear correlation between trial-averaged oxygen and trial-averaged Gamma band LFP power responses. Since fMRI BOLD and our own recordings suggest that oxygen responses are lagged compared to neuronal activity, we computed the cross correlation at lags from -7 to +12 s. Gamma band power was highly correlated with oxygen in both V3 and PCC. In V3, the highest correlation coefficient was 0.68, occurring at a lag of 3.1 s. In PCC, the highest correlation was 0.72 at a lag of 4.3 s. These correlation values are slightly higher than those reported in previous studies, though the lags are similar (37, 97, 130, 131). The lag in PCC was significantly longer than in V3 ($P<0.0001$).

To further quantify the relationship between oxygen and LFP signals, we used three classes of functions to predict the oxygen response based on the Gamma-band LFP response (50-100Hz, spanning both Low Gamma band and High Gamma band). We convolved the Gamma-band LFP signal with each candidate function, adjusting parameters to minimize the mean squared error between the result and the observed oxygen response. First we used a canonical hemodynamic response (HRF) used extensively in the BOLD-fMRI literature (see Methods) (Figure 5, top two rows). Fits were performed by adjusting a single scale parameter for each area (see Methods for details). The best fit prediction explains a significant portion of variance in PCC (r^2 = .85) but only half of the variance in V3 (r^2 = 0.53). In each area, the predicted response (red and blue lines, far right column) fails to capture the initial onset response and subsequent transients (shading). Because of the poor fit with the one-parameter function, we next tried a generic HRF with eight free parameters (see Methods). The eight-parameter fit did well in both areas (rows 3 and 4), though significantly better in PCC than V3 (r^2=0.94 in PCC, r^2=0.85 in V3, P < 0.05). Finally, we estimated a true transfer function using a variant of Fourier deconvolution (see Methods). As expected, the computed transfer function performed well in each area.

With each of the three classes of functions used to predict oxygen level, the best fit function (column 2) differed substantially between regions. For the canonical HRF (1-parameter fit, rows 1 and 2) the scale parameter was 3.5 times larger in PCC than V3, a significant difference (as seen in the difference in the height of the orange versus cyan curves in column 2; P<0.005). With the generic HRF (8-parameter fit, rows 3 and 4) the function shapes were very different in the two areas. The best fit for PCC had a prominent initial negativity compared to the V3 fit, and the scale parameter was again significantly greater for PCC compared to V3 (3.5

times, P<0.005). Finally, the calculated transfer functions also were very different in the two areas (rows 5 and 6). As with the eight-parameter fits, the transfer function for PCC showed an initial negativity that was not present in V3, and the overall amplitude was much larger for PCC than for V3. The difference in the transfer function between V3 and PCC was present in both monkeys, although there were differences in the exact shape of the transfer function in each individual animal (Supplementary Figure S9).

These results demonstrate that the linear transfer function from Gamma band LFP power to oxygen level differs across areas. This result means that one or more of the following are true: hemodynamic coupling differs in PCC and V3, coupling is not driven by or is not well correlated with Gamma band LFP power, or coupling involves a more complex (non-linear) transformation. Several previous studies have shown that multiple frequency bands are correlated with BOLD, independent of Gamma band power (37, 132-134). This was also the case for our data. We found that LFP was correlated with oxygen at most frequencies, with no single band standing out as correlated particularly better than the others (Figure 6a). In V3, both high (>16Hz) and low (<8Hz) frequencies were positively correlated with oxygen, and middle frequencies (8 – 16Hz) were negatively correlated with oxygen. The correlation pattern (negative correlation around Alpha band range) is consistent with previous studies of primary visual and motor cortex (task positive areas) (37, 132-134). The highest correlation between LFP and oxygen (r = 0.68) was found at an LFP frequency of 58 Hz. However, this was not a clear peak; the correlation was nearly as high (above 0.60) from 1 to 2 Hz and from 38 to 86 Hz. In PCC, the highest correlation (r = 0.74) was at 4Hz. As in V3, this was not a clear peak, with correlations above 0.60 from 1 to 12 Hz and from 58 to 150 Hz. Note that in PCC, all frequencies (including Alpha band) were positively correlated with oxygen, which is a different correlation pattern compared with V3.

The fact that Alpha band LFP is negatively correlated with oxygen in V3 but positively correlated with oxygen in PCC suggests that, if a linkage exists, it differs between the two areas.

Since the oxygen signal changed smoothly while the LFP power envelope changed rapidly and correlation may have been reduced by mismatched frequency content, we recomputed the correlations after 1 Hz low pass filtering of the LFP power. This filtering had only a minimal effect on correlation. Even after low pass filtering, no single LFP frequency or band in either area emerged as clearly better correlated with the oxygen signal than the other LFP frequencies.

Having confirmed that many LFP bands were correlated with oxygen level, not just Gamma, we asked if *any* LFP band showed a relationship with oxygen that was similar in V3 and PCC. We repeated the analysis of Figure 5 for each area and for each LFP band. In no case were the fit parameters or transfer function similar for the two areas (Figure 6b).

Several previous studies have suggested that a combination of Alpha band and Gamma band may better explain oxygen responses, and the combination may lead to a consistent transfer function across areas (37, 132-134). We tested this idea by computing the transfer function using a combination of Gamma power and the negative of Alpha power. The negative sign for Alpha power is to be consistent with the negative correlation between Alpha power and BOLD (37, 132-134). The resulting transfer functions differed greatly between two areas, even more than the transfer functions based on Gamma band power alone (data not shown).

In sum, quantification of the LFP-oxygen relationship demonstrated a strong link between neural and oxygen activity. Gamma band LFP power, as well as the power at most other frequencies, was linearly correlated with oxygen level in both V3 and PCC. However, the

35

best-fit linear transfer function for PCC was substantially different from the best-fit function for V3 at every frequency from 1 to 150 Hz. These results suggest that either the nature of the relationship between neural activity and oxygen level differs between brain areas (135, 136), or that evaluating the relationship between the power modulation of single LFP frequency bands between 1 to 150 Hz and oxygen misses the mark and does not capture the true neural correlate of the oxygen response (see Discussion).

Discussion

We recorded local oxygen level and local field potentials (LFP) using oxygen polarography and electrophysiology in the awake macaque. Visually-driven polarographic oxygen responses in both V3 and PCC were similar to BOLD fMRI responses obtained under similar conditions (39, 128, 137). This result indicates that oxygen polarography is a high resolution, electrophysiologically compatible surrogate for BOLD fMRI. Attention to a visual stimulus suppresses both oxygen level and LFP power in PCC compared to a "resting" baseline, demonstrating that macaques not only have a default mode network, as previously described in resting state fMRI studies (61), but also that the PCC exhibits a reduction in electrophysiological activity and oxygen level when the monkey engages with the external environment. Finally, oxygen and LFP responses were correlated in both V3 and PCC. However, the nature of the linear LFP-oxygen relationship differed substantially across regions (99). These results demonstrate that either hemodynamic coupling differs in PCC and V3, or that a simple (linear, single LFP band) transformation is inappropriate for predicting oxygen level from neuronal activity.

Oxygen polarography and BOLD fMRI

Oxygen polarography and BOLD fMRI both reflect oxygen level in the brain. BOLD fMRI signal intensity reflects the inverse magnitude of local magnetic field distortions caused by deoxyhemoglobin (138-140). The concentration of deoxyhemoglobin is inversely related to blood oxygen (2). Oxygen polarography measures available oxygen around the tip of the electrode, which in our study sits in tissue, not blood (94, 141). However, blood and tissue oxygen are generally in equilibrium and BOLD and polarographic oxygen signals should track one another (142).

In practice, we find this to be true: polarographic oxygen closely resembles human BOLD fMRI responses obtained under similar conditions (Figure 1). The oxygen time-course in V3 is similar to that observed in humans in response to sustained visual stimulation in early visual areas (143-149) and is consistent with previous data from macaques (39, 150, 151). Each of these studies shows a sustained BOLD response. A few also show an initial phasic response (146-149). The presence of a phasic response may depend on the specifics of the visual stimulus. For example, Uludağ et al. show both a phasic response and a sustained response in response to a long duration stimuli (20-s of stimulation followed by a 40-s of darkness), whose temporal structure is similar to the current study (149). The PCC oxygen time-course is also consistent with human data (82, 83, 146, 152, 153). Thus, to a first order, polarography and BOLD fMRI provide comparable measurements.

Polarographic and BOLD fMRI measurements operate at widely different spatial and temporal scales. Owing to physiologic (vascular) and technical limits, BOLD fMRI at 3 Tesla (3T) is commonly limited to sampling volumes 2-3 mm on a side at 1-3 s intervals, though

spatial resolutions of up to 1 mm on a side and temporal resolutions of up to 2.5 Hz (with 2 mm voxels) are possible (154, 155). In contrast, our polarographic system samples spherical volumes 30-100 microns in diameter, which are more than 3 orders of magnitude finer than BOLD voxels. Temporal frequency is limited by a lowpass filter set to 20 Hz. The higher temporal resolution of polarography can resolve potential changes in oxygen level within the capillary bed that are invisible to fMRI (2). It also improves our ability to separate neural signals from artifact generated by head motion and cardio-pulmonary pulsations (156, 157).

Oxygen polarography shares limitations with intracranial electrophysiology (e.g., limited coverage, invasiveness, and a requirement to stabilize the head), but also offers significant advantages. Awake macaque fMRI requires significant training to control animal behavior in the fMRI environment, requires that the animal keep still during data collection, and makes rewarding the animal problematic, since any movement that accompanies accepting a reward, even swallowing, will substantially degrade the fMRI signal. This severely limits animal experiments that can be performed with BOLD fMRI. In contrast, oxygen polarography is relatively insensitive to movement. Moreover, adding electrophysiological recording to BOLD fMRI is technically demanding, while adding electrophysiology to polarography is straightforward and provides a match of the spatial specificity of the two signals that is difficult to achieve with fMRI.

The default mode network in monkeys

Only two of the many imaging studies in monkeys have reported a key feature of the human DMN: suppressed activity during external engagement compared to a resting state (90, 91). In one of these studies, the data differed substantially across subjects, and the other required

a meta-analysis of eight independent studies in order to reveal the effects. This would seem to suggest that task negative responses in monkey DMN are less robust than in human DMN. However, our polarographic study provides evidence that this failure reflects a methodological issue rather than a true species difference. Adult humans can be verbally instructed to remain still in the magnet, but monkeys must be specifically trained and then periodically rewarded to remain still. A simple fixation task appears to be far more effortful for even a well-trained animal than for a human (unpublished observations based on error rates in trained subjects). We suggest that sitting still and maintaining fixation in expectation of reward requires, in a monkey, substantially more engagement with the external environment than a similar task in a human. If this is true, then the failure of previous studies to demonstrate a robust negative BOLD response in PCC may reflect their use of an inadequate task negative condition, that is, a task condition that required substantial engagement of the animal with the external environment.

In this study, we used tasks that were more suitable for producing a large contrast between states. With a long interstimulus interval and without the requirement to remain still and fixate for a reward, macaques naturally rest, reducing their engagement with the external environment. When this resting state was interrupted by an externally engaging visual stimulus, we observed clear suppressions in local oxygen level, LFP power and multi-unit activity in PCC (Supplementary Figure S10). These results demonstrate that simian and human default mode networks are both markedly more active at rest than during external engagement. It is true that the "task" in our study was merely passive viewing of a visual stimulus. The animals were not required to perform any particular action. However, we observed, and confirmed via eye tracking, that animals oriented towards the stimulus on the majority of trials. Orienting towards a target is *prima facie* evidence that some degree of attention has been allocated. In any case, our

results indicate that an engaging stimulus, compared to a period of no stimulation, is sufficient in the monkey to evoke a negative oxygen response in PCC. More generally, our results demonstrate the potential for our oxygen polarographic platform, deployed under various experimental conditions, to investigate the functions of the macaque DMN and in particular which functions, or what neural activity, correlate with BOLD activity."

Neural basis of BOLD responses

The physiological basis of task-induced positive BOLD responses is relatively well understood (158, 159). Increased neural activity leads to an increase in metabolic demand, followed by an increase in oxygen supply via an increase in blood flow. The increase in oxygen supply exceeds the increase in oxygen consumption, leading to a decrease in the local concentration of de-oxyhemoglobin and, hence, an increase in the T2*-weighted fMRI (BOLD) signal.

The physiological basis of task-induced negative BOLD responses, like those we report here, may be more complicated (160). However, the most straightforward view is that the mechanism accounted for task negative responses is similar to the mechanism for task-induced positive responses.. In support of this view, a handful of studies have reported task-related suppression of electrophysiological activity in default mode regions (93, 100, 107-110, 112). However, none report BOLD or oxygen responses under matched conditions, and the tasks used had very different temporal structure than those used in typical imaging studies of the default network (but see (93, 100)). We observed concomitant oxygen level and LFP power decreases during visual stimulation in PCC (Figure 1-3). LFPs are thought to reflect synchronized currents within spatially-aligned dendrites from both excitatory and inhibitory neurons (50). Thus, our

results support the hypothesis that default mode BOLD suppression reflects suppression of neural activity and a concomitant decrease in oxygen supply.

In PCC we observed an initial increase in both oxygen level and LFP power in response to stimulus onset followed by sustained suppression (Figure 1). The initial increase in oxygen was identical to that seen in V3, which is especially notable given the high temporal resolution of our method. Similar increases have been previously observed in human fMRI (128, 146, 152, 161-163). We also observed phasic increases in LFP power within PCC with each flash of the visual stimulus (Figure 4). The initial and subsequent phasic increases in LFP power suggest that at least two neural processes, one task-positive and one task-negative, co-exist in PCC during visual stimulation.

Neuro-hemodynamic coupling

Our analysis suggests that the relationship between oxygen and LFP differs across areas (Figures 5 and 6b). For example, the linear transfer function relating Gamma band power with oxygen contains an early negativity for PCC but not V3 (Figure 5, row 6, middle column). The early decrease in oxygen in response to a stimulus may reflect a local increase in oxygen consumption that precedes an increase in regional blood flow (164-166). Alternatively, the initial negativity in the PCC transfer function could reflect a linear approximation to a complex non-linear relationship. The BOLD response to repeated stimuli presented closely together in time is non-linear (167), (although Siero et al. attribute most of this non-linearity to neuronal processes (168)). Different non-linearities in PCC versus V3 could give rise to an initial negativity in one function but not the other.

41

More generally, we assumed in our analysis that neurovascular coupling was a linear process involving a single LFP frequency band. A more complete analysis would consider non-linear combinations of all LFP bands, including those well below 1 Hz, multi and single unit activity and phase relationship between units and field potentials. Such an analysis is confounded by the infinite number of possible non-linear transformations, which guarantee the ability to find transfer functions that are identical across areas (See Supplementary Text for an illustration). To avoid this confound, transformations would need to be cross-validated using data collected under different experimental conditions.

Following changes in neural activity, cerebral blood flow (CBF), cerebral blood volume (CBV) and cerebral metabolic rate of oxygen ($CMRO_2$) all change with different spatial and temporal dynamics. Each of these factors may influence tissue oxygen level. In this study, we show a scale difference in the relationship between oxygen and LFP in V3 compared to PCC; however, further work is required to determine which factor(s) contribute to the scale difference.

In conclusion, we demonstrate that oxygen and LFP responses are closely related to each other in both V3 and PCC (Figure 1 and 2a), supporting the idea that oxygen level and neural activity are closely related to each other in both V3 and PCC. A simple linear transformation of Gamma band LFP power accounts for 85% of the variance in the oxygen signal in our task (Figure 5, rows 3 and 4). The relationship is not specific to the Gamma band, but instead is present over a wide range of LFP frequencies (Figure 6a). Finally, we show that the details of the relationship between oxygen and LFP responses differ across areas, at least for single frequency band, linear transformations (Figure 5). For example, an initial dip is present in the PCC transfer function but not in the V3 transfer function, and the computed hemodynamic efficiency (the ratio of how much oxygen level changes for a given change in LFP power) is 2-4

42

times greater in PCC than in V3 (Figure 5 and 6b). This implies that the relationship between neural activity and oxygen either varies across regions, is a non-linear function of LFP power, reflects frequencies outside of the standard LFP range, or some combination of these possibilities. The ability to combine polarographic oxygen recording with electrophysiological recording in the awake behaving primate provides a platform for testing each possibility.

Acknowledgments

Figures

Figure 1
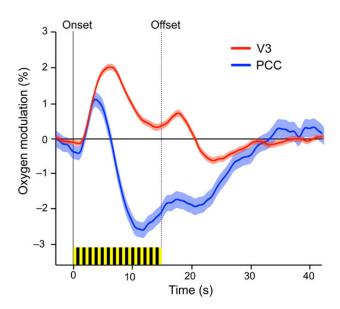
Figure 1. Percent oxygen modulation (mean ± SEM) relative to the period 0-5 s before stimulus onset.

Yellow-black bars mark the 15 s, 1 Hz stroboscopic stimulus. Both areas show a 2.3 s delay followed by an increase in oxygen, peaking at 3.7 s in PCC and 6.2 s in V3. This is followed by a sustained positive response in V3 and a sustained negative response in PCC. After the stimulus is turned off there is a late suppression in both areas followed by a return to baseline at ~15 s after the end of stimulation. Data from 1025 and 942 trials are included in the PCC and V3 traces, respectively.

Figure 2
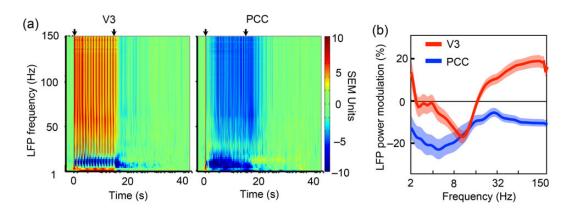
Figure 2. A. LFP power modulation relative to baseline (0-5 s before stimulus onset) in standard error units (SEM is estimated based on baseline activity).

Arrows indicate stimulus onset and offset. Data from 607 and 605 trials are included for V3 (left) and PCC (right), respectively. B. LFP power modulation (mean ± SEM) as a function of frequency (log) during stimulation for V3 and PCC.

Figure 3
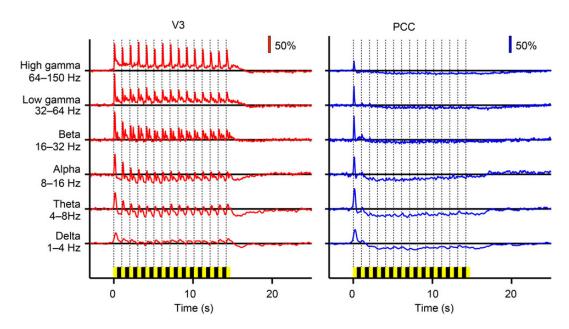
Figure 3. Percent modulation of LFP power for standard EEG bands.

V3 shows complex phasic responses riding on top of tonic increases (Gamma, Delta) and decreases (Alpha, Theta) in power relative to baseline. PCC shows smaller phasic responses and tonic decreases.

Figure 4
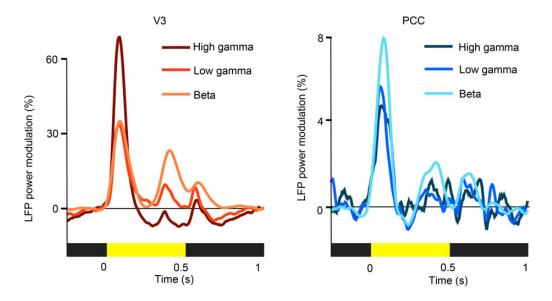
Figure 4. Flash-triggered average of LFP power for fourth to fifteenth flashes. V3 shows prominent transients at the onset of each flash, with additional structure just before and after flash offset. Surprisingly, PCC also shows single-flash responses. The initial transients to the first flash (which are not included in this average; nor the second or third flashes) are comparable in size to the V3 transients, but the later responses are ~10 times smaller.

Figure 5
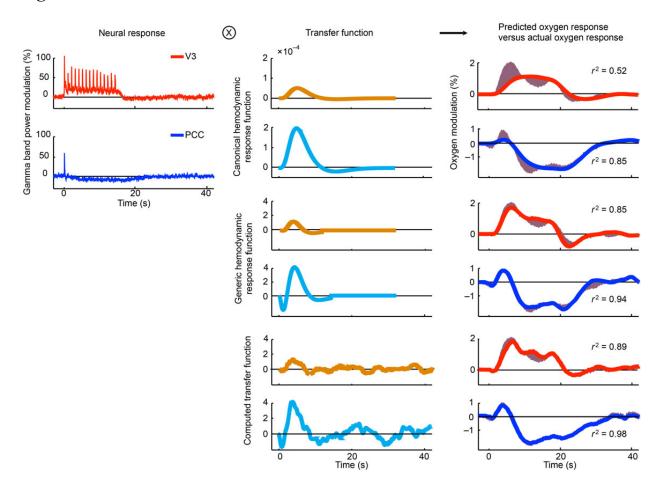
Figure 5. Hemodynamic coupling in V3 and PCC.

First column: Gamma band LFP power in V3 (red) and PCC (blue). Second column: candidate transfer functions used to predict the oxygen response (third column) based on the LFP response (first column). The units of measure are percent oxygen modulation divided by percent LFP power modulation. Third column: predicted and actual oxygen responses. The predicted response is the convolution of the neural response (first column) with the selected transfer function (second column). Shading highlights any mismatch between the predicted and actual oxygen responses. Rows 1+2: A single parameter canonical hemodynamic response function (canonical HRF; see text), fit to either the V3 (orange in the second column) or PCC data (cyan

48

in the second column), is much smaller in V3 than PCC. Only 53% of the variance in the V3

oxygen signal can be predicted, and the initial transients are missed in both areas. Note that the

scale parameter for the function is 3.5 times larger in PCC than V3 (as seen in the height of the

orange versus cyan curves in column 2). Rows 3+4: The best-fitting eight-parameter generic

HRFs (see text) do well but have different shapes in the two areas. The fit for V3 (orange in the

second column) has much smaller amplitude while the fit for PCC (cyan in the second column)

contains an initial negativity that is not present in V3. Rows 5+6: A computed transfer function

(see text) does well in both areas but, like the eight parameter fits, is smaller in V3 (orange in the

second column) and contains an initial negativity only in PCC (cyan in the second column).

Figure 6
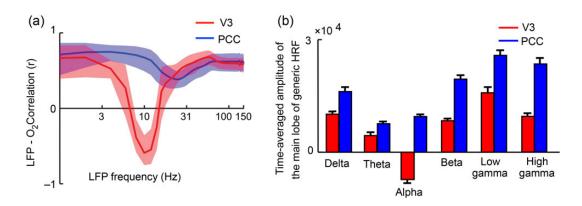
Figure 6. A. A linear correlation (mean± SEM) between oxygen and LFP responses at each frequency.

Correlations were computed at lags from -5 to +12 s, and the highest correlation at each frequency is shown. B. The amplitude (mean± SEM) of the main lobe of generic HRFs in V3 and PCC at each of six frequency bands. Generic HRF was calculated for each data session, and the main lobe was defined as the lobe with the larger deviation from baseline. For all six bands, the amplitude of the main lobe of generic HRFs are significantly different in the two areas.

Supplementary Text

Given a single input and a single output, a linear transform relating the two can always be found (Press WHT, Saul A. Vetterling, William T. and Flannery, Brain P. 2007). With two sets of two inputs and two outputs, one can also always find a linear solution (proof to follow). For example, we might have both Gamma LFP power (input 1) and Alpha LFP power (input 2) from area V3 and from area PCC, and wish to find a set of linear transfer functions (TF1 and TF2) that relate these two inputs to the BOLD signals in each area (Output.a and Output.b). We can express this mathematically as follows:

$$\text{Input1.a} * \text{TF1} + \text{Input2.a} * \text{TF2} = \text{Output.a} \qquad (1)$$

$$\text{Input1.b} * \text{TF1} + \text{Input2.b} * \text{TF2} = \text{Output.b} \qquad (2)$$

Here each term is the time frequency representation of either LFP power (inputs) or the BOLD response (outputs). Multiplication in the frequency domain ("*") is the same as convolution in the time domain (125). Solving for the two transfer functions yields:

$$\text{TF1} = \frac{\text{Output.a} * \text{Input1.b} - \text{Output.b} * \text{Input1.a}}{\text{Input2.a} * \text{Input1.b} - \text{Input2.b} * \text{Input1.a}} \qquad (3)$$

$$\text{TF2} = \frac{\text{Output.b} * \text{Input2.a} - \text{Output.a} * \text{Input2.b}}{\text{Input2.a} * \text{Input1.b} - \text{Input2.b} * \text{Input1.a}} \qquad (4)$$

A finite solution exists so long as

$$\text{Input2.a} * \text{Input1.b} \neq \text{Input2.b} * \text{Input1.a}$$

$$\rightarrow \qquad \frac{\text{Input1.a}}{\text{Input1.b}} \neq \frac{\text{Input2.a}}{\text{Input2.b}} \qquad (5)$$

In other words, if the ratio between Alpha and Gamma bands is not the same in V3 as it is in PCC, we are guaranteed to find a set of transfer functions that works for both V3 and PCC.

More generally, we can replace Alpha and Gamma with any other pair of bands (for instance, Delta and Theta bands). Thus, by using two LFP bands, a mathematical solution can be found that will relate the LFP signals to the BOLD recorded in two different areas. However, given that this is guaranteed to work with any pair of LFP signals, it is doubtful that the solution will reflect anything of physiological interest.

Supplementary Figures

Figure S1

Figure S1. Examples of visual stimuli used in this study.

The projector we used to deliver the stimuli blurred the visual stimuli, to an extent equivalent to applying a 2-pixel radius Gaussian filter to a 259X194 pixel image. Two examples are shown to illustrate the effect of the blurring.

Figure S2

A

10 mm 　　　　　 6 mm

B

11 mm 　　 11 mm 　　 18 mm 　　 19 mm

5 mm 　　 8 mm 　　 13 mm 　　 14 mm
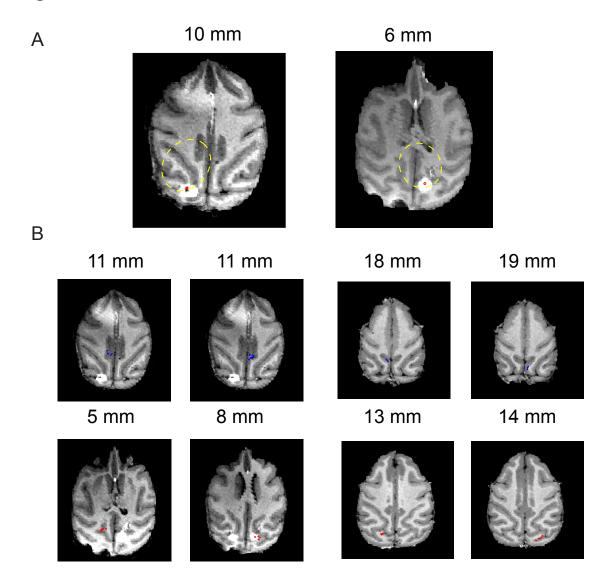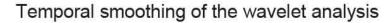
Figure S2. Recording sites confirmed by manganese injections.

Manganese is MRI lucent and was used to calibrate our recording apparatus. A. MRI images

showing injections into each hemisphere (white blobs) and the locations at which injections were

aimed (red dots). The dots are aligned with the injections, confirming the accuracy of our maps.

The dashed yellow ovals mark the boundaries of our recording chambers. B. Recording sites in

the two monkeys (blue dots for PCC, and red dots for V3). Recordings into each hemisphere in

each monkey are shown separately, often at a different slice depth. For example, the upper left panel shows PCC recordings into monkey 1, left hemisphere. The slice depths indicate millimeters above the anterior commissure. The top of the brain is at 22mm and 26mm for Monkey 1 and Monkey 2, respectively.

Figure S3
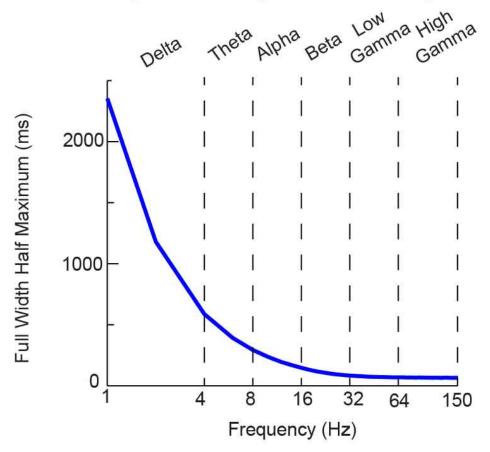
Figure S3. The temporal smoothing of the wavelet analysis.

Power at specific frequency is estimated by convolving data with a complex Morlet wavelet.

This method includes inherent low-pass temporal smoothing. The degree of smoothing is a

function of frequency, and is similar to convolving the instantaneous power with a Gaussian.

Here we show the full width of the equivalent Gaussian at half maximum height for each

frequency. Notice that the degree of smoothing is greater for lower frequencies.

Figure S4
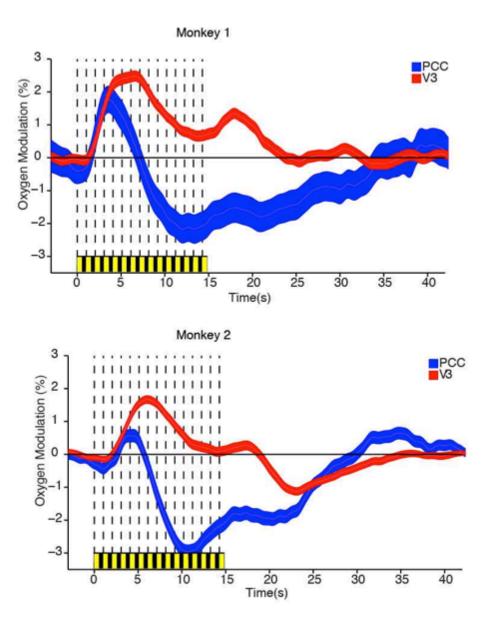
Figure S4. Percent oxygen modulation (mean ± SEM) relative to the period 0-5 s before stimulus onset for both monkeys.

In V3, oxygen level shows a transient response to the stimulus onset, followed by sustain activation. In PCC, oxygen level show transient activation followed by sustained suppression. These are true for both monkeys.

Figure S5
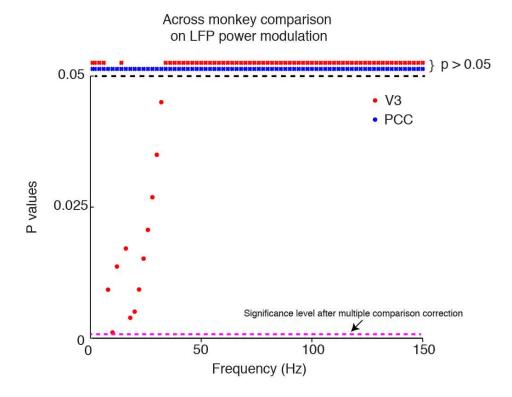
Figure S5. The p values (without multiple comparison correction) for the across monkey

comparison of modulation in LFP power for each frequency.

LFP power modulation is computed the same as in Figure 2B (5-15 s after the onset of visual

stimulation relative to the subsequent 30 s of darkness). P values larger than 0.05 are shown as

crosses. In PCC, there is no significant difference in power between the two monkeys at any

frequency. In V3, there is no significant difference except at 8-32 Hz, where the LFP power

modulation for Monkey 1 is less than that of Monkey 2. Even this difference is not significant if

corrected for multiple comparisons (criterion level of P=.05/76, dashed magenta line).

Figure S6
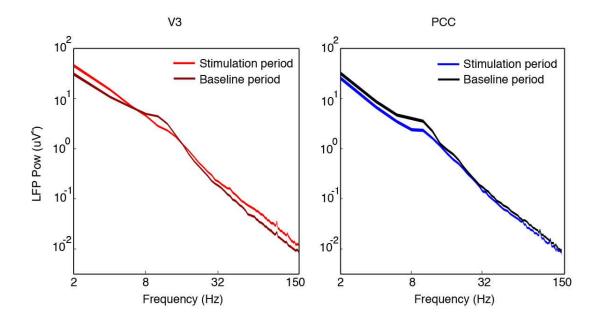
Figure S6. LFP power (mean ± SEM) as a function of frequency (log) during stimulation for V3 and PCC for the visual stimulation period and the baseline period (0-5 s before stimulus onset). Overall, LFP power is inversely proportional to the frequency. In V3, LFP power increases during stimulation compared to the baseline, expect for (6-16 Hz). In PCC, LFP power decreases during stimulation compared to the baseline.

Figure S7
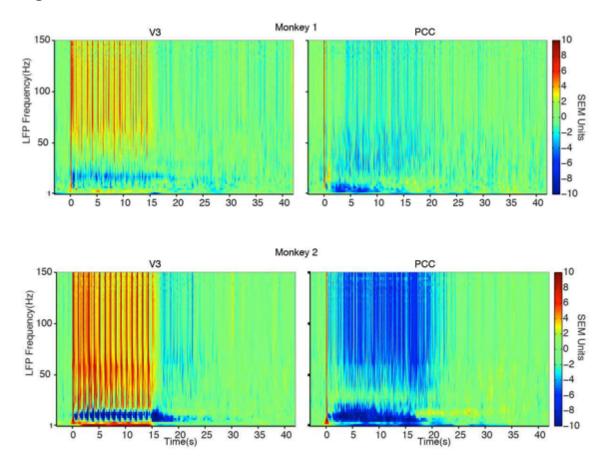
Figure S7. LFP power modulation relative to baseline (0-5 s before stimulus onset) in standard error units (SEM is estimated based on baseline activity) for both monkeys.

Figure S8

A

B
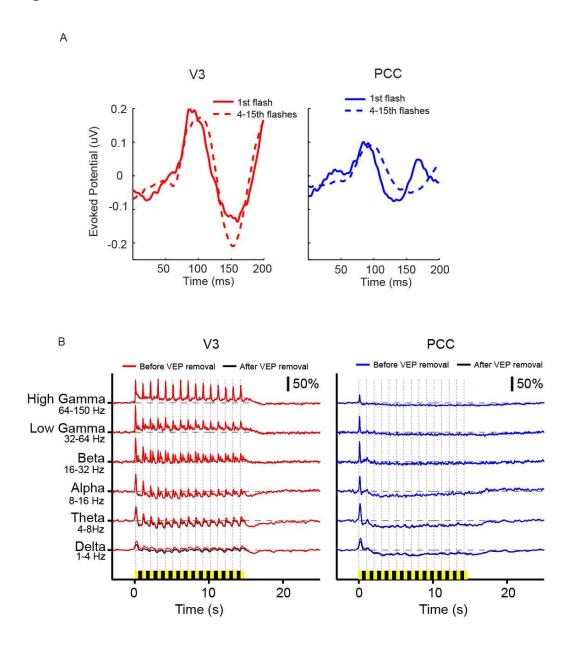
Figure S8. A. Visual stimulus evoked potential (VEP) for V3 and PCC.

The positive component around 100ms could correspond to the P100, and the negative

component around 150ms in V3 could correspond to the N140. VEPs associated with the

stimulus onset (solid lines, first flash) are similar to those evoked by the later flashes (dashed

lines, 4-15th flashes). This is different from oxygen responses, which show a prominent transient

response to the stimulus onset and a sustained response (positive in V3 and negative in PCC) to later flashes. B. Percent modulation of LFP power for standard EEG bands before and after removing VEPs. Removal of VEP slightly decreased LFP responses for both transient and sustained components, but the decrease is so small that the data before (colored) and after (black) VEP removal are almost indistinguishable.

Figure S9
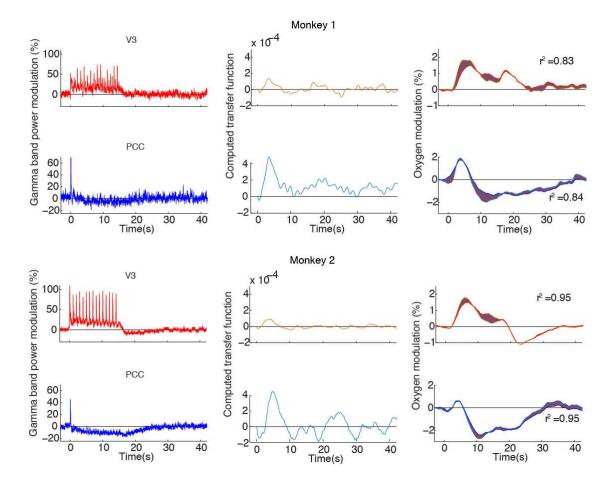
Figure S9. A computed transfer function (see text) does well in both areas but is smaller in V3 (orange in the second column) and contains an initial negativity only in PCC (cyan in the second column) for both monkeys.

Figure S10
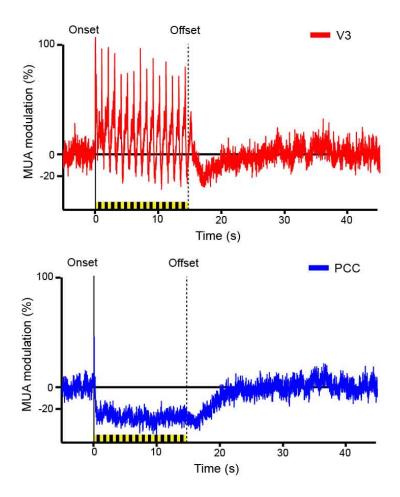
Figure S10. Percent multiple-unit activity (MUA) modulation relative to the period 0-5 s before stimulus onset.

Yellow-black bars mark the 15 s, 1 Hz stroboscopic flashing stimulus. Electro- physiological signals were band-pass filtered (800Hz to 8KHz) and events exceeding 2.5 times the root mean square of the filtered signal were considered as MUA events. V3 shows complex phasic responses riding on top of a tonic increase in MUA activity relative to baseline. PCC shows smaller phasic responses at the onset of the first flash followed by a tonic decrease. Data from 397 trials in V3 and 398 in PCC from one monkey are included.

Chapter 3: Functional connectivity arises from a slow rhythmic mechanism

Abstract

The mechanism underlying temporal correlations among blood oxygen level dependent signals is unclear. We used oxygen polarography to better characterize oxygen fluctuations and their correlation and to gain insight into the driving mechanism. The power spectrum of local oxygen fluctuations is inversely proportional to frequency raised to a power (1/f), with an additional positive band-limited component at 0.06 Hz. In contrast, the power of the correlated oxygen signal is band-limited from ~0.01 to 0.4 Hz with a peak at 0.06 Hz. These results suggest that there is a band-limited mechanism(s) driving interregional oxygen correlation that is distinct from the mechanism(s) driving local (1/f) oxygen fluctuations. Candidates for driving interregional oxygen correlation include rhythmic or pseudo-oscillatory mechanisms.

Significance Statement

Functional connectivity MRI has revolutionized our understanding of brain architecture. Correlated changes in oxygen levels reveal networks of regions. These networks, each linked to particular functions, are conserved across individuals and species. Normal development, learning, and mental disorders are associated with subtle network changes, providing insight into how brains work. Remarkably, the basis of functional connectivity remains unknown. Although some studies have reported data consistent with an oscillatory process, the leading hypothesis involves emergent, arrhythmic dynamics of complex and distributed networks (the "criticality" hypothesis). By using a new electrode-based technique, we show that functional connectivity is not related to criticality, but instead to specific and localizable oscillatory processes. This finding provides a tool to identify the mechanisms underlying functional connectivity.

Introduction:

Resting-state functional connectivity MRI (rs-fcMRI) analyses provide insight into the functional architecture of the brain. The method is based on slow correlations (e.g., 0.01 - 0.1Hz) in blood oxygen level dependent (BOLD) signal across the brain. The pattern of these slow correlations has been used to trace out functional networks, and to describe how these networks develop, change with experience, vary across individuals and are disturbed in disease (169-176). Slow BOLD fluctuations and their correlations are thought to reflect neuronal processes, yet the underlying mechanisms remain unknown (69, 177). We used a high temporal resolution method, oxygen polarography, to characterize the dynamics of oxygen fluctuations and thereby gain insight into the underlying neuronal mechanisms.

Two types of dynamics commonly observed in the brain may be associated with two distinct types of underlying mechanisms or processes. Dynamics with narrow band-limited power may reflect the influence of specific pacemaker units. For instance, the occipital alpha rhythm, which dominates the EEG during relaxed wakefulness, may originate from an alpha pacemaker unit, which consists of a specialized subset of gap-junction coupled thalamocortical neurons that exhibit intrinsic rhythmic bursting at alpha frequencies (178-180). While much evidence supports this oscillatory model of resting state activity (e.g.(181, 182)), the dominant hypothesis in the field is that correlations arise from neural activity propagating within an anatomically constrained small world network (e.g., (77, 183)). This model predicts scale-free dynamics, also known as 1/f dynamics (77, 184). With 1/f dynamics, event amplitude varies inversely with frequency, so that large events are rare while small events are common. More precisely, power may vary inversely with frequency raised by a (small) exponent: $P \propto 1/f^{\beta}$, with

typical exponents from 0 to 3 (38). 1/f dynamics is a hallmark of a complex dynamic system operating at a critical point, at which the system is balanced between ordered and disordered phases (185-187) although 1/f dynamics may also arise in other non-critical systems (188). The fact that various neural signals, such as local field potentials, show 1/f characteristics has inspired models of the brain as operating at a critical point through a process of self-organization (72-77).

Local BOLD fluctuations have a 1/f power spectrum (189-191). This has led to the suggestion that the slow correlations of resting state connectivity may reflect a critical process (38, 184). This assumes that the dynamics of interregional oxygen correlation match the dynamics of local fluctuations. Indeed, three studies report that BOLD correlations vary inversely with frequency (1/f), much like local oxygen (192-194). However, Achard *et al.* Cordes *et al.* and Sasai *et al.* report instead that oxygen correlation peaks around 0.04-0.06 Hz, with less correlation at lower frequencies – a band-limited pattern that is distinctly different from 1/f ((195-197) see also(198-200)). Finally, other studies report that BOLD correlations reach a plateau at low frequencies, a result that is intermediate between 1/f and band-limited dynamics (201, 202).

We used oxygen polarography to directly measure the spectrum of interregional oxygen correlation. Polarography is an invasive alternative to BOLD fMRI that allows robust recording of local oxygen fluctuations with higher temporal resolution, higher frequency specificity, and broader frequency range than can be achieved with standard fMRI techniques. We measured oxygen fluctuations in the default network (bilateral posterior cingulate, PCC, area 23) and the visual/attention network (bilateral V3) in the awake, resting macaque. Here, we report that correlations between homotopic regions are band-limited rather than 1/f. Further, we show that

the variance of local oxygen fluctuations can be separated into a 1/f component and a band-limited component. Only the band-limited component relates to long-range correlation. This suggests that there is a band-limited mechanism(s) driving interregional oxygen correlation that is distinct from the mechanism(s) driving local (1/f) oxygen fluctuations. The fact that correlation is band-limited is suggestive of a rhythmic or pseudo-oscillatory mechanism.

Results

Polarography captures long-range oxygen correlation

We recorded resting state oxygen level simultaneously from four sites in two monkeys: two sites in the default mode network (left and right posterior cingulate cortex, PCC), and two sites in the visual/attention network (left and right V3). In order to verify electrode placement, we first obtained visually-evoked responses at each of these sites. As previously reported (203), both multiunit firing rate and oxygen level were elevated in V3, and both were suppressed in PCC (Fig.1 A). This confirms that our recording sites are located in two functionally distinct networks: V3 is part of the task-positive, visual/attention network, while PCC is part of the task-negative, default mode network.

After visual stimulation, we recorded 30-60mins of resting state data, where monkeys were left alone and resting in the dark room. Similar to BOLD recorded with fMRI, oxygen level fluctuated slowly, over the course of tens of seconds or longer, changing by up to ~10% of the baseline value (Fig. 1B, upper panel, (204). Unlike BOLD, prominent pulsations (~1% of the baseline value) occurred at just above 1 Hz. In separate experiments we recorded simultaneous

69

EKG to show that these pulsations correspond to heart beats (Supplementary Fig. S1). In conventional BOLD, these pulsations are aliased into lower frequencies due to the low sampling rate of fMRI. With our high temporal resolution, this does not occur. However, modulation of heart rate by respiration rate and other low frequency factors will contaminate measures of interregional oxygen correlation regardless of sampling rate (205). To minimize this contamination, we analyzed correlations only after regressing out the heart rate signal (Fig. 1B, lower panel). See Supplemental Text for additional discussion regarding the comparison between oxygen polarography and BOLD fMRI.

To determine whether long-range correlations in oxygen can be seen using polarography, we first bandpass filtered the oxygen signals into the standard fcMRI frequency range (0.1Hz to 0.01Hz). Fig. 1C shows that polarographic oxygen is correlated across long distances. Correlations are significantly larger within a network (in-network correlation, recorded from sites in opposite hemispheres) than correlations across networks (out-of network correlation) ($p < 0.005$). Both in-network and out-of network correlations are greater than zero ($r_{in} = 0.40 \pm 0.03$, $n_{in} = 31$, $p < 0.0001$; $r_{out} = 0.28 \pm 0.02$, $n_{out} = 62$, $p < 0.0001$).   The positive out-of-network correlation is surprising, since many fcMRI studies find that the visual/attention and default mode networks are anti-correlated with one another, that is, their out-of network correlation is negative (204). Such anti-correlation may or may not be the result of pre-processing steps whose purpose is to remove common signals (206). In fact, it has been shown that the so-called "global signal" is in fact particularly prominent in regions including visual cortex and pericingulate regions (207). To test whether the positive out-of-network correlation that we observed was specific to the particular sites that we used, their physical proximity or to their lying within or close to the occipital lobe, we performed additional control experiments. We recorded from two

70

additional pairs of visual/attention and default mode network sites: the intraparietal sulcus (IPS) and PCC, and the anterior cingulate cortex (ACC) and V3 (Fig. S2). All out-of-network correlations were significantly positive, even for pairs at the most extreme distance (ACC versus V3: $r_{out} = 0.20 \pm 0.03$, $p < 0.001$). Distance may effect the strength of out-of network correlation, though this analysis is confounded by network identity (see Supplemental Fig. S2). Hemispheric location (within versus across hemispheres) did not effect out-of-network correlations ($r_{out [within hemisphere]} = 0.29 \pm 0.05$, $r_{out [across hemisphere]} = 0.26 \pm 0.03$, $p = 0.4$).

Out-of-network correlations could be driven by artifactual signals not related to oxygen level. The yellow bar in Figs. 1C and the yellow dot in Fig. S2 represents the correlation between noise signals recorded from soft tissue or fluid immediately adjacent to the brain. This correlation was very low ($r_{noise} = 0.10 \pm 0.06$, $n_{noise} = 42$, $p = 0.13$), ruling out non-oxygen-related artifacts (e.g., correlated electrical circuit noise and movement artifacts) as sources for the high in- and out-of-network correlations. Taken together, our results demonstrate that oxygen polarography can capture long-range, network dependent oxygen correlation and serve as an MR-independent measure of functional connectivity.

Oxygen correlation is band-limited.

To gain insight into the mechanism(s) driving interregional oxygen correlation, we wished to evaluate the frequency structure of just that portion of the signals that is correlated between regions. Since we cannot precisely isolate the correlated signal, we instead estimated its frequency spectrum by computing correlation as a function of frequency. To accomplish this, we filtered the heart-rate-regressed oxygen signals into half-octave frequency bands from 0.003 to 20 Hz and then computed correlation for each band. Fig. 2A shows that both in- and out-

71

correlations are only present in a band-limited window between 0.01 and 0.4 Hz, with a peak at 0.06 Hz, and not present below 0.01 Hz or between 0.04 and 5 Hz. This frequency structure suggests that the correlated signal is not 1/f but band-limited.

There are several additional features in the data, including a prominent peak at 1 Hz and a shoulder at 0.3 Hz. Both are significantly decreased after regressing out heart rate (Supplemental Fig. S3). Respiration is known to modulate heart rate and BOLD signals, and the respiratory rate in monkeys is close to 0.3 Hz (208). Therefore the features at 1 and 0.3 Hz likely reflect residual effects of heart rate and respiration, respectively. A small peak at 10 Hz appears only for in-network correlations and may reflect a previously undescribed high frequency, network-specific coupling. The yellow trace in Fig. 2A represents the correlation found in the soft tissue outside of the brain and demonstrates that the frequency dependence of correlation is a brain-specific finding and not related to extraneous factors such as noise or filtering in our system.

Correlation captures the instantaneous temporal dependence between two signals. If there is a time lag between two otherwise similar signals, then correlation will underestimate that similarity. Consider two otherwise identical sine waves, one of which is shifted in time by one-quarter cycle. One signal perfectly predicts the other, and therefore there is 100% temporal dependence between the two. However, because of the phase shift, their correlation coefficient is zero. Coherence, unlike correlation, captures temporal dependence even in the face of phase shifts. Unlike correlation, the coherence between two sine waves of the same frequency is always 1, regardless of phase lead or lag. In general, shifting two signals in time will change their correlation but will have no effect on their coherence.

Fig. 2B shows that, like correlation, coherence is also band limited from 0.01 to 0.4 Hz. Other related measures such as synchrony and wavelet amplitude correlation give similar results (Supplemental Fig. S4). The pattern for PCC-PCC and V3-V3 recording sites was found in all animals tested, and a very similar pattern of band-limited correlation was also seen in all out-of-network pairs, including the out-of-network correlations between V3 and PCC, IPS and PCC, and V3 and ACC (Supplementary Fig. S5). We conclude that interregional oxygen signals show band-limited temporal dependence, not 1/f.

Local oxygen has both a 1/f component and a band-limited component.

Previous MRI studies report that the local BOLD power spectrum is 1/f from 0.01 to 0.23 Hz (189). Our polarography data extend this finding to a range of 0.003 to 20 Hz. When plotted on log-log axes, a $1/f^\beta$ relationship appears as a straight line with a slope of β. Fig. 3A reveals a $P \propto 1/f^\beta$ relationship with an exponent of 1.74. Together, Figures 2 and 3A shows that local power is predominantly 1/f while long-range correlation is band-limited. This situation might arise in one of two ways. In one scenario, oxygen fluctuations are driven by at least two distinct mechanisms. One mechanism is entirely local and has 1/f characteristics, that is, it has high power at low frequencies and low power at high frequencies. The other mechanism independently drives fluctuations that are correlated across regions. This mechanism is band-limited, with most of its power concentrated between 0.01 and 0.4 Hz (Fig. 2).

In the second scenario, oxygen fluctuations are driven by sources that have a 1/f spectrum, and fluctuations that are coupled across regions are a band-limited component of this 1/f spectrum. (In neither scenario do we include known non-neural sources of oxygen fluctuations, e.g., heart rate, which is band-limited at around 1 Hz.) The power (or equivalently,

73

the variance) of two independent processes will add together. Therefore we can distinguish between the two scenarios by asking whether the local power is best described as the sum of a 1/f component and a band-limited component (supporting the first scenario), or as purely 1/f (supporting the second scenario).

The data support the first scenario, that is, separate 1/f and band-limited sources. On closer examination, the local power spectrum deviates from a strict $P \propto 1/f^{\beta}$ fit, and the largest deviation occurs over the same range of frequencies at which long-range correlations appear (0.01 to 0.4 Hz). When this frequency range is excluded, the exponent of the best 1/f fit is 1.65. We call the difference between the 1/f fit (dashed dark red) and the observed power (solid dark red) the "deviation power" (black). Fig. 3B shows that the deviation power has the same frequency profile as the interregional oxygen correlation. The match is similar for both in-network correlation ($r = 0.89$, $p < 0.0001$) and out-of-network correlation ($r = 0.78$, $p < 0.0001$), though it is stronger in-network than out-of-network ($p = 0.047$). This relationship between the 1/f fit and the observed power is also significant if, instead of using the mean power averaged across all sessions, the relationship is computed session by session ($r = 0.37 \pm 0.04$, $n = 31$, mean $\pm$ SEM, $p < 0.05$ for in-network, and $r = 0.24 \pm 0.04$, $n = 62$, $p < 0.05$ for out-of network). To summarize, local power deviates from a strict 1/f relationship, and this deviation matches the frequency profile of long-range correlation. Since the power from independent processes will add together, this pattern can be most parsimoniously explained by the idea that at least two independent mechanisms drive oxygen fluctuations. One mechanism is 1/f and local, and the second is band-limited and non-local. (We cannot rule out that the two mechanisms may be partially rather than fully independent.)

As a further test of the two-source model, we asked whether the deviation power co-fluctuates with inter-regional oxygen correlation in time. Briefly, we used a sliding window strategy (2 minutes wide, 10 s increments) to estimate the time courses of (1) the local deviation power and (2) the inter-regional correlation strength. The time courses were estimated over a half-octave band centered at 0.06 Hz. We chose this frequency band because this is where we measure the highest deviation power and the strongest inter-regional correlation. We then calculated the correlation coefficient between the time course of average deviation power from each pair of electrodes, and the time course of the long-range correlation coefficient between those same two electrodes. The fluctuations of local deviation power are significantly correlated with the fluctuations in long-range correlation, both for in-network ($r = 0.29 \pm 0.05$, $p < 0.05$) and out-of network electrode pairs ($r = 0.13 \pm 0.04$, $p < 0.05$). The relationship is significantly stronger in-network compared to out-of-network ($p = 0.03$). These results confirm that local deviation power is significantly related to long-range correlation. The relationship exists for both in-network pairs and out-of network pairs, but is stronger for in-network pairs.

As a final test of the two-source model, we evaluated the impact of removing correlated power on the local power spectrum. If the two-source model is accurate, then removing the power associated with the long-range correlation (the correlated power) from the locally measured power should make the remaining power more consistent with the $P \propto 1/f^\beta$ spectrum (Fig 4A). We estimated the correlated power based on a linear regression model (see Experimental Procedures). Removing the correlated power significantly improved the fit of the local oxygen signals to a $1/f^\beta$ model. For each individual session and recording site (n=93), removing the correlated power either reduces the maximum deviation from a strict $P \propto 1/f^\beta$

spectrum or else leaves it essentially unchanged, that is, all of the data points fall close to or below the diagonal identity line. In no case did removal of the correlated power substantially increase the deviation from a 1/f fit, that is, no points are well above the identity line. In summary, our data support a two-source model in which oxygen fluctuations are driven by the sum of long-range band-limited sources and a local 1/f source. The removal of the correlated power from a single distal electrode does not produce a perfectly linear fit, that is, after removal a positive deviation often remains in the 0.01 to 0.4 Hz range (e.g., the right panel of Fig. 4A). This is consistent with a model in which there are independent band-limited contributions from multiple long-range networks, and our manipulation removes only one of those contributions.

Differences in frequency content across networks.

To investigate whether the frequency content of correlation is similar or different for different networks, we compared correlation and power deviation across frequencies in the visual/attention network (left V3 and right V3) and in the default mode network (left PCC and right PCC). Fig. 5 shows that the frequency profiles of the visual/attention and default networks are broadly similar, whether assessed by oxygen correlation (Fig. 6A) or by power deviation (Fig. 6B). Both networks are band-limited from 0.01 to 0.4 Hz.

To compare band-limited correlations in the two networks more closely, we compared the frequencies at which the peak effect (correlation or deviation power) occurs, computed electrode pair by electrode pair. There is no significant difference in the values obtained using one or the other method ($P_{visual/attention} = 0.7$, $P_{default} = 0.6$). The peak correlation frequencies (Fig. 6A, arrows) show a trend towards being higher in the default network than in the visual/attention network (0.072 ± 0.009 versus 0.056 ± 0.004 Hz, respectively; $p = 0.09$). This difference is

significant for the peak deviation power (Fig. 6B, 0.054 ± 0.004 Hz versus 0.076 ± 0.005 Hz, $p < 0.05$). In sum, correlation within the two networks occurs at a similar range of frequencies (0.01 to 0.4 Hz), but the peak effect is 0.02 Hz higher in the default network compared to the visual/attention network. Finally, the fact that the same peak frequencies are seen within each network when using either long-range correlation or local deviation power further supports the two-source model.

Eyes open versus eyes closed

Both local fluctuations and long-range correlations were stronger when the eyes were closed compared to open. Effects were similar across areas and networks, with greater effects in-network compared to out-of-network (Supplemental Text). The published data from human fMRI are remarkably inconsistent on this point (Supplemental Table S1). See Supplemental Text for discussion.

Discussion:

Inter-regional correlation of fluctuations in the blood oxygen level dependent (BOLD) signals has been used to reveal the functional architecture of large-scale brain networks. To gain insight into the origin of BOLD correlation, we used a high temporal-resolution measurement, oxygen polarography, to further probe oxygen fluctuations and their correlation. We simultaneously recorded oxygen from two sites in the default mode network (bilateral posterior cingulate) and from two sites in the visual/attention network (bilateral V3) in each of two resting macaques across multiple experimental sessions.

We found that long-range oxygen correlation occurs only in a restricted frequency window of 0.01 to 0.4 Hz (Fig. 2; see Supplemental Text for discussion regarding the upper bound). In contrast, the variance or power of local oxygen levels is inversely proportional to frequency (1/f, or more completely, $P \propto 1/f^{\beta}$ with $\beta = 1.7$) across the full range of tested frequencies (0.001-20 Hz) (Fig. 3A). This indicates that the (band-limited) process(es) driving interregional correlation are distinct from the (1/f) process(es) driving local oxygen fluctuations. On closer inspection, the power spectrum of local oxygen fluctuations deviates slightly from a strict $1/f^{\beta}$ fit. The profile of this deviation closely matches the frequency profile of the long-range oxygen correlation (Fig. 3B). This is exactly what would be predicted if the band-limited mechanism(s) driving inter-regional oxygen correlation are independent of the mechanism(s) driving the local $1/f^{\beta}$ fluctuations. Finally, the fact that correlation is band limited suggests that long-range oxygen correlations are driven by a rhythmic or pseudo-oscillatory mechanism. The fact that the peak frequency is higher in one network than the other (Fig. 5) is consistent with two separate driving mechanisms, but could also arise from a single mechanism with slightly different effects on the two networks (201).

Oxygen polarography captures interregional oxygen correlation.

Functional connectivity MRI (fcMRI) has established that blood oxygen levels in widely separated brain areas fluctuate in synchrony. This finding was established by sampling volumes 2-3 mm on a side at 1-3 s intervals. We modified an existing technique, oxygen polarography, to examine long-range oxygen correlations. Oxygen polarography has been used to study the vascular control of oxygen levels in the brain and more recently to examine the relationship between local oxygen levels and neuronal activity (118, 166, 203, 209, 210). Fluctuations in local oxygen level were an incidental finding in many early polarography studies, but they were

78

believed to be driven by local autoregulation (e.g. (211, 212)). Burgess and Shallet have observed slow fluctuations (~0.1Hz) that are correlated between left and right medial geniculate in rats (Abstract, D. Burgess et al., Stroke, 374, 1973). However, the importance of interregional oxygen correlation did not become apparent until fcMRI revealed that long-range BOLD correlations can be used to delineate functionally relevant brain networks (6, 204).

Polarographic oxygen signals can be recorded using modified glass pipettes (Clarke electrodes), platinum or carbon paste electrodes (118, 166, 209, 210). Electrode tip sizes can range from microns to millimeters. We recorded simultaneously from multiple areas using independently controlled platinum microelectrodes with ~30 micron exposed tips. Our design was optimized for robustness (required for use in an awake behaving animal), high spatial specificity and high temporal resolution. In our design, oxygen levels are recorded from a sphere of brain parenchyma 30-100 microns in diameter (volume = 0.00001-0.0005 cubic millimeters). We temporally filtered the analog oxygen signal at 20 Hz prior to digitizing at 1000 Hz.

Remarkably, the signals obtained through fMRI and polarography are largely similar, despite differences in sampled volume and temporal resolution, and despite the fact that polarography samples tissue oxygen rather than blood oxygen. The amplitude and time course of stimulus-evoked responses in both task positive and task negative areas are similar for the two techniques (203), as is the finding of interregional correlations (Fig. 1). In our data, exactly as in fcMRI prior to global signal regression (see below), most correlations are positive. Scholvinck and colleagues have found electrophysiological evidence for widely shared neural activity at rest in non-human primates, which could correspond to the positive correlation that we see in the polarographic oxygen signals between PCC and V3 (213).

A direct comparison between the functional connectivity revealed by polarography and fcMRI is complicated by differences in preprocessing. Before computing correlations in fcMRI data, a mean signal (the global signal) is computed and then regressed out of each voxel's data. Some portion of the global signal is clearly artifactual, including variance due to head movements, respiration, and aliasing from heart rate. Some variance is of neural origin. The neurally-derived portion of the global signal could reflect a specific global neural signal, as shown in *Scholvinck et al.*, or merely an average of neural activity throughout the brain (206, 213). Global signal regression (GSR) will distort correlation by imposing a substantial negative bias, since the sum of the correlations across all the contributing signals must necessarily be less than or equal to zero as a result of GSR (Supplementary Fig. S6, see (206) for proof). In addition, GSR might fundamentally alter the correlation pattern by biasing correlations differently in different regions depending on the true underlying correlation structure (214). Nevertheless, GSR remains in wide use for fcMRI data, and this is fully justified by the fact that GSR is effective in removing artifactual variance in fcMRI data and greatly improves the delineation of networks within the brain (215).

While GSR is appropriate for fcMRI preprocessing, it would be inappropriate to apply GSR to our polarographic data. Artifactual sources are greatly attenuated in polarographic compared to MRI data. Sampling rates are higher so aliasing of heart and respiration rate is not an issue; heart and respiration rate effect can be resolved and removed from the data. In addition, we did not observe shared signals in our control recordings from non-neural tissue (Fig. 1B). This result argues that our system is not susceptible to correlations resulting from non-neural sources, including motion artifacts, which is the major artifactual source in fcMRI data. Thus, applying GSR to polarography data will not yield empirical benefits in artifact removal as

80

in fcMRI. If we were to nonetheless blindly apply GSR in the current study, then the sum of all of our correlations would necessarily be negative. This would occur whether or not a shared signal is actually present; it is a mathematical consequence of the operation and independent of the physiology. With thousands of signals, as in typical fMRI analyses, the sum of the correlations after regression approaches zero; with fewer signals the sum is progressively more negative (Supplementary Fig. S6). Thus, with our current state of knowledge, applying GSR to our data is inappropriate for both theoretical and practical reasons. We cannot rule out the possibility that our results may be affected by the inclusion of a globally shared neural signal that is removed from the fMRI data by GSR. However, our most important finding – that interregional correlation is band-limited – still applies, since the difference between in-network and out-of-network correlation is itself strongly band-limited (Fig. 2A).

Interregional oxygen correlation is independent of local fluctuations and is band-limited.

The temporal and spatial features of interregional oxygen correlation can provide clues to the origin of the correlation. Local BOLD fluctuations have 1/f power spectra (Fig. 3A; (189-191). From this it has been suggested that neural activity corresponding to interregional BOLD correlation may also have a 1/f power spectrum (38). Furthermore, the topology of connectivity, as assessed by correlations, itself shows a 1/f character. Only a few voxels are strongly correlated with many other voxels outside of their own network ("hub nodes"), while many voxels show a few inter-network correlations (78, 79). 1/f features are a signature of a system operating around criticality, a state where the system balances between ordered and disordered phases and has a maximum number of metastable states (216). Taken together, these findings

81

have inspired a heuristic model in which interregional oxygen correlation results from self-organized criticality (72-76).

A key assumption of the heuristic model is that the spectrum of interregional correlation is 1/f. While some studies have obtained results consistent with a 1/f pattern, other studies report opposite results. Salvador et al. separate BOLD into three frequency bands (0-0.08Hz, 0.08-0.17Hz and 0.17-0.25Hz) and show that correlation is strongest at the lowest frequency band, consistent with a 1/f spectrum (193). Ciuciu et al. also argue that BOLD coherence is 1/ f (192). In contrast, Wu et al. show that correlation first increases as frequency decreases and then plateaus at 0.04-0.06Hz (201). Achard et al. show that wavelet correlation, which is similar to coherence, peaks around 0.03-0.06Hz and drops at lower frequencies (196). Sasai et al. measure mean-squared coherence and find that the prefrontal and occipital regions show high coherence only in a narrow frequency range (0.04– 0.1 Hz) (195). Network structure is most clear for fMRI at 0.02-0.06 Hz (33, 36, 37). Additional indirect support of band-pass behavior can be seen in studies of quasi-periodic patterns in the BOLD signal, which have a center frequency of around 0.05 Hz (217-220). Other indirect support can be found in the fact that gamma-band power, a putative neural correlate of BOLD (but see (203)), is coherent within the default mode network only over a narrow frequency range (191). Still other studies find mixed results regarding the frequency content of BOLD correlation (197, 202). Thus, some results have been consistent with a 1/f pattern and others have been consistent with a band-limited pattern.

Two main issues may explain the lack of agreement across studies. In order to distinguish band-limited from 1/f effects, a wide range of frequencies is helpful. Many studies of correlation acquire only 5-10 minutes of data, which limits their range at the low frequency end. Range is limited at the high end by sampling rate. A typical 5 minute fMRI dataset provides a

theoretical frequency range of 1.3 decades (0.17 to 0.0033 Hz), and a usable range of less than

one decade. (The usable range is reduced at the high end because the Nyquist limit cannot be

reached under real-world conditions, and is reduced at the low end because at least three or four

cycles are required for a reproducible estimate.) Second, most measures of coherence (but not

mean-squared coherence, used by (195) are compromised by a mathematical artifact that

produces an apparent 1/f effect (Supplemental Fig. S7). This bias is surprisingly strong, yet few

studies remove or otherwise compensate for it (192, 195). In addition, Zhang *et al*. show that

artifacts, such as head motion and systemic physiological fluctuations in pulsation, can mask the

frequency structure of the 'true' correlation (200). To address these issues, we use oxygen

polarography, which is less susceptible to artifactual correlations (Fig. 1B and 2A), and collect

polarographic data for 40 minutes, providing at least 4 cycles of data over four frequency

decades (0.0017 Hz to 20 Hz), and correct our analysis of coherence for the artifactual 1/f

contamination.

We show that interregional oxygen correlation is band-limited from 0.01 to 0.4 Hz with a

peak at 0.06 Hz, not 1/f (Fig. 2). In addition, we show that the power spectrum of oxygen

fluctuations measured at each electrode can be explained as the sum of a 1/f process plus a band-

limited process (Fig. 3A). Both the frequency profile and the temporal fluctuations of the

deviation power match those of the interregional correlation (Fig. 3B). This relationship exists

for both in-network pairs and out-of network pairs, but is stronger for in-network pairs. Our

results indicate that the signal underlying interregional correlation has a band-limited spectrum

that is distinct from the 1/f pattern of local oxygen fluctuations. The fact that the relationship is

stronger for in-network pairs supports that the deviation power reflects both network-specific and

network-nonspecific correlations (such as the global signal shown in (213)). In-network pairs

capture both network-specific and network-nonspecific correlations, while out-of network pairs only capture network-nonspecific correlation, and thus, in-network pairs show a stronger relationship between their correlation and their local deviation power.

Our results do not address whether criticality exists in the brain. They do, however, strongly suggest that interregional correlation is neither a result nor a reflection of criticality. More generally, our results challenge the view that functional connectivity arises from neural activity propagating within an anatomically constrained network (e.g.(77, 183)). This would predict that correlation has a flat spectrum (Supplemental Fig S8). Instead, we show that oxygen correlation is band-limited. The band-limited aspect of interregional correlation is highly suggestive of rhythmic or pseudo-oscillatory mechanisms, perhaps reflecting resonant mechanisms or circuits (182, 221-223).

Interregional correlations could be driven by oscillatory modules, perhaps in sub-cortical nuclei, which consist of small sets of cells and generate band-limited patterns of firing that are then transmitted to widespread cortical and sub-cortical regions. Indeed, simple oscillator-based models of functional connectivity exist (e.g.(80)). However, these models focus on oscillators with fast dynamics, on order of tens to hundreds of milliseconds. Our results point to oscillators with dynamics several orders of magnitude slower.

An alternative possibility is that band-limited correlation which we measure using polarography is unrelated to the functional connectivity measured using BOLD and instead reflects local vasomotion or Mayer waves, both of which are low frequency (~0.1 Hz) oscillations in cerebral hemodynamics. For several reasons, we do not believe this is the case. First, we see greater correlation within known cortical networks than across networks. Local

vasomotion is a spontaneous oscillation of local blood vessel tone and is unlikely to drive long-range correlations (211, 224) but see (217). Mayer waves are produced by oscillations of arterial pressure and can drive long-range correlations, but these correlations would not reflect functional network structure (225). Second, our control recordings from soft tissue should be as susceptible to local vasomotion and Mayer waves as signals recorded from the brain (226). Yet our control recordings do not show band-limited correlation. Third, local vasomotion sporadically occurs in a range of pathological conditions or subjects underlying anesthesia but appears to be rare in healthy awake subjects; its occurrence may reflect a form of hemodynamic dysregulation (224). In contrast, fcMRI is a consistent phenomenon, seen in essentially all subjects. We have found band-limited oxygen correlations in all four awake, resting monkeys that we tested (Supplementary Fig. S5). The odds of all four animals showing the same rare vascular behavior are quite low. Fourth, the characteristic frequency of local vasomotion and Mayer waves is 0.1 Hz, which is almost an octave above the center frequency that we observe. Fifth, local vasomotion and Mayer waves are sinusoidal, with a large amount of power in a very narrow frequency range (211, 224, 225). The signals we have recorded are not sinusoidal but aperiodic (Fig. 1A). In sum, though we cannot rule out that local vasomotion or Mayer waves contributes to oxygen correlation, these facts all suggest that the band-limited correlation that we observe reflects the same phenomenon that is revealed by resting state fcMRI in humans and is of neural origin.

Materials and Methods:

Animals, Behavior, Stimulus: Two macaques served as subjects in this study. Animals were cared for and handled in accordance with the Guide for the Care and Use of Laboratory Animals, and all procedures were approved by the Washington University Animal Studies Committee. During recording, macaques were fully hydrated and sat head-fixed in a dark room. Behavior was unconstrained, and the animals had no expectation of a task or reward. Animals naturally relaxed in the setup. The velocity of spontaneous eye movements typically slowed and the eyelids often partially or fully closed (64% and 17% of the time, respectively for the two monkeys). Results discussed below are similar for the two monkeys, and thus the data are combined.

Recording: Electrodes were targeted to V3 and PCC using anatomical MRI images and physiology (203). Briefly, each animal's brain was accessed via bilateral 15 mm (internal diameter) chronic custom recording chambers. T1 weighted MRI images (MPRAGE; .5 mm isotropic voxels) were obtained using a custom phantom in the chamber that provides visualization of the chamber and allows for the virtual projection of a chamber-based coordinate system down into the brain. In one monkey, two small manganese injections were placed to confirm alignment. Prior to data collection, boundaries for PCC and V3 recording regions were defined on the MRI image. The positions of PCC and V3 were further validated based on their respective oxygen and electrophysiological responses to visual stimulation, which were recorded immediately before the resting state data (203).

To record oxygen signals, we utilized specialized platinum microelectrodes (FHC Inc. Inventory #: UE(LS3)) as a cathode. An Ag/AgCl reference electrode (Grass Technologies) was placed on the back of the head at a location with minimal underlying musculature and no response to body or limb movements. The skin was lightly abraded to minimize sweat and movement potentials, and a layer of Ten20 EEG paste was applied. The platinum cathode was polarized at -0.8 volts relative to the reference electrode (Unisense PA2000). The current required to maintain the polarization is proportional to oxygen level. This signal was filtered at 20 Hz and sampled and stored at 1 kHz using the Plexon MAP system (Plexon Inc.).

We recorded oxygen signals simultaneously from left and right PCC and left and right V3. Twenty data sets (10 from each monkey) with an average length of 40 minutes were recorded.

Analysis: All analyses were performed with custom software written in Matlab (MathWorks). Oxygen polarographic signals, like BOLD signals, reflect relative rather than absolute oxygen levels. Therefore the polarographic signals, like BOLD data, were expressed as percentage deviation from the mean signal level.

Heart rate removal. We identified individual heart rate pulsations using a recursive template-matching approach. We started with a 1-second Gaussian-derived generic heart beat template. We identified putative beat times as the moments at which the template had greatest linear correlation with the data using a sliding window approach (1s window with increment of 1ms). We used these times to generate a beat triggered average of the oxygen signal. We then replaced the heart beat template with this beat-triggered average and repeated the analysis. Four iterations were performed in order to refine our estimates of the beat template and the beat times.

87

The estimated heart beat effect was then regressed out of the oxygen signals, taking into account instantaneous heart rate, using the method of Fekete et al. (227).

Band-pass filtering. Band-pass filtering was accomplished by first high-pass filtering and then low-pass filtering. Chebyshev-type II filters were designed with a defined passband and stopband. The transition band of each filter was one octave wide, and the stopband was set to -80 dB. For the correlation in Fig. 1B, the -3 dB points for the low and high pass filters were set to 0.01 and 0.1Hz, respectively. For correlation in Fig. 2A, oxygen signals were filtered into individual frequency bands using filters with half octave passbands.

Correlation and coherence. Correlation was calculated as Pearson's r. To calculate coherence, we decomposed each oxygen signal into a time-frequency representation. We extracted the instantaneous amplitude *A(t,f)* and analytical phase *ψ(t,f)* as a function of time and frequency by applying the Hilbert transform to each half-octave band. To confirm that our results were not influenced by the specific filters used or by the use of the Hilbert transform, we repeated the decomposition and subsequent analyses using a continuous wavelet transform with a complex morlet wavelet (203). These two approaches generated nearly identical results.

Coherence at the frequency (f) is defined as,

$$Coherence_{x,y}(f) = \left| \frac{\mathbb{E}\{A_x(t,f) * A_y(t,f)e^{i[\psi_x(t,f) - \psi_y(t,f)]}\}}{\sqrt{\mathbb{E}\{A_x(t,f)^2\}} * \sqrt{\mathbb{E}\{A_y(t,f)^2\}}} \right|,$$

where $\mathbb{E}$ is the expectation or mean value across time (t). Coherence measures the degree of consistency of the phase difference $\Phi_{x,y}(t,f) = \psi_x(t,f) - \psi_y(t,f)$ across time. It ranges over the interval 0 to 1. The more consistent the phase difference across time, the higher the coherence

value. All statistics on correlation and coherence were done after applying Fisher's Z transform (228).

Estimations of instantaneous phase at neighboring time points by a Hilbert or wavelet transform are based on a finite interval. This results in the phase of neighboring time points being nearly identical, because they are estimated based on overlapping data. Even phase estimates of time points that are more widely separated will show some level of artifactual consistency. This artifactual consistency in phase within individual signals produces artifactual consistency in the phase *differences* across signals. This in turn leads to artifactual non-zero values for coherence even for completely independent signals. Supplementary Fig. S7 shows that the bias between two 8-minute independent synthetic signal streams. The bias approaches 1 for a single cycle of data. This reflects the fact that, with a single cycle of data, phase can hardly vary as a function of time, and therefore the phase difference between two independent streams remains nearly constant for the entire cycle, and coherence thus approaches one. As the number of data cycles in each stream increases, the bias decreases, but even with 1000 cycles of data (corresponding to a frequency of just over 1 Hz for an 8 minute data stream) the bias is still significantly greater than zero. The result is that, for most data lengths, there will be a substantial bias towards a 1/f characteristic.

To estimate and remove the bias, we constructed two independent synthetic signals, each with the same duration and power spectrum as the recorded oxygen signals. We then calculated their coherence. This process was repeated 100 times and the resultant values were averaged to compute the mean expected bias. For the analysis illustrated in Fig. 2B, the mean expected bias was subtracted out so that a value of zero corresponds to the consistency of phase differences that would be obtained by chance were the null hypothesis true (no coherence).

89

Power spectrum and deviation power. The power spectrum was obtained using the

multitaper technique (229, 230), which efficiently improves spectral estimates by using multiple

Slepian tapers. When power and frequency are expressed in log units, the 1/f power spectrum is

captured by a linear function,

$$log(Power) = \beta * log(f) + k,$$

where f is frequency, β is the power exponent and k is the offset. The deviation power (Fig. 3)

was calculated as the difference between the actual power and the power predicted by a linear fit.

Removal of correlated power. We wished to estimate power in a signal after removing

the power that is associated with a correlated signal. Consider two signals, expressed as vectors

$\vec{X}$ and $\vec{Y}$, whose correlation coefficient is r. Both $\vec{X}$ and $\vec{Y}$ can be written as the sum of a shared

component plus a unique component.

$$\vec{X} = \left(\vec{S} * W_{Sx} + \overrightarrow{U_x} * \sqrt{1 - W_{Sx}^2} \right) * |\vec{X}|, \qquad (1)$$

$$\vec{Y} = \left(\vec{S} * W_{Sy} + \overrightarrow{U_y} * \sqrt{1 - W_{Sy}^2} \right) * |\vec{Y}|, \qquad (2)$$

where $\vec{S}$, $\overrightarrow{U_x}$, and $\overrightarrow{U_y}$ are unit-length vectors corresponding respectively to the shared component,

the unique component in $\vec{X}$ and the unique component in $\vec{Y}$. $\vec{S}$ and $\overrightarrow{U_x}$, $\vec{S}$ and $\overrightarrow{U_y}$, and $\overrightarrow{U_x}$ and $\overrightarrow{U_y}$

are all orthogonal to each other. W_{Sx} and W_{Sy} are the relative weights of the shared component

($\vec{S}$) in $\vec{X}$ and $\vec{Y}$, respectively. If the fraction of the total signal that is shared is similar in $\vec{X}$ and $\vec{Y}$,

then $W_{Sx} = W_{Sy} = W_S$, and based on (1) and (2) the shared power and the unique power are

expressed as:

90

$$Shared\ Power\ = Total\ Power * \left(W_S{}^2\right), \tag{3}$$

$$Unique\ Power = Total\ Power * \left(1 - W_S{}^2\right). \tag{4}$$

The correlation between $\vec{X}$ and $\vec{Y}$ is by definition:

$$r = \frac{\vec{X} * \vec{Y}}{(|\vec{X}| * |\vec{Y}|)}. \tag{5}$$

We can substitute the values from equations (1) and (2) into (5). Because $\vec{S}$, $\overrightarrow{U_x}$ and $\overrightarrow{U_y}$ are all orthogonal to each other, most of the terms in the dot product go to zero, leaving

$$r = \frac{\vec{S} * W_{Sx} * |\vec{X}| * \vec{S} * W_{Sy} * |\vec{Y}|}{(|\vec{X}| * |\vec{Y}|)} = W_{Sx} * W_{Sy} = W_S{}^2. \tag{6}$$

Therefore, from equations (3), (4) and (6):

$$Shared\ Power\ = Total\ Power * r,$$

$$Unique\ Power = Total\ Power * (1 - r).$$

Thus, the unique power in a signal that is leftover after removing the power that is associated with a correlated signal is simply, for each frequency band, the total power times one minus the Pearson correlation.

Acknowledgments

Figures

Figure 1

A   Stimulus-driven activity

B   Resting state activity

C
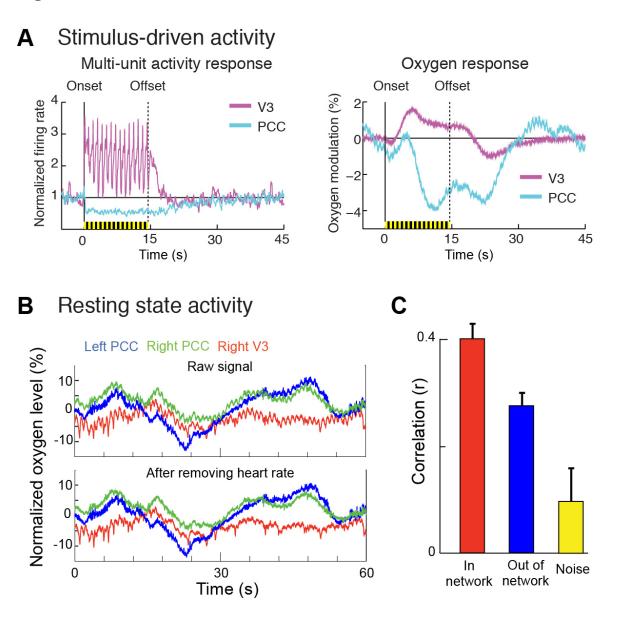
Fig. 1. Visually driven response and at-rest oxygen correlation.

A) Visually driven activity in V3 and PCC. The visual stimulus is a 1 Hz flash for 15 s (yellow

and black bar). The left panel shows firing rate normalized to the rate in the 5 s before

stimulation and the right panel shows the oxygen modulation. In V3, both unit activity and

oxygen level are activated during visual stimulation, and in PCC, both are suppressed. **B)** Example data (normalized oxygen level) obtained from three electrodes in a minimally-restrained animal at rest in complete darkness. Lower panel is the same data after regressing out heart rate. **C)** Within each network, oxygen signals (left versus right V3, left versus right PCC) are strongly correlated with one another ("In network", r=0.40 ± 0.03, n=31 polarographic electrode pairs). Out-of-network signals (left V3 versus left PCC, left V3 versus right PCC, right V3 versus right PCC, right V3 versus left PCC) are also correlated, but less so (r=0.28 ± 0.02, n=62 electrode pairs). The correlation between noise signals, recorded from outside the brain, is 0.10 ± 0.06 (p = 0.13, n = 42). Both in-network and out-of-network correlations are significantly higher than noise correlation (both $p < 0.005$), and the difference between in-network correlation and out-of-network correlation is significant ($p < 0.005$).

Figure 2
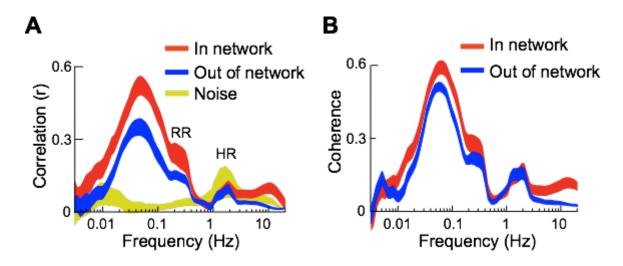
Fig. 2. Oxygen correlation and coherence.

A) Oxygen correlation as a function of frequency, mean ± 1 SEM. Both in- and out-of-network

correlations are band-limited from 0.01 to 0.4 Hz. Peak correlation is at 0.06 Hz. Data recorded

from outside the brain show no significant correlation at these frequencies. The peak just above

1 Hz and the shoulder just above 0.1 Hz reflect residual effects of heart rate (HR) and respiratory

rate (RR), present after regression of HR (see Supplemental Results). **B**) Coherence (baseline

removed; see Methods and Supplementary Fig. S4) shows band-limited effects similar to those

seen in correlation.

Figure 3
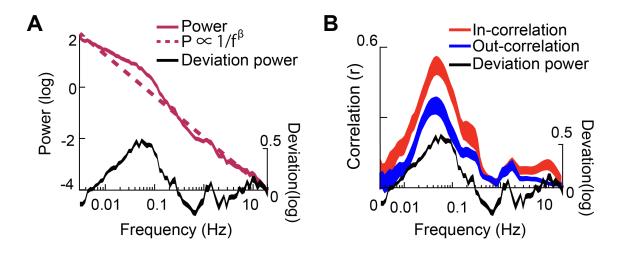
Fig. 3. Oxygen power spectrum.

A) Power in the local oxygen signal as a function of frequency. A log-linear (1/f) model fit (dashed dark red) accounts for most of the power in the raw oxygen (solid dark red). Subtracting the log-linear fit from the observed power leaves a residual that we call the "deviation power" (black). **B**) The frequency profile of the local deviation power is similar to the frequency profile of long-range correlation, both within-network ("in-correlation") and across networks ("out-correlation").

Figure 4
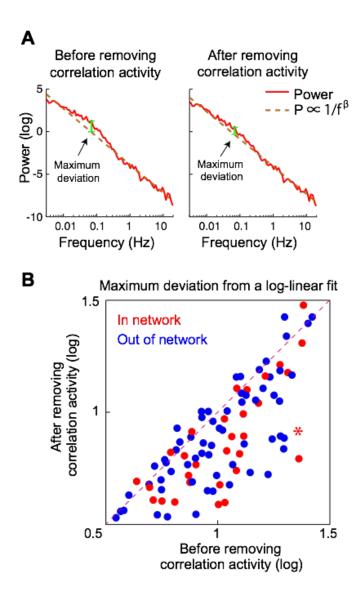
Fig. 4. Maximum deviation from a log-linear fit.

A) The oxygen power spectrum was expressed in log-log scale and then fit by a linear function

(log(Power) = -β*log(f) +k, or $P \propto 1/f^{\beta}$) for before (**left panel**) and after (**right panel**) removing

correlated activity. The maximum deviation was computed as the maximum difference between

the observed power spectrum and the linear fit (vertical black lines). **B**). Maximum deviation

before and after removing correlated activity. Each individual data point corresponds to a single

session's recording from a single pair of in-network (red dots) or out-of-network oxygen signals (blue dots). The maximum deviation was reduced or largely unchanged as a result of removing the correlated portion of the signal. The asterisk corresponds to the data in **A**.

Figure 5
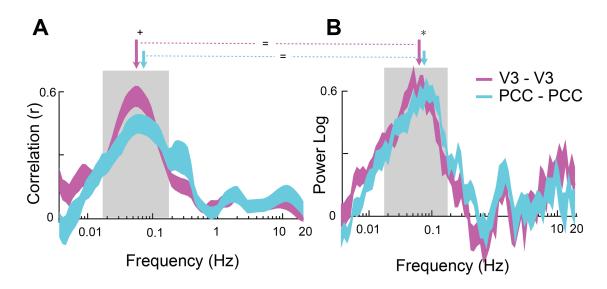
Fig. 5. The frequency profile of oxygen correlation and deviation power in the networks.

A) The frequency profiles of oxygen correlations from the visual/attention and default networks are nearly identical. The default network has a trend towards a higher peak correlation frequency than the visual attention network (V3) (0.072 ± 0.009 versus 0.056 ± 0.004 Hz, respectively; $p = 0.09$ for the difference). **B**) The deviation power profiles from the two networks are also similar, although the small difference in the peaks of the deviation power is significant (0.076 ± 0.005 versus 0.054 ± 0.004 Hz, respectively; $p < 0.05$ for the difference). The peak frequencies revealed by correlation analysis (left panel) versus deviation power (right panel) are not significantly different from one another for either network ($p > 0.5$ for each).

Supplemental Text

Eyes-open versus eyes-closed

We compared the amplitude of both (local) low frequency oxygen fluctuations and the strength of long-range correlations in eyes-closed versus eyes-open conditions. Our animals were free to open or close their eyes at any time within each session. This had no effect on retinal stimulation, since the room was completely dark (no light detectable by humans after 15 minutes of dark adaptation). We divided the data into one minute chunks using a sliding-window approach (window length = 1 min, with a 6-s time step between consecutive windows), and sorted into those in which the percentage of eyes-closed time was less than 70% (n=8069), between 30 and 70% (n=5290), or greater than 30%(n=12255). (Total recording time from 4 monkeys together was ~43 hours.) Local fluctuation, quantified by the coefficient of variation, increased from 0.68 to 0.85 to 1.44 as the proportion of eyes-closed time increased (the standard error of these and the subsequent measurements are all less than 0.01; P < 0.0001). Interregional correlations (Pearson's r) were computed separately for in-network and out-of-network recording sites. Within-network correlations increased from 0.39 to 0.52 to 0.54 with increasing eyes-closed time (n=4462, 3376 and 7631, respectively; P<0.0001). Out-of-network correlations increased by a smaller absolute amount but by a similar proportion, from 0.20 to 0.28 to 0.29 (n=22125, 6588 and 27676; P< 0.0001).

With a human subject in a completely dark room who is free to open or close their eyes at will, one might guess that eye closure would be associated with sleepiness. Extrapolating to the monkeys, one might speculate that spontaneous eye closure would be associated with a general cognitive disengagement. Since there is no change in external input when the eyes open or close

in total darkness, we would predict that eye closure (cognitive disengagement) would be associated with a decrease in measures that correlate with neuronal processing, and therefore a decrease in functional connectivity across all networks. This was not seen. Alternatively, if voluntary eye closure reflects relative disengagement with the external world and increased emphasis on internal processing, one might predict that correlates of neuronal activity would decrease in V3 and increase in the default mode network. This pattern was also not seen. Several studies have addressed a similar question in human fMRI (Table S1). McAvoy et al. and Bianciardi et al. report a decrease in the amplitude of low frequency fluctuation in visual cortex when the eyes are open (216, 217). Yang et al. and Yuan et al. show the opposite effect (218, 219). Others report mixed results (220-224). Thus, the published human data fail to show even a trend towards a consistent result.

One possible reason for the heterogeneity across human studies is the lack of control of visual input. Visual input affects the activity in both visual cortex and PCC (203), and therefore differing light levels across studies, or different visual features in the subjects' environments could easily produce differences in BOLD fluctuations or correlation. Additional complications arise if the visual input differs between the eyes open and eyes closed conditions. If opening the eyes changes the visual input, then this may directly drive differences in activity or may drive changes in the internal brain state. In our study, the room was kept completely dark during both eyes-open and eyes-closed conditions, eliminating these confounds. The fact that visual inputs were not eliminated in most human studies may drive many of the differences seen in Table S1. A related possible explanation for heterogeneous results across studies is that "eyes open" and "eyes closed" insufficiently constrain internal brain states. Subjects with their eyes open may, for example, be focusing on visible objects in their external environment, they may be ignoring their

100

surroundings and concentrating on internal thoughts, or they may be completely disengaged, dozing with open eyes. Differences in experimental conditions across studies may differentially bias the internal state. For example, the time of day at which scans are performed or the amount of time spent in the scanner prior to collecting these particular data could affect the likelihood of a subject remaining alert or lightly dozing, especially in the eyes closed sessions. It is also possible that the level of compliance differed across studies due to differences in subject pools, instructions or the type and level of monitoring. Any or all of these factors may contribute to differences across studies. Our strategy of allowing the subject to control when their eyes were open or shut addresses some but not all of these issues. In sum, we suggest that an 'eyes open versus eyes closed' contrast is poorly defined, and care should be taken when using it as an experimental manipulation or interpreting the results.

Oxygen polarography and BOLD fMRI

Oxygen polarography and BOLD fMRI both reflect oxygen level in the brain. The BOLD fMRI signal measures local magnetic field distortions caused by deoxyhemoglobin. The amount of deoxyhemoglobin in a given voxel varies directly with blood volume and inversely with blood oxygen (2). Oxygen polarography measures oxygen availability around the electrode tip, which in our study lies in the gray matter of the brain (225). Blood oxygen and tissue oxygen are generally in equilibrium. Thus, in theory, oxygen polarography and BOLD fMRI should produce similar results (142).

In practice, they do. Visually-evoked polarographic oxygen responses greatly resemble human BOLD responses obtained under similar conditions (Fig 1A, right panel,(149, 226)). Resting state polarographic oxygen signals show long-range correlation, and their correlation

pattern is similar to that reported in resting state fcMRI studies (Fig 1C, (206)). Thus, to a first order, polarography and BOLD fMRI provide comparable results.

Polarographic and BOLD fMRI measurements operate at widely different spatial and temporal scales. Typically, BOLD fMRI samples volumes 2-3 mm on a side at 1-3 s intervals, though spatial resolutions of up to 1 mm on a side and sampling rates of 2.5 Hz or higher are possible (154, 155). In contrast, our oxygen polarography samples spherical volumes 30-100 microns in diameter, which are up to 5 orders of magnitude smaller than BOLD voxels. Temporal frequency is limited by a lowpass filter in our hardware, which is set to 20 Hz in this study.

High frequency functional connectivity

Functional connectivity in BOLD signals is usually analyzed at frequencies below about 0.1 Hz. Typical fcMRI scans have long (2-3 second) repetition times (TR), limiting the upper bound of frequencies that can be examined. However, with the development of methods that allow for faster sampling, several studies have reported that functional connectivity exists in fast BOLD fluctuations above 0.1 Hz (199). Many studies report an upper frequency cut-off between 0.2 and 0.5 Hz, consistent with our polarographic data (227-229). A few studies report significant correlations in the 0.5 - 0.8 or 0.25 to 0.75 Hz bands (230-232).

Almost all studies find that, above 0.1 Hz, functional connectivity drops with frequency (except (232)). Since power also tends to drop with frequency, measurements within a given frequency band are dominated by the lowest frequencies in that band. Thus, functional connectivity within a 0.5 to 0.8 Hz band or a 0.25 to 0.75 Hz band may be driven by effects at 0.5 Hz or 0.25 Hz, respectively. This would not be too dissimilar from the 0.4 Hz high end found

in other studies. Functional connectivity at high frequencies may be the exception rather than the rule; most of the reports showing report data from single seeds in just one or two networks. Another possibility is that discrepancies in high end cut-off frequency could reflect differential sensitivity. For example, the voxels used by Lee *et al.* (4 x 4 x 4 mm) are more than 100,000 larger than the effective polarography voxel, even before spatial smoothing. Thus, correlation that appears to be below the noise level in the polarography data might become reliable when averaged over a much larger volume.

Supplemental Figures

Figure S1
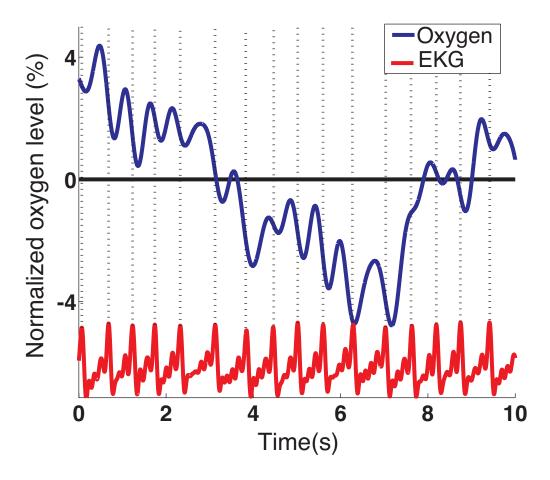
Figure S1, Oxygen and EKG signals, Related to Figure 1 and Figure 2.

The blue trace is an example oxygen signal, red is the simultaneously recorded EKG signal, and the dotted lines mark heart pulsations estimated based on EKG. Near every heart pulsation, there is a signature oxygen change, which reaches a local maximum just before the peak of the EKG and a local minimum just after.

Figure S2
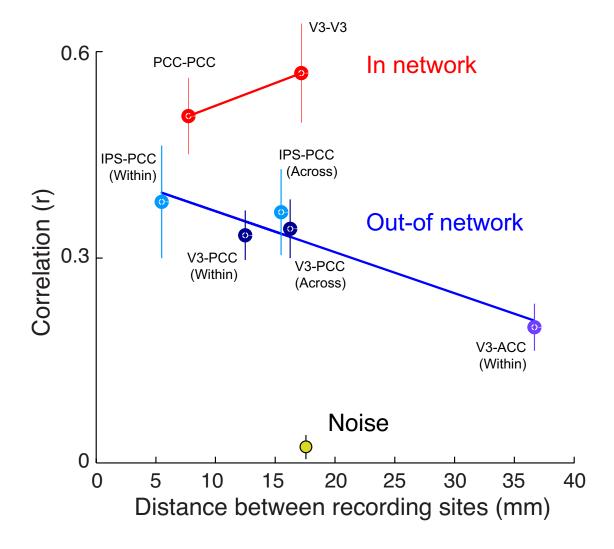
Figure S2, Distance effect on correlation, Related to Figure 2.

Oxygen correlations were computed in a half octave frequency band centered at 0.06 Hz (0.05 - 0.07Hz). In-network correlation is separated into V3-V3 and PCC-PCC correlations. Out-of network correlation is first separated into V3-PCC, IPS-PCC, and V3-ACC correlations (different shades of blue), and it is then further separated into within-hemisphere and across-hemisphere correlations (labeled as 'Within' and 'Across', correspondingly). Out of network correlation appears to have a proximity effect, such that sites that are physically closer to one

another have higher out-of-network correlation. However, this is confounded by network

identity. The farthest distance is for ACC-V3; the intermediate distance is for across-hemisphere

IPS-PCC, and both across- and within-hemisphere V3-PCC; the shortest distance is for within-

hemisphere IPS-PCC. In-network correlation does not have the proximity effect.

Figure S3
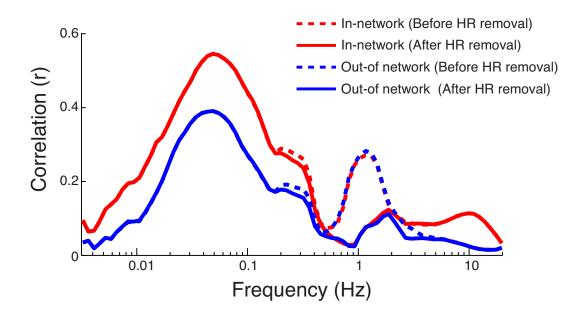
Figure S3. Oxygen correlation before and after heart-rate (HR) removal. Related to Figure 2. The dotted traces are oxygen correlations before HR removal, and the solid traces are oxygen correlations after HR removal. The shoulder at 0.3 Hz and the small peak at 1 Hz are significantly decreased after applying the heart rate removal. 0.3 Hz and 1 Hz corresponds the reported respiratory rate and heart rate in monkeys (208), suggesting that the effect at 0.3 and 1Hz likely reflect residual effects of respiration and heart rate, respectively.

Figure S4

A

B
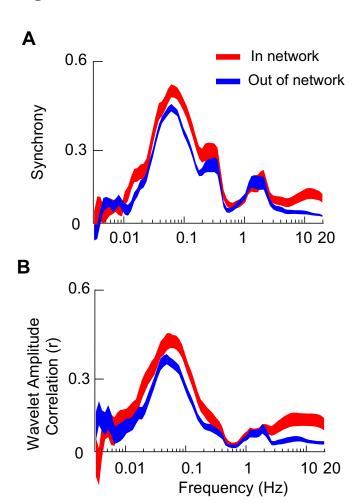
Figure S4, Synchrony and wavelet amplitude correlation (baseline removed), Related to Figure 2.

Similar to coherence in Figure 2B, synchrony and wavelet amplitude correlation are estimated after time-frequency decomposition. Synchrony and wavelet amplitude correlation are defined as follows:

$$Synchrony_{x,y}(f) = \left| \mathbb{E}\{e^{i[\psi_x(t,f) - \psi_y(t,f)]}\} \right|$$

$$Amplitude\ Correlation_{x,y}(f) = \frac{\mathbb{E}\{A_x(t,f)*A_y(t,f)\} - \mathbb{E}\{A_x(t,f)\}*\mathbb{E}\{A_y(t,f)\}}{\sqrt{\mathbb{E}\{A_x(t,f)^2\} - [\mathbb{E}\{A_x(t,f)\}]^2} * \sqrt{\mathbb{E}\{A_y(t,f)^2\} - [\mathbb{E}\{A_y(t,f)\}]^2}}.$$

They measure the strength of phase coupling and amplitude coupling, respectively. Note that the amplitude used in wavelet amplitude correlation is not the oxygen magnitude, but the instantaneous amplitude $A(t,f)$ extracted from the time-frequency decomposition. Similar to coherence and correlation, both synchrony and wavelet amplitude correlation are also band-limited.

Figure S5
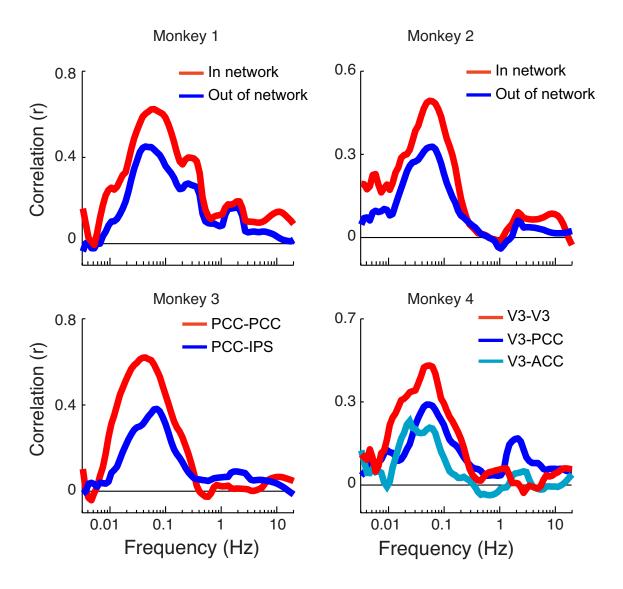
Figure S5, Related to Figure 2 and Discussion.

In all monkeys tested to date, oxygen correlation is band-limited. Red is in-network correlation, and blue is out-of network correlation. Data from Monkey 3 and 4 were collected as part of a different study and are not further described in this paper.

Figure S6
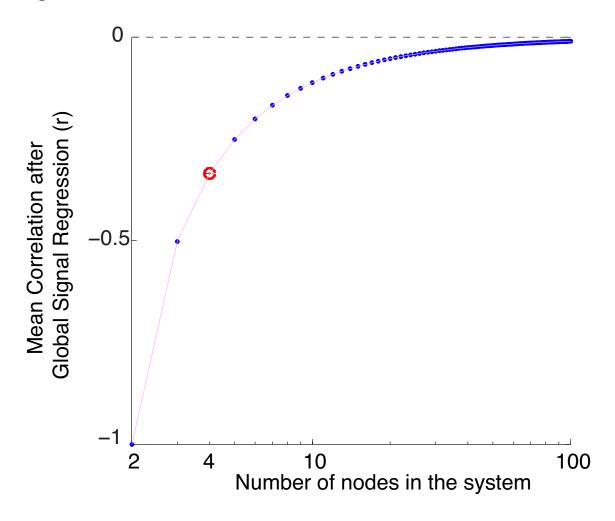
Figure S6, Mean correlation after global signal regression, Related to Discussion.

Independent data streams for systems with different numbers of nodes were synthesized, global

regression was performed (see text), and the resulting internode correlation values were

averaged. Overall, the mean correlation after global regression is driven below zero. The

magnitude of the negative bias introduced by global signal regression is a function of the number

of nodes in the system, and increases as number of nodes decreases. For a 4-node system like

ours, marked with a red dot, mean correlation after regression is -0.34.

Figure S7
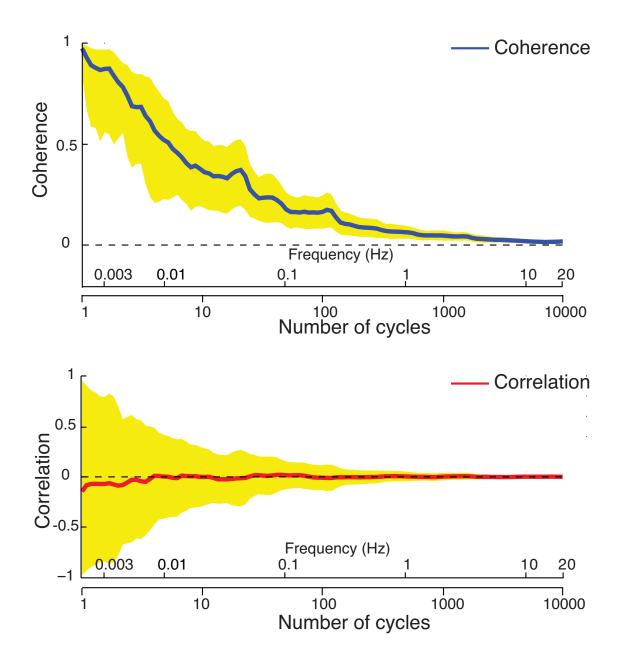
Figure S7, Coherence and correlation between two 8-minute streams of synthetic data, Related to Discussion and Experimental Procedures. Sampling rate and power spectra are matched to the actual polarographic oxygen data, but because each stream was generated independently, the average correlation and coherence should be zero. Mean (lines) and standard

deviation (shading) are shown for 100 repetitions. Coherence (upper panel) is a biased statistic,

increasing as the number of cycles used in the computation decreases. With one cycle of data,

the average coherence is 0.97; with 5 cycles, it is 0.55. Even with 100 cycles of data, coherence

is 0.17. See text for an explanation of this substantial and pervasive bias. Correlation (lower

panel) is unbiased. The estimate approaches zero at all frequencies. However, the large standard

deviation of the estimate renders the statistic nearly meaningless for less than 20 cycles of data

(e.g., SD = 0.29 with 10 cycles of data).

Figure S8
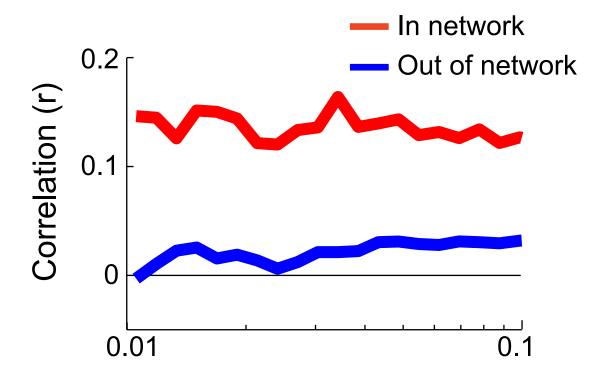
Figure S8, BOLD correlation from the functional connectivity model described by Honey et al., Related to Discussion.

We simulated 20 sessions of 24-minute data using the model described by Honey et al (77). Briefly, the model simulates BOLD correlations as arising from neuronal noise between brain areas that are coupled by anatomical connectivity. From these BOLD correlations, two networks emerge. We computed the frequency profile of the within-network and out-of-network BOLD correlations using the same methods as were used in Fig. 2A of our main text. Unlike the observed polarographic results, the correlations from the model are constant as a function of frequency.

Supplemental Table

Table S1. Eyes closed compared to eyes open

	Amplitude of low frequency BOLD			Functional connectivity		
	Visual network	Default mode network	S1	Visual network	Default mode network	S1
Current study	Greater	Greater		Greater	Greater	
Yang et al. 2007	Less	Equal				
McAvoy et al. 2008	Greater					
Bianciardi et al. 2009	Greater			Greater		
Yan et al. 2009		Less			Less	
Van Dijk et al. 2010				Less	Less	
McAvoy et al. 2012	Greater					
Donahue et al. 2012			Greater			Greater
Patriat et al. 2013				Equal	Equal	
Yuan et al. 2014	Less	Greater				

Chapter 4: Neural basis of functional connectivity MRI

Abstract

Functional connectivity MRI (fcMRI) studies have provided enormous insight into the functional organization of the human brain. fcMRI measures temporal correlations in at-rest blood oxygen level dependent signals (BOLD), which, at best, provide an indirect measure of neural activity. Though much effort has been put towards understanding the relationship between neural activity and BOLD responses evoked during particular tasks, it is unclear whether and how at-rest BOLD correlation is related to neural activity. Here we show that at-rest oxygen correlation reflects correlated spiking activity of neurons. We also show that the causal relationship between spiking and oxygen is mediated by slow LFP. Our results provide conclusive support for the idea that fcMRI reflects patterns of neural activity, present significant challenges to the traditional view of neurohemodynamic coupling, and open up new avenues for exploring the functional significance of fcMRI.

Introduction:

When subjects are at rest, networks of cortical areas distributed across the brain show slow (0.1-0.01 Hz) correlated fluctuations in blood oxygen level dependent signals (BOLD). Analyzing these at-rest BOLD correlations has become the primary approach to study brain functional organization (169). Yet the neural origins of BOLD correlation remain mysterious.

116

We have a rudimentary understanding about the neural activity underlying task-evoked BOLD changes (39), but we do not know whether or to what extent the principles underlying task-evoked BOLD also apply to fcMRI. fcMRI is commonly thought of as reflecting the information transfer across regions (233), yet the details are puzzling. One might expect that information transfer would be maximal during a task and minimal when at rest. Yet fcMRI correlations are prominent in subjects at rest and persist even under anesthesia. Further, fcMRI correlations operate at very slow time scales (10-100 s), which is several orders of magnitude slower than most neural dynamics (but see (71)). This leads us to ask whether BOLD correlation reflects underlying correlated neural signals, or if some other factor is responsible. Potential non-neuronal drivers for slow correlated BOLD include glia or hemodynamic mechanisms (205, 234). Remarkably, there are no reports of long-range correlations in neuronal spiking at the time scale of fcMRI. Several studies report slow correlation in local field potentials (LFP) (191, 235, 236), but LFP signals may themselves arise from non-neuronal origins (237). To address the relationship of fcMRI to neuronal signals, we developed a system to simultaneously record oxygen level and electrophysiology (203). We have previously demonstrated that the system can capture the slow, long-range oxygen correlations that underlie fcMRI (238). We now demonstrate that similar correlations exist in the firing rate of extracellular action potentials (spiking activity), and we present evidence that this activity drives slow changes in the raw local field potential levels that in turn drives long range oxygen correlation (fcMRI).

Results:

We simultaneously recorded from four nodes from two distinct functional networks in awake monkeys resting quietly in the dark. Two of the nodes were in left and right posterior cingulate cortex (PCC), which is part of the default mode network (see Supplementary

Information). The other two nodes were in either left and right V3 or left and right intraparietal

cortex, which are part of the visual attention network. Local field potentials, multi-unit spiking

activity (MUA), single units and oxygen signals were recorded from each node. From LFP, we

extracted both the power of high frequency LFP signals (from delta to gamma), and slow

fluctuations of raw LFP levels (slow LFP, well below 1 Hz). The results were similar across

monkeys and areas, and so were combined.

We asked whether electrophysiological signals, especially single units and MUA, show

long-range, network dependent correlations similar to those found in oxygen. We distinguish two

types of long-range correlations. Within-network correlations occur between signals from the

same network, i.e. between left and right PCC, or between left and right V3. Across-network

correlations occur between signals from different networks, e.g. between left PCC and right V3.

Fig 1 shows long-range correlations in all tested electrophysiological signals, including MUA,

single units, slow LFP, delta power, theta power, alpha power, beta power, and gamma power.

Like oxygen correlations and BOLD correlations prior to global regression, both within- and

across- network electrophysiological correlations are positive (p_{within} <0.05 and p_{across} < 0.05),

and within-network correlation is consistently higher than across-network correlation (p<0.05 for

every comparison) (206, 238). Each electrophysiological correlation shows frequency band-

limiting that grossly matches that of the long-range oxygen correlation (Supplemental Fig. S1).

The match is particular good for the single units. For MUA and single units, the best frequency

for correlation is shifted to a slightly higher frequency (0.03 Hz for MUA, 0.04 Hz for spikes,

0.06 Hz for oxygen), but on the whole there is considerable overlap across the spectra. Thus

interregional oxygen correlations not only reflect interregional LFP power correlation (235); they

also reflect correlated spiking activity.

To address which electrophysiological signal(s) are most tightly coupled to long-range oxygen correlation, we developed a regression-based dependency analysis. It quantifies the extent to which the variance shared between a local electrophysiological signal and the local oxygen signal is the same shared variance that underlies the oxygen correlation (see Fig. 2 and Methods). The analysis reveals that, of all the electrophysiological signals, slow LFP is the most tightly coupled with oxygen correlation. Slow LFP accounts for 72% of the within-network covariance in oxygen and 57% of the across-network covariance in oxygen (Fig. 2). Gamma power and multi-unit activity were the second and third most tightly-coupled signals, respectively, but none accounted for more than 46% of the within-network covariance, or more than 37% of the across-network covariance. Applying a similar analysis to the slow LFP correlation revealed that MUA had the strongest effect, accounting for 51% of both within- and across-network covariance, though LFP power also had a significant effect. Together, these results are consistent with oxygen correlation being driven by slow LFP, and slow LFP being driven primarily by MUA.

To rigorously test for a causal relationship, it would be ideal to extract just the shared (correlated) component, and then using causality analysis (e.g., Granger causality analysis) to determine which, if any, electrophysiological signal appears to drive that correlated component. Methods extracting the correlated component require a large number of correlated signals as input to operate properly. With only four signals, as in our case, the extracted component will necessarily include a substantial amount of non-correlated signal, regardless of the precise method used (see Supplemental Text and Figure S2). Thus, rather than operating on just the correlated component, we instead analyzed causal relationships involving the entire resting-state oxygen signal and electrophysiological signals. To our knowledge this has not been done. In fact,

119

causality analysis has not even been attempted the easier case of relating spikes and LFP to task-evoked oxygen or BOLD, although there have been tests of the necessity of spikes from pyramidal neurons for evoking task-evoked BOLD modulations (e.g., (52, 239)).

For one signal to cause another, it must precede it in time. The closer the linkage, the shorter the time difference. We therefore began our causal analysis by computing lagged cross-correlations and identifying the sign of the time lag that produces the peak correlation. This approach reveals that changes in oxygen lag changes in all tested electrophysiological signals (Fig. 3A). The highest peak, that is, the strongest correlations, are for slow LFP and oxygen and for gamma power and oxygen. The magnitude of the two correlations are almost identical ($p = 0.9$). However, slow LFP leads oxygen by only 0.5 s, while gamma power and MUA lead by ~7 s. The remaining signals (beta, alpha and theta power) lead by 8-11 s and have significantly lower peak correlation values. From this we conclude that slow LFP and gamma power are the best candidates for directly driving oxygen correlation, and slow LFP likely has a closer linkage to oxygen based on its short time lead.

To further investigate the relationships between these signals, we computed spike-triggered averages. We show only oxygen, slow LFP and gamma power, since all LFP power signals yielded results that were similar to gamma power (Fig 3B). All spikes are aligned to the dashed vertical line. The spike-triggered oxygen signal reveals a significant change in oxygen level with a 2 s delay, a peak at 6.1 s, and a slight undershoot at 20 s. The overall time course closely resembles a typical BOLD response to a transient event. This demonstrates, for the first time, a consistent relationship between oxygen and neural activity at the single spike level, and shows that this relationship is present in the resting state. Gamma power, which is often thought of as the best neural correlate of task-evoked BOLD, shows a symmetric elevation that is greatest

120

right at the time of the spike (± 1 s) and reaches baseline at ± 8 s. The time course of gamma power does not at all resemble that of the oxygen response. In contrast, the spike-triggered average of the slow LFP response (the raw potential, not the signal power) has a slow response that is almost identical to the oxygen response, though it leads oxygen by 0.5 s. Both oxygen and slow LFP show a ~8 s progressive drop in signal prior to the spike. Slow LFP but not the oxygen, shows a fast transient drop right at the time of the spike. This downward drop may reflect the tendency of spikes to occur in so-called "up-states", that is, periods in which the intracellular potential is elevated close to threshold and the extracellular potential is depressed. We conclude that slow LFP has a close relationship to oxygen, much closer than that of gamma power. Our results suggest a causal relationship where oxygen is driven by slow LFP, and slow LFP is driven by gamma, other LFP power, and/or spikes (MUA).

As a final step, we computed Granger causality for the local signals (Fig 4A and 4B). Only slow LFP is Granger causal to oxygen. Slow LFP itself is driven mostly by MUA and slightly by gamma power. MUA drives most of the tested signals, including gamma, beta, alpha, and slow LFP, but not oxygen. Finally, both slow LFP and gamma power have a small feedback effect on MUA.

Discussion:

We show that long-range correlation, similar to that seen with oxygen, exists not only in LFP power (delta through gamma bands), but also in slow LFP and, most importantly, in spiking activity. The connection between oxygen correlation and spiking activity provides critical support for the argument that studies of resting state fcMRI illuminate the functional organization of the brain. We also present evidence that resting state oxygen is driven by slow

LFP, and that slow LFP is itself mostly driven by spiking activity and only weakly by gamma power. This is a surprising, since task-evoked BOLD is somewhat better correlated with gamma power than with spikes, and further, spikes are not necessary for BOLD modulation (52, 239). If both sets of findings are correct, then this suggests a fundamental difference in neuro-hemodynamic coupling between resting and task states. At rest, the changes in blood flow that lead to BOLD modulations are driven primarily by spikes and only secondarily by gamma LFP, while during performance of a task, the order is reversed. An alternative possibility is that gamma oscillations are most prominent during task performance (e.g. (39, 240)). At rest they are small and their contribution towards driving blood flow is masked by noise.

It has been speculated that the average level of the extracellular field potential, measured over seconds – the slow cortical potential, which we call the slow LFP – reflects prolonged depolarizations of pyramidal apical dendrites, driven perhaps by widespread non-specific thalamic inputs (28, 44). The hypothesis suggests that slow LFP signals reflect inputs that drive excitability changes, and that these effects are then manifest as changes in spiking activity. However, in the resting state condition, spike-triggered averaging and Granger causality analysis show, respectively, that spiking activity leads and drives the slow LFP; the reverse (slow LFP influencing spike rate) is at best only a weak effect. Our data are consistent with slow LFP reflecting some slow process that is occurs as the result of a spike. One possibility is that slow LFP could arise from a very slow recovery of voltage-gated sodium channels from the inactivation state that follows action potential generation (241-243). Future studies combining intracellular and extracellular recordings with pharmacological approaches that provide manipulations of these channels will help to determine the physiological process underlying LFP and its potential functional role.

Methods:

Animals, and behavior:

Three macaques served as subjects in this study. Animals were cared for and handled in accordance with the Guide for the Care and Use of Laboratory Animals, and all procedures were approved by the Washington University Animal Studies Committee. During recording, macaques were fully hydrated and sat head-fixed in a dark room. Behavior was unconstrained, and the animals had no expectation of a task or reward. Animals naturally relaxed in the setup. Results discussed below are similar for the three monkeys, and thus the data are combined.

Recording:

Pairs of adjacent (0.5 mm apart) microelectrodes were used to simultaneously record oxygen and electrophysiological signals. One pair of electrodes was inserted into each of four brain areas, including two nodes in the default mode network (left and right posterior cingulate cortex, PCC) and two nodes in the visual/attention network (left and right V3 in monkey P and L, and left and right intraparietal sulcus in monkey E). Electrodes were targeted to area of interest using anatomical MRI images and physiology (203). Briefly, each animal's brain was accessed via bilateral 15 mm (internal diameter) chronic custom recording chambers. T1 weighted MRI images (MPRAGE; .5 mm isotropic voxels) were obtained using a custom phantom in the chamber that provides visualization of the chamber and allows for the virtual projection of a chamber-based coordinate system down into the brain. In one monkey, two small manganese injections were placed to confirm alignment. Prior to data collection, boundaries for PCC, V3 and IPS recording regions were defined on the MRI image. The positions of PCC, V3 and IPS were further validated based on their respective oxygen and electrophysiological

responses to visual stimulation, which were recorded immediately before the resting state data (203).

To record oxygen signals, we utilized specialized platinum microelectrodes (FHC Inc. Inventory #: UE(LS3)) as a cathode. An Ag/AgCl reference electrode (Grass Technologies) was placed on the back of the head at a location with minimal underlying musculature and no response to body or limb movements. The skin was lightly abraded to minimize sweat and movement potentials, and a layer of Ten20 EEG paste was applied. The platinum cathode was polarized at -0.8 volts relative to the reference electrode (Unisense PA2000). The current required to maintain the polarization is proportional to oxygen level.

To record electrophysiological signals, we used standard tungsten microelectrodes (Alpha Omega LTD). Unit activity and local field potential (LFP) were extracted from the electrophysiological recording. From the unit activity, offline sorting were performed to extract single unit. Total unit activity (sorted and unsorted units) were referred to as multi-unit activity.

Oxygen and LFP were sampled and stored at 1 kHz, and unit activity was sampled and stored at 40 kHz using the Plexon MAP system (Plexon Inc). Total 54 data sets (19 for monkey P, 16 from monkey E, and 19 from monkey L) with an average length of 50 minutes were recorded.

Analysis:

All analyses were performed with custom software written in Matlab (MathWorks). Oxygen polarographic signals, like BOLD signals, reflect relative rather than absolute oxygen levels. Therefore the polarographic signals, like BOLD data, were expressed as percentage deviation from the mean signal level. LFP data were analyzed into two different ways: the power

of high frequency LFP band (LFP power), and slow fluctuation of raw LFP (slow LFP). LFP signals were first notch filtered at 60 Hz to remove power line noise. To extract LFP power, LFP was filtered into frequency bands, and we applied the Hilbert transform to extract the power. Total five LFP power bands were extracted: Delta (1-4 Hz), Theta (4-8 Hz), Alpha (8-16 Hz), Beta (16-32 Hz), and Gamma (32-128 Hz). Slow LFP was computed by filtering raw LFP below 1 Hz. Unit activity was expressed into instantaneous spiking rate sampled at 1 kHz.

Heart-rate removal. We identified individual heart rate pulsations using a recursive template-matching approach. We started with a 1-second Gaussian-derived generic heart beat template. We identified putative beat times as the moments at which the template had greatest linear correlation with the data using a sliding window approach (1s window with increment of 1ms). We used these times to generate a beat triggered average of the oxygen signal. We then replaced the heart beat template with this beat-triggered average and repeated the analysis. Four iterations were performed in order to refine our estimates of the beat template and the beat times. The estimated heart beat effect was then regressed out of the oxygen signals, taking into account instantaneous heart rate, using the method of Fekete et al. (244).

Correlation and coherence. Correlation was calculated as Pearson's r after filtering signals into 0.01-0.1 Hz, the standard fcMRI frequency range. Lagged correlation was computed as correlation after imposing a lag onto the electrophysiological signals. To calculate coherence, we decomposed each signal into a time-frequency representation. We first filter signals into half octave frequency bands, and extracted the instantaneous amplitude $A(t,f)$ and analytical phase

125

$\psi(t,f)$ as a function of time and frequency by applying the Hilbert transform to each half-octave band. Coherence at the frequency (f) is defined as,

$$Coherence_{x,y}(f) = \left| \frac{\mathbb{E}\{A_x(t,f) * A_y(t,f)e^{i[\psi_x(t,f)-\psi_y(t,f)]}\}}{\sqrt{\mathbb{E}\{A_x(t,f)^2\}} * \sqrt{\mathbb{E}\{A_y(t,f)^2\}}} \right|,$$

where $\mathbb{E}$ is the expectation or mean value across time (t). Coherence measures the degree of consistency of the phase difference $\Phi_{x,y}(t,f) = \psi_x(t,f) - \psi_y(t,f)$ across time. It ranges over the interval 0 to 1. The more consistent the phase difference across time, the higher the coherence value. All statistics on correlation and coherence were done after applying Fisher's Z transform (245)

The bias in coherence was estimated on two independent synthetic signals, each with the same duration and power spectrum as the recorded oxygen signals. This process was repeated 100 times and the resultant values were averaged to compute the mean expected bias. For the result reported in Fig. S1, the mean expected bias was subtracted out so that a value of zero corresponds to the consistency of phase differences that would be obtained by chance were the null hypothesis true (no coherence).

Regression-based dependency analysis. Regression-based dependency analysis estimates the extent to which regressing out a particular electrophysiological signal can diminish interregional oxygen correlation. If regressing out gamma power (or any other electrophysiological signal) from oxygen completely abolishes interregional oxygen correlation, then interregional oxygen correlation completely depends on gamma power, or gamma power accounts for 100% of the interregional oxygen correlation. If there is no effect of the regression, then correlation does not depend at all on gamma power. Intermediate effects indicate partial dependence.

126

Intuitively, regression-based dependency analysis computes the amount of the covariance underlying oxygen correlation that is the same as the covariance between oxygen and electrophysiological signals. We referred to it as the amount of covariance being accounted by electrophysiological signals. The accounted covariance is defined as,

$$Accounted\ covariance\ (\%) =$$

$$\frac{(Covariance_{Before\ regression} - Covariance_{After\ regression})}{Covariance_{Before\ regression}} \times 100\%$$

The regression between electrophysiological and oxygen signals can be performed on the raw signals. However, this is very likely to underestimate the effect, because previous studies have argued that a transfer function needs to be applied before the regression to reflect the neuro-hemodynamic coupling. The transform function was computed using Welch's method with a window size of 5 mins. Electrophysiological signals after convolving with the transfer function were regressed out of the oxygen signal.

We performed the regression-based dependency on both within-network and across-network correlations.

Granger causality. Granger causality was computed to determined the causal relationship among electrophysiological and oxygen signals (246). Briefly, Granger causality determines whether the history of signal A and B together can improve the prediction of the future of B, compared to using the history of B alone. If it does, then A is Granger causal to B. Granger causality is common used to assess causality, but it does not prove causality.

We computed Granger causality using a range of model length (up to 10 s), to account for possible lags in the causal relationship between electrophysiological and oxygen signals. The results were similar, and we presented the result for a model length of 1 s. The magnitude of Granger causality is often thought to lack quantitative meaning beyond its interpretation as an indicator for significance. However, several studies have shown that it can be asymptotically mapped to information-theoretic transfer entropy, though the exact relationship is complex for cases beyond Gaussian distribution (246). Thus, a stronger Granger causality value means a more information passage following the causal link, and it is beyond the scope of current research to determine the exact amount of information corresponding to a particular Granger causality value.

Figures

Figure 1
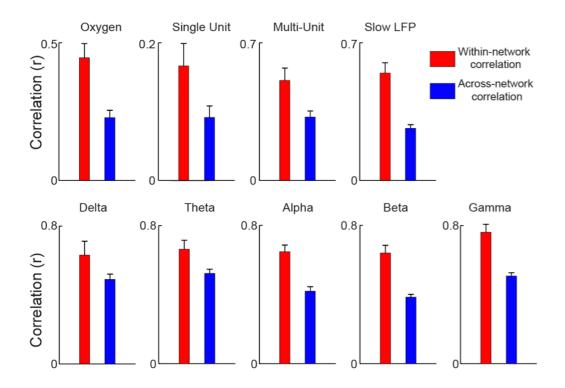
Fig.1. All tested electrophysiological signals, including single units, show long-range, network dependent correlations similar to those shown by oxygen.

Correlations are computed within the standard functional connectivity MRI frequency range of 0.01-0.1 Hz. All tested electrophysiological signals show significantly positive within-network and across-network correlations ($p < 0.001$), and within-network correlation is significantly higher than across-network correlation. Single unit correlations are substantially lower than multi-unit correlations, but this is to be expected, since MUA is less susceptible to the noisiness of spiking by summing over a large local neuron population.

Figure 2
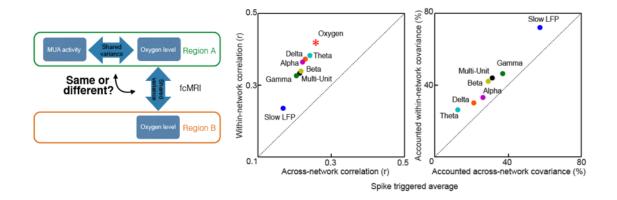
Fig2. Regression-based dependency analysis on oxygen correlation.

Left, dependency analysis determines whether the shared variance between oxygen signals is the same as the shared variance between oxygen and MUA activity (or any other electrophysiological signal). Middle, oxygen correlation before (red asterisk) and after (colored circles) regression. Regressing out slow LFP had the greatest effect on oxygen correlation, substantially reducing both in- and out-of-network correlation. Regressing out other electrophysiological signals produced substantially smaller effects on interregional oxygen correlation. Right, slow LFP accounts for over 70%of the covariance underlying within-network oxygen correlation, and nearly 60% of the covariance underlying across-network correlation. Other electrophysiological signals accounted for only 10-45% of the covariance.

Figure 3
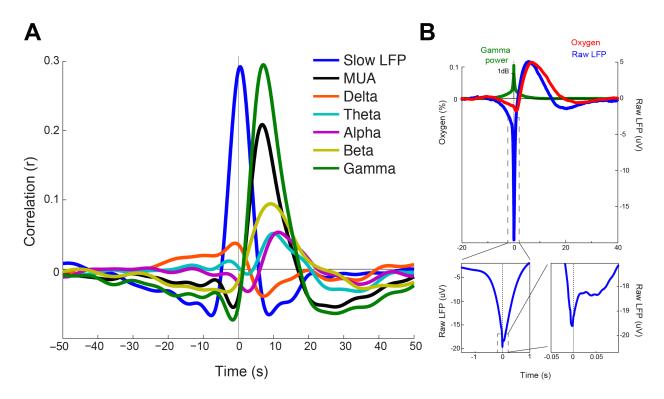
Fig 3. A. Lagged linear correlation between oxygen and electrophysiological signals. Positive lags mean that a delay was imposed on electrophysiological signals before computing the correlation. Positive lags mean that an advance was imposed on electrophysiological signals before computing the correlation. Slow LFP and Gamma power have the strongest correlations with oxygen (p < 0.005). Slow LFP reaches the peak correlation at 0.5 s, which is much shorter than that of gamma power (7.1 s). B. Spike-triggered average of oxygen and electrophysiological signals. Spikes are aligned at time zero. Responses are computed relative to 15 s to 20 s before the spike. Gamma power (green) is elevated at the time of the spike and returns to baseline around ± 8 s. Prior to the spike, both oxygen and raw LFP show a slow. drop. After the spike, both oxygen and raw LFP show a slow delayed increase that peaks around 6 s, slowly falls back toward the baseline, and then overshoots and becomes slightly negative for ~10 s. These slow responses in oxygen and raw LFP closely match with each other, with slow LFP leading by

131

about 0.5 s. In addition, raw LFP has a negative transient response around time zero that lasts

~2 s.   The two insets at the bottom show expansions in time.   The left inset shows that the

duration of the peri-spike negativity is about 1 s. The right inset shows a very brief (< 20 ms)

negativity that is almost exactly coincident with the spike. This could represent contamination of

the LFP (low-passed) signal from the spike itself.

Figure 3
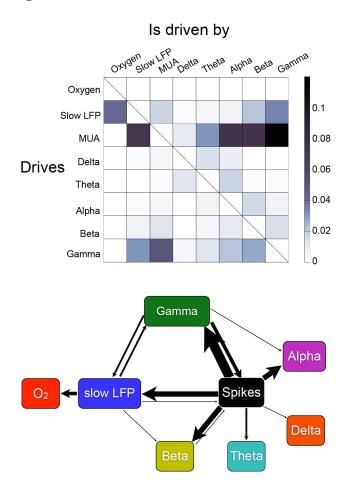
Fig4. Granger causality analysis between oxygen and electrophysiological signals.

Top, each row shows whether a particular signal drives any other signal, and each column shows whether a particular signal is driven by any other signal. Oxygen does not drive any electrophysiological signals (first row), oxygen is only driven by slow LFP (first column), slow LFP is mostly driven by MUA (second column), and MUA drives every other signal except oxygen (third row). Bottom, the graph representation of Granger causality result. The width of the causal links corresponds to the magnitude of the causal relationship, which is quantized into five categories (>0.1, 0.1-0.05, 0.05-0.04, 0.04-0.03, 0.03-0.02). Weak causal relationships (<

0.02) are not shown. Causal links between neighboring LFP bands are due to the fact that

neighboring LFP bands are partial overlapped, and they are generally weak and not shown.

Supplemental Text

The difficulty of extracting the correlated component

There is not a closed form solution to extract the correlated component out of a group of correlated signals. This can be illustrated by considering a simple case: extracting a correlated component out of two correlated signals. When trying to extract the correlated component, the assumption is that an individual signal can be separated into a component that is shared between the two signals, and a component that is not shared (non-correlated component). By the virtue of extracting the correlated component, the two original signals are left with their own non-correlated components. The extraction of the correlated component means to extract three components (one correlated component, and two non-correlated components) out of two sources (the two original signals). There are more extracted components than sources. Thus, a closed form solution does not exist.

Methods exist to extract a component that approximates the correlated component (such as principle component analysis and independent component analysis). The general idea of these methods is to construct a coefficient matrix (247). The matrix is then used to weighted average the original signals to construct the *correlated component. Methods differ on exact criteria that are used to achieve the coefficient matrix. Because the extracted *correlated component is a weighted average of the original signals, the extracted component is inevitably contaminated by the un-correlated components in the original signals. The amount of the contamination is influenced by the magnitude of the correlation, which reflects the ratio between the correlated and non-correlated

135

components in the original signals, and the number of raw signals used to construct the correlated component.

Fig. S2 shows that the amount of contamination deceases as the number of raw signals increases. In the case of our data, we have two sets of two within-network signals (each set corresponds to one of the two functional networks), and four sets of two across-network signals. The extracted *correlated component is heavily contaminated by local un-correlated signals (38.6% for within-network component, and 63.4% for across-network component). To reach a case of the contamination less than 10%, at least 12 within-network signals and 33 across-network signals are needed.
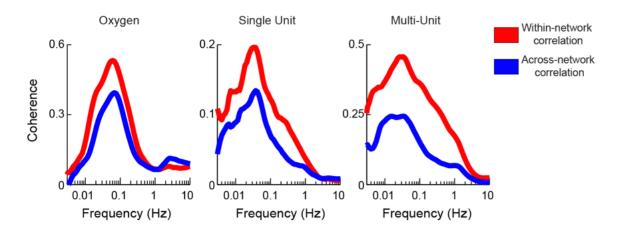
Supplemental Figures

Figure S1

Fig S1. Coherence in oxygen and spiking activity. Oxygen, single unit and multi-unit also show band-limited correlation.

Figure S2
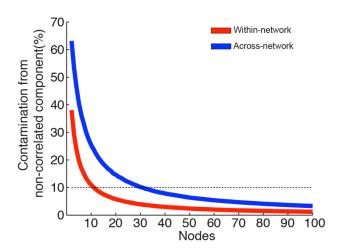
Fig S2. The amount of contaminated from the non-correlated component onto the extracted

*correlated component using principle component analysis.

Chapter 5: Conclusion

Functional connectivity MRI (fcMRI) is widely used to study human brain functional organization in both normal and abnormal subjects. fcMRI examines at-rest correlation in blood oxygen level dependent (BOLD) fluctuations across the brain (1). It reveals that the brain is organized into networks, each network extending across multiple brain areas and subserving particular brain functions. The networks identified by fcMRI are largely stable across subjects, primate species, and levels of consciousness, suggesting that BOLD correlations reflect an evolutionarily conserved, fundamental organization principle of the brain. fcMRI is used to infer the neural basis of the cognitive functions of the brain, such as fluid intelligence and mood. It is also used to assess psychological or neurological diseases, such Alzheimer's disease, depression, and ADHD. It is used to obtain diagnostic and prognostic information, to define disease states, and to determine treatment and treatment effects. Yet, remarkably, it is unclear how fcMRI is related to neural activity.

One puzzling issue is that BOLD correlation measured by fcMRI occurs at rest and persists even under anesthesia. This is odd, because cooperative activity between areas is thought to reflect engagement in a task. At rest, when such engagement is no longer present, the brain should be dominated by uncorrelated activity. Another puzzling aspect of fcMRI is the slow time scale. BOLD correlation operates in the tens of seconds range. This is much slower than most cognitive processes. This leads to questions: does fcMRI reflect neural activity at all? If it does, what role, if any, does it play in cognition?

To address these questions, it would be ideal to record electrophysiology and fcMRI simultaneously. This is possible but extremely challenging, due to the interference between electrophysiology and fcMRI. To circumvent this issue, we adapt oxygen polarography as an alternative measure of BOLD and perform simultaneous oxygen and electrophysiological recording in monkeys.

We first ask whether oxygen polarography captures the same physiological phenomenon as BOLD. We record from posterior cingulate cortex (PCC) and visual areas 3 (V3). BOLD in PCC is suppressed by visual stimuli in humans. Because of this, PCC is termed as a task-negative area. BOLD in V3 is activated by visual stimuli; thus, V3 is termed as a task-positive area. We show that, during a visual stimulus, polarographic oxygen signals are suppressed in PCC and activated in V3 in monkeys. The time course of polarographic oxygen responses closely match that of BOLD responses reported in the literature. These results validate the use of oxygen polarography as a surrogate for BOLD.

We then use oxygen polarography to differentiate between two heuristic models about the origin of BOLD correlation by characterizing the oxygen correlation. As noted before, BOLD correlation is puzzling because of its slow time scale. Two heuristic models have been proposed: criticality and oscillation. The criticality model argues that BOLD correlation emerges as a result of activity propagating in a complex network through a process of self-organization. The slowness of BOLD dynamics is, in this view, part of the 1/f dynamics of criticality. The oscillation model argues that BOLD correlation is driven instead by oscillatory or pseudo-oscillatory mechanisms. We show that the dynamics underlying oxygen correlation is not 1/f, but band-limited. This result shows that functional connectivity is not related to criticality, but instead to specific and potentially localizable oscillatory processes.

Finally, we show that spiking activity shows long-range, slow, and network-dependent correlations, just like oxygen. We demonstrate that spiking activity drives slow LFP, and slow LFP then drives oxygen. These results provide critical support to the notion that oxygen correlation indeed reflects neural activity.

Together, our findings suggest a scenario in which an oscillatory or pseudo-oscillatory process drives slow correlated spiking activity across brain areas. The correlated spike activity then drives correlated hemodynamic responses, which result in turn in long-range oxygen correlation. Looking forward, we are now in a position to investigate the mechanisms driving the oscillation, and the possible roles of the resulting slow long-range correlations in brain function.

Mechanisms driving the oscillation

A simple model of oscillation consists of a delayed negative feedback and a net excitation: the delayed negative feedback drives neurons exiting from a high activity state to a low activity state, the net excitation drives neurons back into the high activity state, and together they generate a slow oscillatory neural activity. We speculate a local origin of such a slow oscillation. We have shown that spikes drive a positive, delayed slow LFP change, with very slow dynamics. We hypothesize that slow LFP is the mirror image of the average membrane potential of local population. If this is the case, slow LFP would reflect the cortical excitability, and a positive LFP change corresponds to membrane hyperpolarization and a decrease in excitability. The positive, delayed LFP change driven by spiking activity is the delayed negative feedback needed for generating a slow oscillation in cortical activity. These oscillations can then be synchronized either by a center oscillation localized in subcortical structures, or via both direct and indirect anatomic connections.

141

We are designing experiments to test this model. First, we want to examine whether slow

LFP changes indeed reflect changes in membrane potential and modulate local excitability.

Intracellular recordings can reveal whether a spike leads to a long-term effect on membrane

potential with a similar time as the spike-triggered extracellular slow LFP. If so, this would

indicate that the extracellular slow LFP may reflect an intracellular change in potential. Second,

we can examine whether the cortical excitability follows the changes in slow LFP. One way to

measure cortical excitability is to determine the amount of current needed to excite local neural

populations. For instance, one could test the excitability of the frontal eye field (FEF) by

determining the threshold of extracellular microstimulation current required to evoke a saccade

from FEF. We predict that during high slow LFP periods, the threshold is higher than that of low

slow periods. If the prediction is correct, this would provide evidence that an increase in slow

LFP leads to a decrease in local excitability. Third, we want to examine the feasibility of

generating slow, long-rang correlation from a local oscillator. Simple oscillator-based models of

functional connectivity exist (e.g.(80)). However, these models focus on oscillators with fast

dynamics, on the order of tens to hundreds of milliseconds. We can examine whether these

models can still be used to predict functional connectivity using oscillators with slow dynamics.

Functional roles of slow correlation

It is puzzling to think about how long-range correlation can play a role in cognition,

because of its slowness. The dominant hypothesis to resolve this issue is "frequency nesting", a

phenomenon in which the phase of low frequency dynamics underlying correlation modulates

the magnitude of some high frequency dynamics. For instance, the magnitude of gamma power

is modulated by the phase of slow oscillation, and gamma power has been implicated to play an

important role in various cognitive processes, such as sensory processing, attention, and working memory. To test this hypothesis, we can examine whether fast dynamics, such as firing rate or gamma power, are indeed nested in the slow dynamics underlying long-range correlation. No study has looked at this issue, because slow dynamics are thought to reflect DC drifts from non-neural sources (such as movement artifact) in recordings. We can also examine whether these slow dynamics can be used to predict variability in task performance, such as the variability in reaction time in an attention task. Finally, we can examine the causal effect in fast dynamics and in task performance after modulating these slow dynamics, using intervention approaches like transcranial direct current stimulation. We predict that the imposed slow oscillatory electrical field can entrain the fast neural dynamics (such as gamma power and spiking activity) to co-fluctuate with the field. We also predict that the task performance (for example, the reaction in a visually guided saccade task) will also co-fluctuate with the imposed field. If these predictions are true, they will support that the slow oscillatory field potential is of functional significance, and slow field potential is likely an unidentified mechanism via which local neural population uses to synchronize with each other. These results are of critical relevance to both basic and clinical neuroscience.

Reference:

1. Raichle ME & Mintun MA (2006) Brain work and brain imaging. *Annual review of neuroscience* 29:449-476.
2. Kim S-G & Bandettini PA (2011) Principles of BOLD Functional MRI. (Springer US, Boston, MA), pp 293-303.
3. Ogawa S, Lee TM, Nayak AS, & Glynn P (1990) Oxygenation-Sensitive Contrast in Magnetic-Resonance Image of Rodent Brain at High Magnetic-Fields. *Magnet Reson Med* 14(1):68-78.
4. Raichle ME & Mintun MA (2006) Brain work and brain imaging. *Annu Rev Neurosci* 29:449-476.
5. Biswal B, Yetkin FZ, Haughton VM, & Hyde JS (1995) Functional Connectivity in the Motor Cortex of Resting Human Brain Using Echo-Planar Mri. *Magnetic Resonance in Medicine* 34(4):537-541.
6. Biswal B, Yetkin FZ, Haughton VM, & Hyde JS (1995) Functional connectivity in the motor cortex of resting human brain using echo-planar MRI. *Magnetic resonance in medicine : official journal of the Society of Magnetic Resonance in Medicine / Society of Magnetic Resonance in Medicine* 34(4):537-541.
7. Hampson M, Peterson BS, Skudlarski P, Gatenby JC, & Gore JC (2002) Detection of functional connectivity using temporal correlations in MR images. *Human brain mapping* 15(4):247-262.
8. Fox MD, Corbetta M, Snyder AZ, Vincent JL, & Raichle ME (2006) Spontaneous neuronal activity distinguishes human dorsal and ventral attention systems. *Proc Natl Acad Sci U S A* 103(26):10046-10051.
9. Seeley WW, *et al.* (2007) Dissociable intrinsic connectivity networks for salience processing and executive control. *The Journal of neuroscience : the official journal of the Society for Neuroscience* 27(9):2349-2356.
10. Greicius MD, Krasnow B, Reiss AL, & Menon V (2003) Functional connectivity in the resting brain: a network analysis of the default mode hypothesis. *Proceedings of the National Academy of Sciences of the United States of America* 100(1):253-258.
11. Friston KJ (2011) Functional and Effective Connectivity: A Review. *Brain connectivity* 1(1):13-36.
12. Vincent JL, *et al.* (2007) Intrinsic functional architecture in the anaesthetized monkey brain. *Nature* 447(7140):83-86.
13. Horovitz SG, *et al.* (2008) Low frequency BOLD fluctuations during resting wakefulness and light sleep: a simultaneous EEG-fMRI study. *Human brain mapping* 29(6):671-682.
14. Fox MD, Snyder AZ, Vincent JL, & Raichle ME (2007) Intrinsic fluctuations within cortical systems account for intertrial variability in human behavior. *Neuron* 56(1):171-184.
15. Hesselmann G, Kell CA, Eger E, & Kleinschmidt A (2008) Spontaneous local variations in ongoing neural activity bias perceptual decisions. *Proceedings of the National Academy of Sciences of the United States of America* 105(31):10984-10989.

16. Hesselmann G, Kell CA, & Kleinschmidt A (2008) Ongoing activity fluctuations in hMT+ bias the perception of coherent visual motion. *The Journal of neuroscience : the official journal of the Society for Neuroscience* 28(53):14481-14485.

17. Dhond RP, Yeh C, Park K, Kettner N, & Napadow V (2008) Acupuncture modulates resting state connectivity in default and sensorimotor brain networks. *Pain* 136(3):407-418.

18. Hampson M, Driesen NR, Skudlarski P, Gore JC, & Constable RT (2006) Brain connectivity related to working memory performance. *J Neurosci* 26(51):13338-13343.

19. Takeuchi H*, et al.* (2012) The association between resting functional connectivity and creativity. *Cereb Cortex* 22(12):2921-2929.

20. Lewis CM, Baldassarre A, Committeri G, Romani GL, & Corbetta M (2009) Learning sculpts the spontaneous activity of the resting human brain. *Proceedings of the National Academy of Sciences of the United States of America* 106(41):17558-17563.

21. Baldassarre A*, et al.* (2012) Individual variability in functional connectivity predicts performance of a perceptual task. *Proceedings of the National Academy of Sciences of the United States of America* 109(9):3516-3521.

22. Cherkassky VL, Kana RK, Keller TA, & Just MA (2006) Functional connectivity in a baseline resting-state network in autism. *Neuroreport* 17(16):1687-1690.

23. Bluhm RL*, et al.* (2007) Spontaneous low-frequency fluctuations in the BOLD signal in schizophrenic patients: anomalies in the default network. *Schizophr Bull* 33(4):1004-1012.

24. DeGutis JM, Bentin S, Robertson LC, & D'Esposito M (2007) Functional plasticity in ventral temporal cortex following cognitive rehabilitation of a congenital prosopagnosic. *J Cogn Neurosci* 19(11):1790-1802.

25. He BJ*, et al.* (2007) Breakdown of functional connectivity in frontoparietal networks underlies behavioral deficits in spatial neglect. *Neuron* 53(6):905-918.

26. Friston K (2002) What Can Neuroimaging Tell Us About Distributed Circuitry? *Annual review of neuroscience* 25(1):221-250.

27. Berens P, Logothetis NK, & Tolias AS (2010) Local field potentials, BOLD and spiking activity: Relationships and physiological mechanisms. *Nature Precedings* 2010:1-27.

28. Mitzdorf U (1985) Current source-density method and application in cat cerebral cortex: investigation of evoked potentials and EEG phenomena. *Physiological reviews* 65(1):37-100.

29. Johnston D, Wu SM-S, & Gray R (1995) *Foundations of cellular neurophysiology* (MIT press Cambridge, MA:).

30. Hasenstaub A*, et al.* (2005) Inhibitory postsynaptic potentials carry synchronized frequency information in active cortical networks. *Neuron* 47(3):423-435.

31. Kamondi A, Acsady L, Wang XJ, & Buzsaki G (1998) Theta oscillations in somata and dendrites of hippocampal pyramidal cells in vivo: activity-dependent phase-precession of action potentials. *Hippocampus* 8(3):244-261.

32. Buzsaki G (2002) Theta oscillations in the hippocampus. *Neuron* 33(3):325-340.

33. David SV, Malaval N, & Shamma SA (2010) Decoupling action potential bias from cortical local field potentials. *Computational intelligence and neuroscience*:393019.

34. Muresan RC, Jurjut OF, Moca VV, Singer W, & Nikolic D (2008) The oscillation score: an efficient method for estimating oscillation strength in neuronal activity. *Journal of neurophysiology* 99(3):1333-1353.

35. Burns SP, Xing D, & Shapley RM (2011) Is gamma-band activity in the local field potential of V1 cortex a "clock" or filtered noise? *The Journal of neuroscience : the official journal of the Society for Neuroscience* 31(26):9658-9664.

36. Ray S & Maunsell JH (2011) Different origins of gamma rhythm and high-gamma activity in macaque visual cortex. *PLoS biology* 9(4):e1000610.

37. Magri C, Schridde U, Murayama Y, Panzeri S, & Logothetis NK (2012) The Amplitude and Timing of the BOLD Signal Reflects the Relationship between Local Field Potential Power at Different Frequencies. *Journal of Neuroscience* 32(4):1395-1407.

38. He BJ (2014) Scale-free brain activity: past, present, and future. *Trends in cognitive sciences* 18(9):480-487.

39. Logothetis NK, Pauls J, Augath M, Trinath T, & Oeltermann A (2001) Neurophysiological investigation of the basis of the fMRI signal. *Nature* 412(6843):150-157.

40. Cardin JA*, et al.* (2009) Driving fast-spiking cells induces gamma rhythm and controls sensory responses. *Nature* 459(7247):663-667.

41. Sohal VS, Zhang F, Yizhar O, & Deisseroth K (2009) Parvalbumin neurons and gamma rhythms enhance cortical circuit performance. *Nature* 459(7247):698-702.

42. Buzsáki G & Wang X-J (2012) Mechanisms of Gamma Oscillations. *Annual review of neuroscience* 35(1):203-225.

43. Timofeev I & Bazhenov M (2005) Mechanisms and biological role of thalamocortical oscillations. *Trends in chronobiology research*:1-47.

44. He BJ & Raichle ME (2009) The fMRI signal, slow cortical potential and consciousness. *Trends in cognitive sciences* 13(7):302-309.

45. Speckmann EJ & Walden J (1991) Mechanisms underlying the generation of cortical field potentials. *Acta oto-laryngologica. Supplementum* 491:17-23; discussion 24.

46. Voipio J, Tallgren P, Heinonen E, Vanhatalo S, & Kaila K (2003) Millivolt-scale DC shifts in the human scalp EEG: evidence for a nonneuronal generator. *Journal of neurophysiology* 89(4):2208-2214.

47. Fatt P & Katz B (1952) Spontaneous subthreshold activity at motor nerve endings. *The Journal of physiology* 117(1):109-128.

48. Sanchez-Vives MV & McCormick DA (2000) Cellular and network mechanisms of rhythmic recurrent activity in neocortex. *Nature neuroscience* 3(10):1027-1034.

49. Kim SG & Ogawa S (2012) Biophysical and physiological origins of blood oxygenation level-dependent fMRI signals. *J Cerebr Blood F Met* 32(7):1188-1206.

50. Heeger DJ & Ress D (2002) What does fMRI tell us about neuronal activity? *Nature Reviews Neuroscience* 3(2):142-151.

51. Viswanathan A & Freeman RD (2007) Neurometabolic coupling in cerebral cortex reflects synaptic more than spiking activity. *Nat Neurosci* 10(10):1308-1312.

52. Rauch A, Rainer G, & Logothetis NK (2008) The effect of a serotonin-induced dissociation between spiking and perisynaptic activity on BOLD functional MRI. *Proceedings of the National Academy of Sciences of the United States of America* 105(18):6759-6764.

53. Thomsen K, Piilgaard H, Gjedde A, Bonvento G, & Lauritzen M (2009) Principal Cell Spiking, Postsynaptic Excitation, and Oxygen Consumption in the Rat Cerebellar Cortex. *Journal of neurophysiology* 102(3):1503-1512.

54.   Berens P, Logothetis NK, & Tolias AS (2010) Local field potentials, BOLD and spiking activity – relationships and physiological mechanisms. *Nature Precedings*

55.   Dale AM & Buckner RL (1997) Selective averaging of rapidly presented individual trials using fMRI. *Human brain mapping* 5(5):329-340.

56.   Heckman GM*, et al.* (2007) Nonlinearities in rapid event-related fMRI explained by stimulus scaling. *NeuroImage* 34(2):651-660.

57.   Greicius MD, Supekar K, Menon V, & Dougherty RF (2009) Resting-state functional connectivity reflects structural connectivity in the default mode network. *Cereb Cortex* 19(1):72-78.

58.   Hagmann P*, et al.* (2008) Mapping the structural core of human cerebral cortex. *PLoS biology* 6(7):e159.

59.   Koch MA, Norris DG, & Hund-Georgiadis M (2002) An investigation of functional and anatomical connectivity using magnetic resonance imaging. *NeuroImage* 16(1):241-250.

60.   van den Heuvel M, Mandl R, Luigjes J, & Hulshoff Pol H (2008) Microstructural organization of the cingulum tract and the level of default mode functional connectivity. *The Journal of neuroscience : the official journal of the Society for Neuroscience* 28(43):10844-10851.

61.   Vincent JL*, et al.* (2007) Intrinsic functional architecture in the anaesthetized monkey brain. *Nature* 447(7140):83-86.

62.   Damoiseaux JS & Greicius MD (2009) Greater than the sum of its parts: a review of studies combining structural connectivity and resting-state functional connectivity. *Brain Structure and Function* 213(6):525-533.

63.   Hlinka J, Alexakis C, Diukova A, Liddle PF, & Auer DP (2010) Slow EEG pattern predicts reduced intrinsic functional connectivity in the default mode network: An inter-subject analysis. *Neuroimage* 53(1):239-246.

64.   Lu H*, et al.* (2007) Synchronized delta oscillations correlate with the resting-state functional MRI signal. *P Natl Acad Sci USA* 104(46):18265-18269.

65.   Chang C, Liu Z, Chen MC, Liu X, & Duyn JH (2013) EEG correlates of time-varying BOLD functional connectivity. *Neuroimage* 72:227-236.

66.   Pan WJ, Thompson GJ, Magnuson ME, Jaeger D, & Keilholz S (2013) Infraslow LFP correlates to resting-state fMRI BOLD signals. *NeuroImage* 74:288-297.

67.   Pan WJ*, et al.* (2011) Broadband local field potentials correlate with spontaneous fluctuations in functional magnetic resonance imaging signals in the rat somatosensory cortex under isoflurane anesthesia. *Brain Connect* 1(2):119-131.

68.   Honey CJ, Kotter R, Breakspear M, & Sporns O (2007) Network structure of cerebral cortex shapes functional connectivity on multiple time scales. *P Natl Acad Sci USA* 104(24):10240-10245.

69.   Nir Y*, et al.* (2008) Interhemispheric correlations of slow spontaneous neuronal fluctuations revealed in human sensory cortex. *Nat Neurosci* 11(9):1100-1108.

70.   He BJ, Snyder AZ, Zempel JM, Smyth MD, & Raichle ME (2008) Electrophysiological correlates of the brain's intrinsic large-scale functional architecture. *Proc Natl Acad Sci U S A* 105(41):16039-16044.

71.   Hughes SW, Lorincz ML, Parri HR, & Crunelli V (2011) Infraslow (<0.1 Hz) oscillations in thalamic relay nuclei basic mechanisms and significance to health and disease states. *Progress in brain research* 193:145-162.

72. Levina A, Herrmann JM, & Geisel T (2007) Dynamical synapses causing self-organized criticality in neural networks. *Nature Physics* 3(12):857-860.
73. Millman D, Mihalas S, Kirkwood A, & Niebur E (2010) Self-organized criticality occurs in non-conservative neuronal networks during/up/'states. *Nature physics* 6(10):801-805.
74. Rubinov M, Sporns O, Thivierge J-P, & Breakspear M (2011) Neurobiologically realistic determinants of self-organized criticality in networks of spiking neurons. *PLoS computational biology* 7(6):e1002038.
75. Poil S-S, Hardstone R, Mansvelder HD, & Linkenkaer-Hansen K (2012) Critical-state dynamics of avalanches and oscillations jointly emerge from balanced excitation/inhibition in neuronal networks. *The Journal of Neuroscience* 32(29):9817-9823.
76. Linkenkaer-Hansen K (2002) *Self-organized criticality and stochastic resonance in the human brain* (Helsinki University of Technology).
77. Honey CJ, Kotter R, Breakspear M, & Sporns O (2007) Network structure of cerebral cortex shapes functional connectivity on multiple time scales. *Proceedings of the National Academy of Sciences of the United States of America* 104(24):10240-10245.
78. van den Heuvel MP, Stam CJ, Boersma M, & Hulshoff Pol HE (2008) Small-world and scale-free organization of voxel-based resting-state functional connectivity in the human brain. *NeuroImage* 43(3):528-539.
79. Bassett DS & Bullmore E (2006) Small-world brain networks. *The Neuroscientist : a review journal bringing neurobiology, neurology and psychiatry* 12(6):512-523.
80. Cabral J, Hugues E, Sporns O, & Deco G (2011) Role of local network oscillations in resting-state functional connectivity. *NeuroImage* 57(1):130-139.
81. Shulman GL*, et al.* (1997) Common blood flow changes across visual tasks: II. Decreases in cerebral cortex. *Journal of Cognitive Neuroscience* 9(5):648-663.
82. Binder JR*, et al.* (1999) Conceptual processing during the conscious resting state. A functional MRI study. *Journal of Cognitive Neuroscience* 11(1):80-95.
83. Mazoyer B*, et al.* (2001) Cortical networks for working memory and executive functions sustain the conscious resting state in man. *Brain research bulletin* 54(3):287-298.
84. Raichle ME*, et al.* (2001) A default mode of brain function. *Proc Natl Acad Sci U S A* 98(2):676-682.
85. Raichle ME*, et al.* (2001) A default mode of brain function. *Proceedings of the National Academy of Sciences of the United States of America* 98(2):676-682.
86. Buckner RL, Andrews-Hanna JR, & Schacter DL (2008) The brain's default network: anatomy, function, and relevance to disease. *Annals of the New York Academy of Sciences* 1124:1-38.
87. Anticevic A*, et al.* (2012) The role of default network deactivation in cognition and disease. *Trends Cogn Sci* 16(12):584-592.
88. Fox MD*, et al.* (2005) The human brain is intrinsically organized into dynamic, anticorrelated functional networks. *Proc Natl Acad Sci U S A* 102(27):9673-9678.
89. Mantini D*, et al.* (2011) Default Mode of Brain Function in Monkeys. *Journal of Neuroscience* 31(36):12954-12962.
90. Kojima T*, et al.* (2009) Default mode of brain activity demonstrated by positron emission tomography imaging in awake monkeys: higher rest-related than working memory-related activity in medial cortical areas. *The Journal of neuroscience : the official journal of the Society for Neuroscience* 29(46):14463-14471.

91. Mantini D*, et al.* (2011) Default mode of brain function in monkeys. *The Journal of neuroscience : the official journal of the Society for Neuroscience* 31(36):12954-12962.

92. Mantini D, Corbetta M, Romani GL, Orban GA, & Vanduffel W (2013) Evolutionarily novel functional networks in the human brain? *The Journal of neuroscience : the official journal of the Society for Neuroscience* 33(8):3259-3275.

93. Ramot M*, et al.* (2012) A widely distributed spectral signature of task-negative electrocorticography responses revealed during a visuomotor task in the human cortex. *The Journal of neuroscience : the official journal of the Society for Neuroscience* 32(31):10458-10469.

94. Thompson JK (2005) Separate Spatial Scales Determine Neural Activity-Dependent Changes in Tissue Oxygen within Central Visual Pathways. *Journal of Neuroscience* 25(39):9046-9058.

95. Shmuel A, Augath M, Oeltermann A, & Logothetis NK (2006) Negative functional MRI response correlates with decreases in neuronal activity in monkey visual area V1. *Nature neuroscience* 9(4):569-577.

96. Devor A*, et al.* (2007) Suppressed neuronal activity and concurrent arteriolar vasoconstriction may explain negative blood oxygenation level-dependent signal. *Journal of Neuroscience* 27(16):4452-4459.

97. Goense JB & Logothetis NK (2008) Neurophysiology of the BOLD fMRI signal in awake monkeys. *Current biology : CB* 18(9):631-640.

98. Maier A*, et al.* (2008) Divergence of fMRI and neural signals in V1 during perceptual suppression in the awake monkey. *Nature neuroscience* 11(10):1193-1200.

99. Ekstrom A, Suthana N, Millett D, Fried I, & Bookheimer S (2009) Correlation between BOLD fMRI and theta-band local field potentials in the human hippocampal area. *J Neurophysiol* 101(5):2668-2678.

100. Foster BL, Dastjerdi M, & Parvizi J (2012) Neural populations in human posteromedial cortex display opposing responses during memory and numerical processing. *Proceedings of the National Academy of Sciences of the United States of America* 109(38):15514-15519.

101. He BYJ, Snyder AZ, Zempel JM, Smyth MD, & Raichle ME (2008) Electrophysiological correlates of the brain's intrinsic large-scale functional architecture. *Proc Natl Acad Sci U S A* 105(41):16039-16044.

102. Lu H*, et al.* (2007) Synchronized delta oscillations correlate with the resting-state functional MRI signal. *Proc Natl Acad Sci U S A* 104(46):18265-18269.

103. Pan W-J, Thompson GJ, Magnuson ME, Jaeger D, & Keilholz S (2013) Infraslow LFP correlates to resting-state fMRI BOLD signals. *NeuroImage* 74:288-297.

104. Singh KD (2012) Which "neural activity" do you mean? fMRI, MEG, oscillations and neurotransmitters. *NeuroImage* 62(2):1121-1130.

105. Kayser C (2004) A Comparison of Hemodynamic and Neural Responses in Cat Visual Cortex Using Complex Stimuli. *Cerebral Cortex* 14(8):881-891.

106. Niessing J (2005) Hemodynamic Signals Correlate Tightly with Synchronized Gamma Oscillations. *Science* 309(5736):948-951.

107. Hayden BY, Smith DV, & Platt ML (2009) Electrophysiological correlates of default-mode processing in macaque posterior cingulate cortex. *Proc Natl Acad Sci U S A* 106(14):5948-5953.

108. Jerbi (2010) Exploring the electrophysiological correlates of the default-mode network with intracerebral EEG. *Frontiers in Systems Neuroscience*.

109. Dastjerdi M*, et al.* (2011) Differential electrophysiological response during rest, self-referential, and non-self-referential tasks in human posteromedial cortex. *Proc Natl Acad Sci U S A* 108(7):3023-3028.

110. Ossandon T*, et al.* (2011) Transient Suppression of Broadband Gamma Power in the Default-Mode Network Is Correlated with Task Complexity and Subject Performance. *Journal of Neuroscience* 31(41):14521-14530.

111. Foster BL & Parvizi J (2012) Resting oscillations and cross-frequency coupling in the human posteromedial cortex. *NeuroImage* 60(1):384-391.

112. Gabbott PL & Rolls ET (2013) Increased neuronal firing in resting and sleep in areas of the macaque medial prefrontal cortex. *The European journal of neuroscience* 37(11):1737-1746.

113. van den Heuvel MP & Sporns O (2013) An anatomical substrate for integration among functional networks in human cortex. *The Journal of neuroscience : the official journal of the Society for Neuroscience* 33(36):14489-14500.

114. Bronk DW, Larrabee MG, & Davies PW (1946) The rate of oxygen consumption in localized regions of the nervous system: in presynaptic endings and in cell bodies. *Fed Proc* 5(1):11.

115. Thompson JK, Peterson MR, & Freeman RD (2004) High-resolution neurometabolic coupling revealed by focal activation of visual neurons. *Nature neuroscience* 7(9):919-920.

116. Masamoto K, Vazquez A, Wang P, & Kim S-G (2008) Trial-by-trial relationship between neural activity, oxygen consumption, and blood flow responses. *NeuroImage* 40(2):442-450.

117. Thomsen K, Piilgaard H, Gjedde A, Bonvento G, & Lauritzen M (2009) Principal Cell Spiking, Postsynaptic Excitation, and Oxygen Consumption in the Rat Cerebellar Cortex. *J Neurophysiol* 102(3):1503-1512.

118. Lowry JP*, et al.* (2010) Real-time electrochemical monitoring of brain tissue oxygen: a surrogate for functional magnetic resonance imaging in rodents. *NeuroImage* 52(2):549-555.

119. Clark LC, Jr., Wolf R, Granger D, & Taylor Z (1953) Continuous recording of blood oxygen tensions by polarography. *J Appl Physiol* 6(3):189-193.

120. Fatt I (1976) Polarographic Oxygen Sensors. *CRC press* Cleveland Ohio.

121. Saleem KS & Logothetis NK (2007) *A combined MRI and histology atlas of the rhesus monkey brain in stereotaxic coordinates* (Elsevier/Academic press, San Diego).

122. Worsley KJ & Friston KJ (1995) Analysis of fMRI time-series revisited--again. *NeuroImage* 2(3):173-181.

123. Rosa MJ, Kilner J, Blankenburg F, Josephs O, & Penny W (2010) Estimating the transfer function from neuronal activity to BOLD using simultaneous EEG-fMRI. *NeuroImage* 49(2):1496-1509.

124. Wu L, Eichele T, & Calhoun VD (2010) Reactivity of hemodynamic responses and functional connectivity to different states of alpha synchrony: A concurrent EEG-fMRI study. *NeuroImage* 52(4):1252-1260.

125. Press WHT, Saul A. Vetterling, William T. and Flannery, Brain P. (2007) Numerical Recipes: The Art of Scientific Computing Third Edition. *Cambridge University Press*.

126. Kwong KK, *et al.* (1992) Dynamic magnetic resonance imaging of human brain activity during primary sensory stimulation. *Proceedings of the National Academy of Sciences of the United States of America* 89(12):5675-5679.

127. Ogawa S, *et al.* (1992) Intrinsic signal changes accompanying sensory stimulation: functional brain mapping with magnetic resonance imaging. *Proceedings of the National Academy of Sciences of the United States of America* 89(13):5951-5955.

128. Lustig C, *et al.* (2003) Functional deactivations: change with age and dementia of the Alzheimer type. *Proc Natl Acad Sci U S A* 100(24):14504-14509.

129. Bartolo MJ, *et al.* (2011) Stimulus-induced dissociation of neuronal firing rates and local field potential gamma power and its relationship to the resonance blood oxygen level-dependent signal in macaque primary visual cortex. *The European journal of neuroscience* 34(11):1857-1870.

130. Mukamel R (2005) Coupling Between Neuronal Firing, Field Potentials, and fMRI in Human Auditory Cortex. *Science* 309(5736):951-954.

131. Murayama Y, *et al.* (2010) Relationship between neural and hemodynamic signals during spontaneous activity studied with temporal kernel CCA. *Magnetic resonance imaging* 28(8):1095-1103.

132. Hermes D, *et al.* (2012) Neurophysiologic correlates of fMRI in human motor cortex. *Human brain mapping* 33(7):1689-1699.

133. Harvey BM, *et al.* (2013) Frequency specific spatial interactions in human electrocorticography: V1 alpha oscillations reflect surround suppression. *NeuroImage* 65:424-432.

134. Scheeringa R, *et al.* (2011) Neuronal dynamics underlying high- and low-frequency EEG oscillations contribute independently to the human BOLD signal. *Neuron* 69(3):572-583.

135. Sloan HL, *et al.* (2010) Regional differences in neurovascular coupling in rat brain as determined by fMRI and electrophysiology. *NeuroImage* 53(2):399-411.

136. Conner CR, Ellmore TM, Pieters TA, DiSano MA, & Tandon N (2011) Variability of the relationship between electrophysiology and BOLD-fMRI across cortical regions in humans. *J Neurosci* 31(36):12855-12865.

137. Boynton GM, Engel SA, Glover GH, & Heeger DJ (1996) Linear systems analysis of functional magnetic resonance imaging in human V1. *J Neurosci* 16(13):4207-4221.

138. Ogawa S, Lee TM, Kay aR, & Tank DW (1990) Brain magnetic resonance imaging with contrast dependent on blood oxygenation. *Proc Natl Acad Sci U S A* 87(24):9868-9872.

139. Ogawa S, Lee TM, Nayak AS, & Glynn P (1990) Oxygenation-sensitive contrast in magnetic resonance image of rodent brain at high magnetic fields. *Magn Reson Med* 14(1):68-78.

140. Menon RS, *et al.* (1992) Functional brain mapping using magnetic resonance imaging. Signal changes accompanying visual stimulation. *Invest Radiol* 27 Suppl 2:S47-53.

141. Davies PW & Brink F (1942) Microelectrodes for measuring local oxygen tension in animal tissues. *Review of Scientific Instruments* 13(12):524-533.

142. Mintun MA, *et al.* (2001) Blood flow and oxygen delivery to human brain during functional activity: theoretical modeling and experimental data. *Proceedings of the National Academy of Sciences* 98(12):6859-6864.

143. Boynton GM, Engel SA, Glover GH, & Heeger DJ (1996) Linear systems analysis of functional magnetic resonance imaging in human V1. *The Journal of neuroscience : the official journal of the Society for Neuroscience* 16(13):4207-4221.

144. Volkow ND, Rosen B, & Farde L (1997) Imaging the living human brain: magnetic resonance imaging and positron emission tomography. in *Proceedings of the National Academy of Sciences of the United States of America*, pp 2787-2788.

145. Haynes J-D, Lotto RB, & Rees G (2004) Responses of human visual cortex to uniform surfaces. *Proceedings of the National Academy of Sciences* 101(12):4286-4291.

146. Fox MD, Snyder AZ, Barch DM, Gusnard DA, & Raichle ME (2005) Transient BOLD responses at block transitions. *NeuroImage* 28(4):956-966.

147. Horiguchi H, Nakadomari S, Misaki M, & Wandell BA (2009) Two temporal channels in human V1 identified using fMRI. *NeuroImage* 47(1):273-280.

148. Mayhew SD, Macintosh BJ, Dirckx SG, Iannetti GD, & Wise RG (2010) Coupling of simultaneously acquired electrophysiological and haemodynamic responses during visual stimulation. *Magnetic resonance imaging* 28(8):1066-1077.

149. Uludağ K (2008) Transient and sustained BOLD responses to sustained visual stimulation. *Magnetic resonance imaging* 26(7):863-869.

150. Logothetis NK, Guggenberger H, Peled S, & Pauls J (1999) Functional imaging of the monkey brain. *Nature neuroscience* 2(6):555-562.

151. Vanduffel W, *et al.* (2001) Visual motion processing investigated using contrast agent-enhanced fMRI in awake behaving monkeys. *Neuron* 32(4):565-577.

152. Konishi S, Donaldson DI, & Buckner RL (2001) Transient Activation during Block Transition. *NeuroImage* 13(2):364-374.

153. Shulman GL, *et al.* (1997) Common blood flow changes across visual tasks: I. Increases in subcortical structures and cerebellum but not in nonvisual cortex. *Journal of Cognitive Neuroscience* 9(5):624-647.

154. De Martino F, *et al.* (2013) Cortical depth dependent functional responses in humans at 7T: improved specificity with 3D GRASE. *PloS one* 8(3):e60514.

155. Xu J, *et al.* (2013) Evaluation of slice accelerations using multiband echo planar imaging at 3 T. *NeuroImage* 83:991-1001.

156. Birn RM (2012) The role of physiological noise in resting-state functional connectivity. *NeuroImage* 62(2):864-870.

157. Griffanti L, *et al.* (2014) ICA-based artefact removal and accelerated fMRI acquisition for improved resting state network imaging. *NeuroImage* 95C:232-247.

158. Kim SG & Ogawa S (2012) Biophysical and physiological origins of blood oxygenation level-dependent fMRI signals. *J Cereb Blood Flow Metab* 32(7):1188-1206.

159. Lauritzen M, Mathiesen C, Schaefer K, & Thomsen KJ (2012) Neuronal inhibition and excitation, and the dichotomic control of brain hemodynamic and oxygen responses. *Neuroimage* 62(2):1040-1050.

160. Kim R, Hyder F, & Blumenfeld H (2014) Physiological Basis of BOLD fMRI Decreases. *Neurovascular Coupling Methods,* Neuromethods, eds Zhao M, Ma H, & Schwartz TH (Springer, New York), pp 221-236.

161. Dosenbach NUF, *et al.* (2006) A Core System for the Implementation of Task Sets. *Neuron* 50(5):799-812.

162. Yarkoni T, Speer NK, & Zacks JM (2008) Neural substrates of narrative comprehension and memory. *NeuroImage* 41(4):1408-1425.

163. Sambataro F, *et al.* (2010) Age-related alterations in default mode network: Impact on working memory performance. *Neurobiology of Aging* 31(5):839-852.

164. Malonek D & Grinvald A (1996) Interactions between electrical activity and cortical microcirculation revealed by imaging spectroscopy: Implications for functional brain mapping. *Science* 272(5261):551-554.

165. Kim DS, Duong TQ, & Kim SG (2000) High-resolution mapping of iso-orientation columns by fMRI. *Nature neuroscience* 3(2):164-169.

166. Thompson JK, Peterson MR, & Freeman RD (2003) Single-neuron activity and tissue oxygenation in the cerebral cortex. *Science* 299(5609):1070-1072.

167. Friston KJ, Josephs O, Rees G, & Turner R (1998) Nonlinear event-related responses in fMRI. *Magnetic resonance in medicine : official journal of the Society of Magnetic Resonance in Medicine / Society of Magnetic Resonance in Medicine* 39(1):41-52.

168. Siero JC*, et al.* (2013) BOLD consistently matches electrophysiology in human sensorimotor cortex at increasing movement rates: a combined 7T fMRI and ECoG study on neurovascular coupling. *J Cereb Blood Flow Metab* 33(9):1448-1456.

169. Buckner RL, Krienen FM, & Yeo BT (2013) Opportunities and limitations of intrinsic functional connectivity MRI. *Nature neuroscience* 16(7):832-837.

170. Power JD, Fair DA, Schlaggar BL, & Petersen SE (2010) The development of human functional brain networks. *Neuron* 67(5):735-748.

171. Harmelech T, Preminger S, Wertman E, & Malach R (2013) The day-after effect: long term, Hebbian-like restructuring of resting-state fMRI patterns induced by a single epoch of cortical activation. *The Journal of neuroscience : the official journal of the Society for Neuroscience* 33(22):9488-9497.

172. Qin S*, et al.* (2014) Hippocampal-neocortical functional reorganization underlies children's cognitive development. *Nature neuroscience* 17(9):1263-1269.

173. Kerestes R, Davey CG, Stephanou K, Whittle S, & Harrison BJ (2014) Functional brain imaging studies of youth depression: A systematic review. *NeuroImage. Clinical* 4:209-231.

174. Menon V (2013) Developmental pathways to functional brain networks: emerging principles. *Trends in cognitive sciences* 17(12):627-640.

175. Meijer FJ & Goraj B (2014) Brain MRI in Parkinson's disease. *Frontiers in bioscience* 6:360-369.

176. Dennis EL & Thompson PM (2013) Typical and atypical brain development: a review of neuroimaging studies. *Dialogues Clin Neurosci* 15(3):359-384.

177. He BJ, Snyder AZ, Zempel JM, Smyth MD, & Raichle ME (2008) Electrophysiological correlates of the brain's intrinsic large-scale functional architecture. *Proceedings of the National Academy of Sciences of the United States of America* 105(41):16039-16044.

178. Hughes SW*, et al.* (2004) Synchronized oscillations at alpha and theta frequencies in the lateral geniculate nucleus. *Neuron* 42(2):253-268.

179. Hughes SW & Crunelli V (2005) Thalamic mechanisms of EEG alpha rhythms and their pathological implications. *The Neuroscientist : a review journal bringing neurobiology, neurology and psychiatry* 11(4):357-372.

180. Lorincz ML, Crunelli V, & Hughes SW (2008) Cellular dynamics of cholinergically induced alpha (8-13 Hz) rhythms in sensory thalamic nuclei in vitro. *The Journal of neuroscience : the official journal of the Society for Neuroscience* 28(3):660-671.

181. Cabral J*, et al.* (2014) Exploring mechanisms of spontaneous functional connectivity in MEG: how delayed network interactions lead to structured amplitude envelopes of band-pass filtered oscillations. *NeuroImage* 90:423-435.

182. Cabral J, Kringelbach ML, & Deco G (2014) Exploring the network dynamics underlying brain activity during rest. *Progress in neurobiology* 114:102-131.

183. Deco G*, et al.* (2013) Resting-state functional connectivity emerges from structurally and dynamically shaped slow linear fluctuations. *The Journal of neuroscience : the official journal of the Society for Neuroscience* 33(27):11239-11252.

184. He BJ, Zempel JM, Snyder AZ, & Raichle ME (2010) The temporal structures and functional significance of scale-free brain activity. *Neuron* 66(3):353-369.

185. Bak P (1997) *How nature works* (Oxford university press Oxford).

186. Bak P, Tang C, & Wiesenfeld K (1987) Self-organized criticality: An explanation of the 1/f noise. *Physical review letters* 59(4):381-384.

187. Jensen HJ (1998) *Self-organized criticality: emergent complex behavior in physical and biological systems* (Cambridge university press).

188. Mitzenmacher M (2004) A brief history of generative models for power law and lognormal distributions. *Internet mathematics* 1(2):226-251.

189. He BJ (2011) Scale-free properties of the functional magnetic resonance imaging signal during rest and task. *The Journal of neuroscience : the official journal of the Society for Neuroscience* 31(39):13786-13795.

190. Bullmore E*, et al.* (2001) Colored noise and computational inference in neurophysiological (fMRI) time series analysis: resampling methods in time and wavelet domains. *Human brain mapping* 12(2):61-78.

191. Ko AL, Darvas F, Poliakov A, Ojemann J, & Sorensen LB (2011) Quasi-periodic fluctuations in default mode network electrophysiology. *The Journal of neuroscience : the official journal of the Society for Neuroscience* 31(32):11728-11732.

192. Ciuciu P, Abry P, & He BJ (2014) Interplay between functional connectivity and scale-free dynamics in intrinsic fMRI networks. *NeuroImage* 95:248-263.

193. Salvador R*, et al.* (2008) A simple view of the brain through a frequency-specific functional connectivity measure. *NeuroImage* 39(1):279-289.

194. Salvador R, Suckling J, Schwarzbauer C, & Bullmore E (2005) Undirected graphs of frequency-dependent functional connectivity in whole brain networks. *Philosophical transactions of the Royal Society of London. Series B, Biological sciences* 360(1457):937-946.

195. Sasai S, Homae F, Watanabe H, & Taga G (2011) Frequency-specific functional connectivity in the brain during resting state revealed by NIRS. *NeuroImage* 56(1):252-257.

196. Achard S, Salvador R, Whitcher B, Suckling J, & Bullmore E (2006) A resilient, low-frequency, small-world human brain functional network with highly connected association cortical hubs. *The Journal of neuroscience : the official journal of the Society for Neuroscience* 26(1):63-72.

197. Cordes D*, et al.* (2000) Mapping functionally related regions of brain with functional connectivity MR imaging. *AJNR. American journal of neuroradiology* 21(9):1636-1644.

198. Kiviniemi V, Kantola JH, Jauhiainen J, Hyvarinen A, & Tervonen O (2003) Independent component analysis of nondeterministic fMRI signal sources. *NeuroImage* 19(2 Pt 1):253-260.

199. Niazy RK, Xie J, Miller K, Beckmann CF, & Smith SM (2011) Spectral characteristics of resting state networks. *Progress in brain research* 193:259-276.

200. Zhang YJ*, et al.* (2012) Determination of dominant frequency of resting-state brain interaction within one functional system. *PloS one* 7(12):e51584.
201. Wu CW*, et al.* (2008) Frequency specificity of functional connectivity in brain networks. *NeuroImage* 42(3):1047-1055.
202. Cordes D*, et al.* (2001) Frequencies contributing to functional connectivity in the cerebral cortex in "resting-state" data. *AJNR. American journal of neuroradiology* 22(7):1326-1333.
203. Bentley WJ, Li JM, Snyder AZ, Raichle M, & Snyder LH (2014) Oxygen level and LFP in task positive and task negative areas: Bridging BOLD fMRI and electrophysiology *Cerebral Cortex*:In press.
204. Fox MD*, et al.* (2005) The human brain is intrinsically organized into dynamic, anticorrelated functional networks. *Proceedings of the National Academy of Sciences of the United States of America* 102(27):9673-9678.
205. Birn RM (2012) The role of physiological noise in resting-state functional connectivity. *NeuroImage* 62(2):864-870.
206. Murphy K, Birn RM, Handwerker DA, Jones TB, & Bandettini PA (2009) The impact of global signal regression on resting state correlations: are anti-correlated networks introduced? *NeuroImage* 44(3):893-905.
207. Fox MD, Zhang D, Snyder AZ, & Raichle ME (2009) The global signal and observed anticorrelated resting state brain networks. *Journal of neurophysiology* 101(6):3270-3283.
208. Teichert T, Grinband J, Hirsch J, & Ferrera VP (2010) Effects of heartbeat and respiration on macaque fMRI: implications for functional connectivity. *Neuropsychologia* 48(7):1886-1894.
209. Masamoto K, Vazquez A, Wang P, & Kim SG (2008) Trial-by-trial relationship between neural activity, oxygen consumption, and blood flow responses. *NeuroImage* 40(2):442-450.
210. Mathiesen C*, et al.* (2011) Activity-dependent increases in local oxygen consumption correlate with postsynaptic currents in the mouse cerebellum in vivo. *The Journal of neuroscience : the official journal of the Society for Neuroscience* 31(50):18327-18337.
211. Cooper R, Crow HJ, Walter WG, & Winter AL (1966) Regional control of cerebral vascular reactivity and oxygen supply in man. *Brain research* 3(2):174-191.
212. Clark LC, Misrahy G, & Fox RP (1958) Chronically implanted polarographic electrodes. *Journal of applied physiology* 13(1):85-91.
213. Scholvinck ML, Maier A, Ye FQ, Duyn JH, & Leopold DA (2010) Neural basis of global resting-state fMRI activity. *Proceedings of the National Academy of Sciences of the United States of America* 107(22):10238-10243.
214. Saad ZS*, et al.* (2012) Trouble at rest: how correlation patterns and group differences become distorted after global signal regression. *Brain connectivity* 2(1):25-32.
215. Power JD*, et al.* (2014) Methods to detect, characterize, and remove motion artifact in resting state fMRI. *NeuroImage* 84:320-341.
216. Bianciardi M*, et al.* (2009) Modulation of spontaneous fMRI activity in human visual cortex by behavioral state. *NeuroImage* 45(1):160-168.
217. McAvoy M*, et al.* (2008) Resting states affect spontaneous BOLD oscillations in sensory and paralimbic cortex. *Journal of neurophysiology* 100(2):922-931.

218. Yang H, *et al.* (2007) Amplitude of low frequency fluctuation within visual areas revealed by resting-state functional MRI. *NeuroImage* 36(1):144-152.

219. Yuan BK, Wang J, Zang YF, & Liu DQ (2014) Amplitude differences in high-frequency fMRI signals between eyes open and eyes closed resting states. *Frontiers in human neuroscience* 8:503.

220. Van Dijk KR, *et al.* (2010) Intrinsic functional connectivity as a tool for human connectomics: theory, properties, and optimization. *Journal of neurophysiology* 103(1):297-321.

221. Donahue MJ, *et al.* (2012) Spontaneous blood oxygenation level-dependent fMRI signal is modulated by behavioral state and correlates with evoked response in sensorimotor cortex: a 7.0-T fMRI study. *Human brain mapping* 33(3):511-522.

222. McAvoy M, *et al.* (2012) Dissociated mean and functional connectivity BOLD signals in visual cortex during eyes closed and fixation. *Journal of neurophysiology* 108(9):2363-2372.

223. Patriat R, *et al.* (2013) The effect of resting condition on resting-state fMRI reliability and consistency: a comparison between resting with eyes open, closed, and fixated. *NeuroImage* 78:463-473.

224. Yan C, *et al.* (2009) Spontaneous brain activity in the default mode network is sensitive to different resting-state conditions with limited cognitive load. *PloS one* 4(5):e5743.

225. Davies PW & Brink F (1942) Direct Measurement of the Brain Oxygen Concentration with a Platinum Electrode. *Fed Proc* 1:19.

226. Lustig C, *et al.* (2003) Functional deactivations: change with age and dementia of the Alzheimer type. *Proceedings of the National Academy of Sciences of the United States of America* 100(24):14504-14509.

227. Boubela RN, *et al.* (2013) Beyond Noise: Using Temporal ICA to Extract Meaningful Information from High-Frequency fMRI Signal Fluctuations during Rest. *Frontiers in human neuroscience* 7:168.

228. Posse S, *et al.* (2013) High-speed real-time resting-state FMRI using multi-slab echo-volumar imaging. *Frontiers in human neuroscience* 7:479.

229. Boyacioglu R, Beckmann CF, & Barth M (2013) An Investigation of RSN Frequency Spectra Using Ultra-Fast Generalized Inverse Imaging. *Frontiers in human neuroscience* 7:156.

230. Gohel SR & Biswal BB (2015) Functional integration between brain regions at rest occurs in multiple-frequency bands. *Brain connectivity* 5(1):23-34.

231. Kalcher K, *et al.* (2014) The spectral diversity of resting-state fluctuations in the human brain. *PloS one* 9(4):e93375.

232. Lee HL, Zahneisen B, Hugger T, LeVan P, & Hennig J (2013) Tracking dynamic resting-state networks at higher frequencies using MR-encephalography. *NeuroImage* 65:216-222.

233. Deco G, Jirsa VK, & McIntosh AR (2011) Emerging concepts for the dynamical organization of resting-state activity in the brain. *Nature Reviews Neuroscience* 12(1):43-56.

234. Fields RD, Woo DH, & Basser PJ (2015) Glial Regulation of the Neuronal Connectome through Local and Long-Distant Communication. *Neuron* 86(2):374-386.

235. Thompson GJ, *et al.* (2013) Neural correlates of time-varying functional connectivity in the rat. *NeuroImage* 83:826-836.

236.   He BYJ, Snyder AZ, Zempel JM, Smyth MD, & Raichle ME (2008) Electrophysiological correlates of the brain's intrinsic large-scale functional architecture. *Proceedings of the National Academy of Sciences of the United States of America* 105(41):16039-16044.

237.   Buzsaki G, Anastassiou CA, & Koch C (2012) The origin of extracellular fields and currents--EEG, ECoG, LFP and spikes. *Nature reviews. Neuroscience* 13(6):407-420.

238.   Li JM, Bentley WJ, Snyder AZ, Raichle ME, & Snyder LH (2015) Functional connectivity arises from a slow rhythmic mechanism. *Proceedings of the National Academy of Sciences of the United States of America*.

239.   Viswanathan A & Freeman RD (2007) Neurometabolic coupling in cerebral cortex reflects synaptic more than spiking activity. *Nature neuroscience* 10(10):1308-1312.

240.   Berens P, Keliris GA, Ecker AS, Logothetis NK, & Tolias AS (2008) Comparing the feature selectivity of the gamma-band of the local field potential and the underlying spiking activity in primate visual cortex. *Frontiers in systems neuroscience* 2:2.

241.   Toib A, Lyakhov V, & Marom S (1998) Interaction between duration of activity and time course of recovery from slow inactivation in mammalian brain Na+ channels. *The Journal of neuroscience : the official journal of the Society for Neuroscience* 18(5):1893-1903.

242.   Ogata N & Tatebayashi H (1992) Slow inactivation of tetrodotoxin-insensitive Na+ channels in neurons of rat dorsal root ganglia. *The Journal of membrane biology* 129(1):71-80.

243.   Mickus T, Jung H, & Spruston N (1999) Properties of slow, cumulative sodium channel inactivation in rat hippocampal CA1 pyramidal neurons. *Biophysical journal* 76(2):846-860.

244.   Fekete T, Rubin D, Carlson JM, & Mujica-Parodi LR (2011) The NIRS Analysis Package: noise reduction and statistical inference. *PloS one* 6(9):e24322.

245.   Rosenberg JR, Amjad AM, Breeze P, Brillinger DR, & Halliday DM (1989) The Fourier approach to the identification of functional coupling between neuronal spike trains. *Progress in biophysics and molecular biology* 53(1):1-31.

246.   Barnett L & Seth AK (2014) The MVGC multivariate Granger causality toolbox: a new approach to Granger-causal inference. *Journal of neuroscience methods* 223:50-68.

247.   Li K, Guo L, Nie J, Li G, & Liu T (2009) Review of methods for functional brain connectivity detection using fMRI. *Computerized medical imaging and graphics : the official journal of the Computerized Medical Imaging Society* 33(2):131-139.